

Study of pulse shape discrimination and low
background techniques for liquid xenon dark
matter detectors.

Kota Ueshima
Department of Physics, School of Science,
University of Tokyo

November 24, 2010

Abstract

The results of various astronomical observations show strong evidence for a large amount of dark matter in the universe. Weakly Interactive Massive Particles (WIMPs) are one of the well motivated dark matter candidates. WIMPs are predicted by Supersymmetry (SUSY), which is an extended theory beyond the Standard Model of the particle physics. Various dedicated dark matter search experiments are underway around the world.

As the first phase of the XMASS experiment, a 1 ton liquid xenon detector was developed to search for dark matter. The energy deposition by dark matter interactions in xenon is expected to be in the few keV to tens of keV range. The key idea behind the XMASS experiment is background (BG) reduction using the self-shielding of liquid xenon. The fiducial volume used to search for dark matter is within the center of the detector.

Radioactive impurities in PMT are the main BG source in the XMASS experiment. So we have developed a special low BG PMT. The radioactive impurities of all materials used in these PMTs were measured using a Germanium detector and those with the lowest radioactive contamination were selected. Details of these developments for low background techniques are described in this thesis. The PMTs developed for XMASS have the lowest radioactivity among all other PMTs.

Typically xenon gas contains 0.1~3 ppm krypton. Krypton has a long-lived radioactive isotope ^{85}Kr . To reach BG level of 10^{-4} counts/day/kg/keV, the goal of the XMASS experiment, krypton contamination in xenon has to be reduced by more than 5 orders of magnitude. The distillation system has been developed to remove krypton from xenon gas. This distillation system has achieved the lowest levels of krypton contamination ever. The design principle and the performance test of the distillation system are described in this thesis.

In order to further improve the sensitivity of XMASS, pulse shape discrimination (PSD) of liquid xenon was also studied in this thesis. A dedicated detector setup was constructed which has a high efficiency of collecting scintillation photons. In the first step of the PSD study, pulse shapes are measured with high light yield in order to evaluate the fundamental difference between nuclear recoils and electron recoils. From this study, a difference in the pulse shapes of nuclear and electron recoils is found even at the low energies relevant for dark matter detection. In the second step, the PSD performance was studied at the expected light yield for the XMASS detector (4.6 p.e./keV). Using a mask made from copper, the light yield was tuned to this value. The rejection power was $2.4 \pm 0.2(\text{stat}) \pm 0.3(\text{sys}) \times 10^{-1}$ for 4.8 ~ 7.2 keV_{ee} events.

Using the PSD technique developed in this thesis, improvement of the sensitivity of XMASS was estimated. The remaining BG caused by the radioactive impurities in the PMTs can be reduced more than one order of magnitude while keeping the detection efficiency of dark matter at 50%. The sensitivity at 90% C.L. is greatly improved to 5.6×10^{-45} cm² from 2.9×10^{-44} cm² using PSD at $M_\chi = 100$ GeV.

Acknowledgments

I would like to express my great appreciation to my adviser, Professor Masayuki Nakahata for introducing me to XMASS experiment. I would also thank him for guiding and encouraging me throughout my graduate course.

I would like to express my gratitude to Prof. Y. Suzuki, the spokesperson of the XMASS experiment. He gave me useful advise related to the experiment and the analysis.

I would like to express my gratitude to Prof. S.Moriyama. He has guided me in many occasions. I learned many things related to physics and experiments from him.

I would like to thank to XMASS collaboration who worked with me, Prof. M.Yamashita who is expert of liquid xenon, Y.Koshio, A.Takeda, K.Abe, H.Sekiya, H.Ogawa, K.Kobayashi, K.Hiraide, A.Shinozaki, H.Nishiie, S.Hirano, Prof. K.Martens, J.Liu, Prof. Y.Takeuchi, K.Otsuka, Prof. K.Nishijima, D.Motoki, Prof. S.Tasaka, Prof. S.Nakamura, I.Murayama, K.Fujii, Prof. Y.Fukuda, Prof. Y.Itow, Prof. K.Masuda, H.Uchida, Y.Nishitani, Prof. S.B.Kim, Prof. Y.D.Kim, Prof. Y.H.Kim, M.K.Lee, K.B.Lee, J.S.Lee.

I would like to thank to all other ICRR staffs who worked with me, Prof. T. Kajita, Prof. K. Kaneyuki, Prof. M. Shiozawa, Prof. Y. Hayato, Dr. M. Miura, Dr. Y. Obayashi, Dr. J. Kameda, Dr. K. Okumura, Dr. S. Nakayama, Dr. C. Saji, Dr. I. Higuchi, Dr. N. Tanimoto, Dr. Y. Shimizu, Dr. H. Kaji, Dr. A. Minamino, Dr. Y. Takenaga, Dr. G. Mitsuka, and Dr. H. Nishino. I am also deeply appreciative of my friends who supported me all the time, T.iida, M. Ikeda, C. Isihara, D. Ikeda, N. Okazaki, T.Sato, T. Tanaka, Y. Idehara, Y. Furuse, K. Ueno, Y. Nakajima, S. Hazama, D. Motoki, Y. Yokosawa T. Yokozawa, Y. Kozuma, H. Nishiie, A. Shinozaki, K. Iyogi, S.Hirano, T.F. McLachlan and Maggie.

Special thanks to Prof. A.Hitachi, M.Dziomba, Dr. J. Raaf and Dr. R. Wendell for their useful advices in writing this thesis. I would like to thank to SNOLAB scientists, Prof. C.J.Jillings, Prof. A.B.McDonald, Prof. M.G.Boulay, Dr. B.Cai, P.Pasuthip, W.H.Lippincott, Prof. T.Noble and Dr. O.Simard. They supported me at SNOLAB.

I gratefully acknowledge the financial support by the Japan Society for the Promotion of Science.

I would like to extend my gratitude to all the people who supported and encouraged me during my time in graduate school. Finally, I wish to express my deep gratitude to my friends and family.

Contents

1	Introduction	1
1.1	Existence of Dark Matter	1
1.2	Evidence from Cosmological observations	1
1.3	Local density of dark matter	3
1.4	Dark Matter candidates	4
1.4.1	Axion	5
1.4.2	WIMP	5
2	WIMP search	7
2.1	MSSM and neutralino	7
2.2	WIMP search by accelerator	8
2.3	WIMP indirect search	9
2.3.1	Antimatter	9
2.3.2	Muon neutrino	10
2.4	WIMP direct search	10
2.5	Review of direct detection experiments	13
2.5.1	DAMA/LIBRA experiment	13
2.5.2	XENON10	14
2.5.3	CDMS experiment	15
3	Liquid Xenon	16
3.1	The properties of xenon	16
3.2	Scintillation of xenon	20
3.3	Linear energy transfer	22
3.4	Relative scintillation efficiency	24
3.5	The advantages of Xenon	25
3.6	Pulse shape discrimination of liquid xenon	25
3.6.1	ZEPLIN	30
3.6.2	DAMA	33
3.6.3	LUX	35
4	XMASS experiment	37
4.1	Detector setup	37
4.1.1	Underground laboratory	37
4.1.2	XMASS detector	38
4.2	Low background techniques	42
4.2.1	Low background PMT	42
4.2.2	Material selection	47

4.2.3	Elution test	48
4.2.4	Distillation	51
4.2.5	Xenon circulation system	61
4.2.6	The energy and vertex reconstruction	61
4.2.7	BG MC	66
4.2.8	Neutron background	68
4.2.9	Expected sensitivity	69
4.3	Detector design and concept for $0\nu 2\beta$ search	73
4.4	Scintillation yield at room temperature	75
4.4.1	Experimental setup	75
4.4.2	Measurement	75
4.4.3	Comparison of the light yield	77
4.4.4	Expected sensitivity	80
5	Pulse shape discrimination of liquid xenon	82
5.1	Detector setup for pulse shape measurement	83
5.2	Gas line	87
5.3	Data Acquisition System	88
5.4	Gain and light yield calibration	88
5.5	Data reduction	93
5.5.1	Pre-activity cut	93
5.5.2	Saturation cut	96
5.5.3	Timing cut for neutron selection	97
5.5.4	Summary of the data reduction	98
5.6	PSD	100
5.6.1	Neutron data	100
5.6.2	Gamma-ray data	101
5.6.3	Optimization of the PSD parameter	102
5.7	PSD result	108
5.8	Spread of the <i>PSDratio</i> distribution	111
5.9	Light yield dependence of PSD	115
5.10	Decay time constant	127
5.11	Systematic error	131
6	Discussion	138
6.1	Comparison with other measurements	138
6.1.1	Comparison with ZEPLIN	138
6.1.2	Decay time constant	141
6.1.3	PSD using double phase detector	143
6.1.4	Comparison with S_2/S_1 method	146
6.1.5	Summary and value of PSD study in this thesis	148
6.2	PSD for the XMASS experiment	149
6.2.1	Effect of time of flight	149
6.2.2	The advantage of PSD for the XMASS experiment	151
6.2.3	Inelastic dark matter	157
7	Conclusion	158

A	Direct detection of WIMP	160
A.1	Total event rate	160
A.2	Cross section for the neutralino-nucleus scattering	163
A.2.1	Spin-Independent (SI) interaction	163
A.2.2	Spin-Dependent(SD) interaction	163
A.3	Nuclear form factor correction	165
A.4	Relative scintillation efficiency of nuclear recoils	165
A.5	The expected signal of dark matter	167
A.5.1	Dependence on target nucleus	167
A.5.2	Annual modulation	168

Chapter 1

Introduction

1.1 Existence of Dark Matter

The results of various astronomical observations show strong evidence for a large amount of dark matter in the universe. One piece of evidence for the existence of dark matter comes from measurements of the rotation curves of spiral galaxies. Fig. 1.1 shows the rotational curve for the spiral galaxy NGC6503 [1]. The rotation velocity (v_c) distribution of spiral galaxies expected from Kepler's law is

$$v_c(r)^2 = G \frac{M(r)}{r}, \quad (1.1)$$

where G is the gravitational constant, r is the radial distance from the center of the galaxy, and $M(r)$ is the total mass within the radius r .

The luminous matter extends no farther than about 5 kpc from the center of the galaxy. If the luminous matter is all there is, the rotation velocity will drop at large r . However the velocity stays flat even outside the luminous disk, which implies $M(r) \propto r$. This discrepancy points to the existence of non-luminous matter in the universe.

1.2 Evidence from Cosmological observations

From various observations, cosmological parameters such as the Hubble constant H_0 , the mass density parameter Ω_M , the baryon density parameter Ω_b and the total density parameter Ω_0 have been measured. It is convenient to represent matter and energy in the universe using density parameters Ω_i :

$$\Omega_i = \frac{\rho_i}{\rho_c}, \quad (1.2)$$

where ρ_c is the critical density, $\rho_c = 3H_0^2/8\pi G$. The total density parameter Ω_0 is represent the sum of the components Ω_i .

$$\Omega_0 = \sum_i \Omega_i = \Omega_M + \Omega_\Lambda \quad (1.3)$$

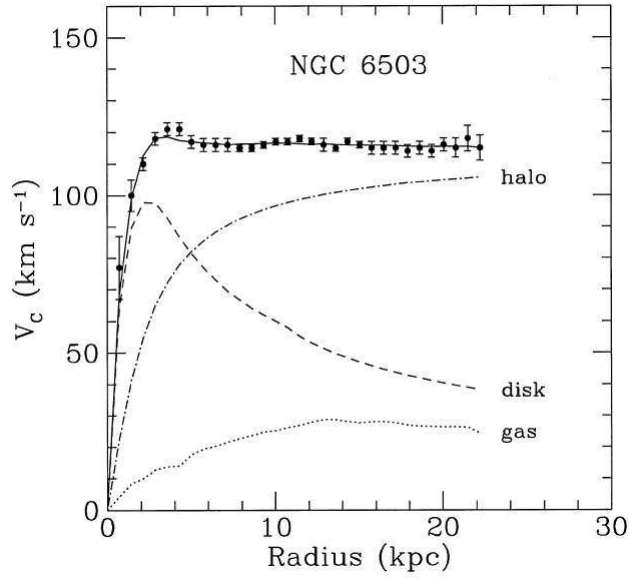


Figure 1.1: Rotation velocity curve for the spiral galaxy NGC6503. The points with error bars indicate the measured rotation velocity as a function of distance from the galactic center. The dashed and dotted curves are the contribution to the rotation velocity due to the observed disk and gas, respectively. The dash-dotted curve is the contribution from the dark halo [1].

where Ω_M and Ω_Λ show the contribution of matter and vacuum energy, respectively.

The value of the total density parameter Ω_0 can be estimated from Cosmic Microwave Background (CMB) radiation observations which study the power spectrum of the angular distribution. Ω_0 is directly related to the curvature of the universe. $\Omega_0 = 1$ shows a flat Universe, $\Omega_0 < 1$ shows an opened Universe and $\Omega_0 > 1$ shows a closed Universe. The CMB radiation is radiation left over from the big bang. This radiation is highly uniform across the sky, but there are tiny anisotropies associated with fluctuations of the matter density in the early universe.

The COBE satellite first detected the anisotropy in 1992, and the Wilkinson Microwave Anisotropy Probe (WMAP) reported a more accurate result [2]. The WMAP results determined cosmological model parameters like the matter density of the universe $\Omega_M h^2 = 0.1326 \pm 0.0063$ and the Hubble constant $h = 0.719 \pm 0.026$. In addition, the WMAP data and the deuterium observation data agree that the baryonic density is $\Omega_B h^2 = 0.02273 \pm 0.00062$, based on Big Bang nucleosynthesis(BBN) [3]. As a result, non-baryonic dark matter is required.

From the measurement of the distance-redshift relation obtained from the observations of Type Ia supernovae, it was shown that the expansion of the Universe is accelerating. This acceleration suggested an unknown type of energy, dark energy. The total energy density of the dark energy, Ω_Λ , is around 0.7 and the mass density Ω_M is around 0.3 for a flat cosmology ($\Omega_\Lambda + \Omega_M = 1$).

Gravitational instability and small fluctuations of the initial density field of the Universe caused the formation of the large-scale structure and the galaxy distribution in the current Universe. Thus the measurement of the distribution of the galaxy clusters investigated by the Sloan Digital Sky Surveys (SDSS) [4] can be used to determine the mass density of the universe. The SDSS result combined with the CMB anisotropy measurement by WMAP favors a low-density Universe with $\Omega_M = 0.30 \pm 0.04$.

Combining the high-redshift supernova survey, the galaxy cluster observations and the CMB, the normalized mass and energy densities Ω_M and Ω_Λ converge in the cosmological parameter space as shown in Fig. 1.2, which indicates an inflation model and flat cosmological models.

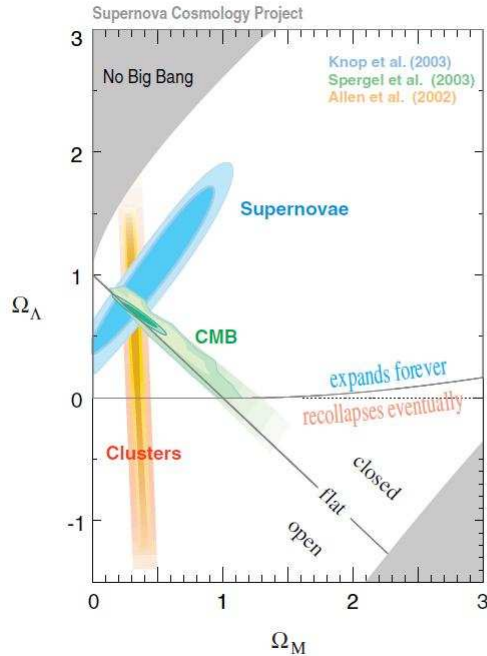


Figure 1.2: Cosmological parameter space from high-redshift supernova survey [5], galaxy cluster observation [6] and the CMB measurement [2].

1.3 Local density of dark matter

Dark matter exists in our universe. However, the density of dark matter around the earth should be known in order to detect dark matter on the earth. The local halo density ρ_0 and dark matter velocity distribution v_0 are needed to estimate the event rate for direct detection of dark matter. There is a large uncertainty in those values.

Therefore the dark matter direct detection community uses a simple model called the isothermal halo model. In determining ρ_0 and v_0 , the galactic rotation curve is the most important observational quantity. The rotation curve of our

galaxy can not be measured with the same precision as that of an external spiral galaxy, for instance NGC6503 in Fig. 1.1. However, assuming that our galaxy is an ordinary spiral galaxy like NGC6503, the rotation velocity of our galaxy increases linearly from zero at the center to roughly $v_c = 220\text{km/s}$ in the solar neighborhood and remains roughly flat all the way out to 25 kpc [7]. The observed rotation curve for our galaxy is shown in Fig.1.3.

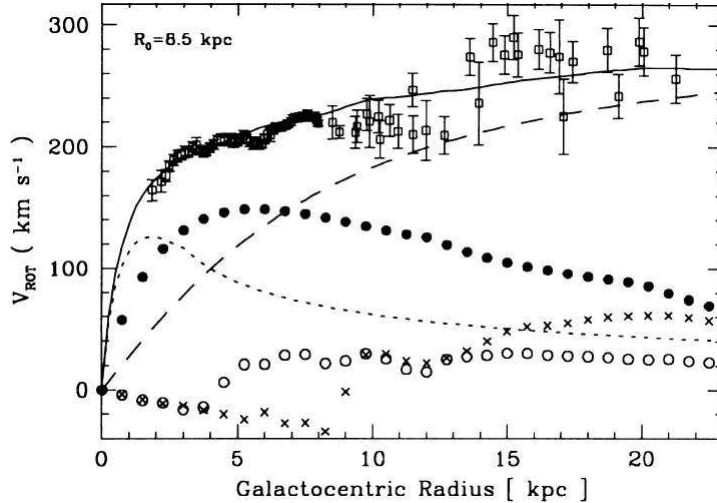


Figure 1.3: Rotational curve for our Galaxy [7]. The different lines represent the contributions from the bulge (dotted), the disk (filled circles), the HI layer (crosses), the H_2 layer (circles), and from the dark halo (dashed). The solid line represents the sum of the contributions.

In the isothermal halo, the shape of the rotation curve can be explained by assuming that the density distribution of the dark halo is given as,

$$\rho(r) = \frac{\rho_0}{1 + r^2/r_0^2}, \quad (1.4)$$

where ρ_0 and r_0 are fitting parameters. Using the observed rotation velocity in the solar neighborhood, the local halo density of dark matter is estimated to be

$$\rho(r) \sim 0.3\text{GeVc}^{-2}\text{cm}^{-3}, \quad (1.5)$$

with an uncertainty of a factor of two [8].

1.4 Dark Matter candidates

Cosmological and galactic observations indicate that non-baryonic dark matter exists with a density parameter of $\Omega_{DM} = 0.2-0.3$. The baryon density Ω_b is only 0.044. Non-baryonic dark matter is classified as Hot or Cold depending on whether it is relativistic or non-relativistic when those particles decoupled from the thermal equilibrium.

One of the candidates of Hot dark matter is the neutrino. However, the galactic cluster observation and WMAP results restrict the neutrino density Ω_ν to less than 0.024 [9]. It is also reported that hot dark matter can not explain the large scale structure of the universe, while cold dark matter reasonably reproduces the observed structure. Many candidates for Cold dark matter are proposed. In this section two Cold dark matter candidates which are most commonly discussed (Axion and WIMP) will be described.

1.4.1 Axion

The axion was originally proposed to solve the problem of why CP is not violated in quantum chromodynamics (QCD). Results from laboratory experiments and cosmology restrict the mass range of axions to $10^{-6}\text{eV} \leq m_a \leq 10^{-3}\text{eV}$ and $2\text{eV} \leq m_a \leq 5\text{eV}$. Axion with mass in the lighter range could be a candidate for Cold dark matter. The heavier axion is called Solar axion because it could be produced in the Sun.

The lighter axion has been searched for with the Sikivie radio frequency cavity technique. The mass range 2.3-3.4 μeV was searched but no significant axion signal was observed so far [10].

On the other hand the Solar axion has been searched for with superconduction magnet telescopes using the inverse Primakov effect [11]. The recent result from CAST [12] and the Tokyo helioscope group [13] imply upper limits on an axion coupling $g_{a\gamma} < 8.8 \times 10^{-11}\text{GeV}^{-1}$ for the axion mass of $m_a \leq 0.02\text{eV}$ at 95% C.L. and $g_{a\gamma} < 5.6 - 13.4 \times 10^{-10}\text{GeV}^{-1}$ for an axion mass of $0.84 < m_a < 1.00\text{eV}$.

1.4.2 WIMP

Weakly Interactive Massive Particles (WIMPs) are also one of the well motivated dark matter candidates. The WIMPs are implied by Supersymmetry (SUSY) which is an extended theory beyond the Standard Model of the particle physics.

SUSY theory introduces hypothetical symmetrical particles and solves the hierarchy problem in the standard model (SM). SUSY presupposes that each elementary particle with a spin j in the SM has a supersymmetric partner with a spin $|j - 1/2|$ as shown in Table 1.4.2.

These particles interact with ordinary particles only via gravity and any force weaker than the electromagnetic force. Since WIMPs are the main subject of this thesis, more details of the SUSY related WIMPs are discussed in the next chapter.

Standard model and Higgs particles			SUSY partners		
Symbol	Name	Spin	Symbol	Name	Spin
$q = u, c, t$	up quarks	1/2	$\tilde{q}_u^1, \dots, \tilde{q}_u^6$	up squarks	0
$q = d, s, b$	down quarks	1/2	$\tilde{q}_d^1, \dots, \tilde{q}_d^6$	down squarks	0
$l = e, \mu, \tau$	leptons	1/2	$\tilde{l}_1, \dots, \tilde{l}_6$	sleptons	0
ν_e, ν_μ, ν_τ	neutrinos	1/2	$\tilde{\nu}_1, \tilde{\nu}_2, \tilde{\nu}_3$	sneutrinos	0
g	gluons	1	\tilde{g}	gluinos	1/2
W^\pm	W bosons	1	$\tilde{\chi}_1^\pm, \tilde{\chi}_2^\pm$	charginos	1/2
H^\pm	charged Higgs	0			
γ	photon	1			
Z^0	Z boson	1			
$h^0 (H_2^0)$	light scalar Higgs	0	$\tilde{\chi}_1^0, \dots, \tilde{\chi}_4^0$	neutralinos	1/2
$H^0 (H_1^0)$	heavy scalar Higgs	0			
$A^0 (H_3^0, P_0)$	pseudoscalar Higgs	0			

Table 1.1: Particle spectrum in the SUSY model [14]. Particles with spin j in the SM have supersymmetric partners with spin $|j - 1/2|$.

Chapter 2

WIMP search

2.1 MSSM and neutralino

The minimal supersymmetric standard model (MSSM) contains all known fields, the standard model particles (SM) and an extra Higgs multiplet. The interaction in the theory is expressed by the gauge symmetry $SU(3) \times SU(2) \times U(1)$. The gauge groups in the standard model may be embedded into a simple group at some high energy scale, called grand unification. It turns out that the gauge coupling constants become equal at 2×10^{16} GeV given the MSSM particle content in Fig. 2.1. On the other hand, the three gauge coupling constants do not converge to one value even at high energy in the SM. This result supports the possibility of supersymmetric grand unification.

The interactions of SUSY particles with ordinary particles are governed by R-parity. R-parity is defined as,

$$R = (-1)^{3(B-L)+2S}, \quad (2.1)$$

where B and L are the baryon and lepton numbers and S is the spin. This means that $R = 1$ for ordinary particles and $R = -1$ for their superpartners. The lightest supersymmetric particle with $R = -1$, called LSP, must be absolutely stable. If the LSP is electrically neutral, it interacts only weakly with ordinary matter, and so can make an attractive candidate for non-baryonic dark matter.

The LSP in most cases is the lightest neutralino (χ), a linear combination of the supersymmetric partners of the photon, Z^0 , and neutral-Higgs bosons,

$$\begin{aligned} \tilde{\gamma} &= \cos \theta_W \tilde{B} + \sin \theta_W \tilde{W}^3, \\ \tilde{Z} &= -\sin \theta_W \tilde{B} + \cos \theta_W \tilde{W}^3, \end{aligned} \quad (2.2)$$

Thus, χ can be written as

$$\chi = N_1 \tilde{B} + N_2 \tilde{W}^3 + N_3 \tilde{H}_1^0 + N_4 \tilde{H}_2^0, \quad (2.3)$$

The neutralino mass matrix is written as

$$\begin{pmatrix} M_1 & 0 & -M_Z \cos \beta \sin \theta_W & M_Z \cos \beta \cos \theta_W \\ 0 & M_2 & M_Z \sin \beta \sin \theta_W & -M_Z \sin \beta \cos \theta_W \\ -M_Z \cos \beta \sin \theta_W & M_Z \sin \beta \sin \theta_W & 0 & -\mu \\ M_Z \cos \beta \cos \theta_W & -M_Z \sin \beta \cos \theta_W & -\mu & 0 \end{pmatrix} \quad (2.4)$$

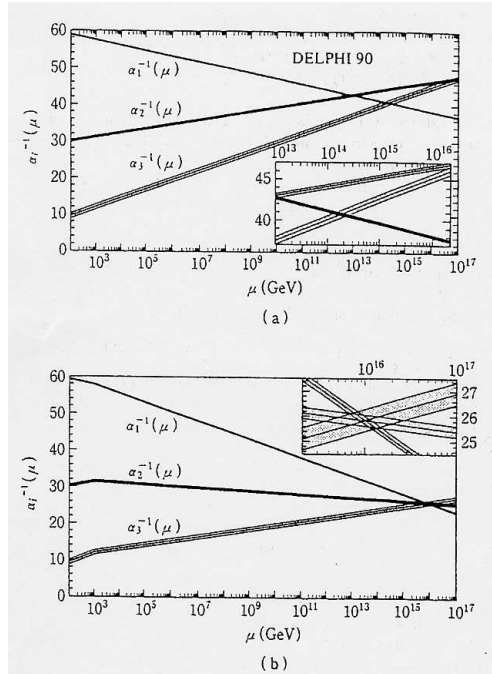


Figure 2.1: Three coupling constants in the Standard Model (SM) (a) and in the Minimal Supersymmetric Standard Model (MSSM) (b) [15]. Only in the latter case unification is obtained. α_1 , α_2 and α_3 are the $U(1)$ hypercharge, $SU(2)$ electroweak and $SU(3)$ strong couplings, respectively.

where M_1 and M_2 are the respective mass parameters of $U(1)$ gaugino (\tilde{B}) and the third component of the $SU(2)$ gaugino (\tilde{W}^3), μ is the higgsino mass parameter, $\sin^2 \theta_W$ is the weak mixing angle, M_z is the Z^0 boson mass, and the $\tan \beta \equiv v_2/v_1$ (v_1 and v_2 are the vacuum expectation values of the two Higgses). A useful parameter for describing the neutralino composition is the gaugino fraction,

$$f_g = |N_1|^2 + |N_2|^2, \quad (2.5)$$

If $f_g > 0.5$, then the neutralino is primary gaugino and if $f_g < 0.5$, then the neutralino is primary higgsino.

2.2 WIMP search by accelerator

Neutralino searches have been performed using accelerators, for example LEP2 at CERN [16]. Neutralinos could be produced in an e^+e^- collider through an s-channel virtual Z^0 , or through a t-channel scalar electron(\tilde{e}) exchange.

$$e^+e^- \rightarrow \tilde{\chi}_1^0 \tilde{\chi}_2^0 \text{ or } \tilde{\chi}_2^0 \tilde{\chi}_1^0, \quad (2.6)$$

where $\tilde{\chi}_1^0$ is the lightest neutralino and $\tilde{\chi}_2^0$ is the next-to-lightest neutralino.

The $\tilde{\chi}_2^0$ decays as follows,

$$\tilde{\chi}_2^0 \rightarrow \tilde{\chi}_1^0 \gamma \quad (2.7)$$

$$\tilde{\chi}_2^0 \rightarrow \tilde{\chi}_1^0 f \bar{f} \quad (2.8)$$

The $\tilde{\chi}_1^0$ will always produce a considerable missing energy and missing momentum signal. The lower mass limit of $\tilde{\chi}_1^0$ for a commonly chosen parameter set is 40 GeV from OPAL experiment. But a search for a neutralino with a lighter mass is still needed because the mass limit is calculated based on Grand Unified Theory.

The neutralino could also be produced in a hadron collider through various channels. The Tevatron collider searched for the neutralino at the center-of-mass energy of 1.96 TeV. It is expected that many SUSY particles will be produced at the Large Hadron Collider (LHC). Detectable neutralino events are expected from the production of heavier SUSY particles, which in turn decay via a multi-step cascade to the stable LSP. The LSP could be identified by missing mass in those interactions. The LHC experiment will either find a neutralino or give a much more stringent constraint on neutralino parameters [17].

2.3 WIMP indirect search

If WIMPs are majorana neutralinos, the annihilation of these neutralinos can occur and produce gamma rays or other particles. The annihilation channels are listed in Table 2.1.

The annihilations would occur mainly in the Sun, the earth and at the galactic center where the dark matter may be concentrated locally because of gravitational trapping.

	annihilation channel
$\chi\chi \rightarrow$	$f\bar{f}$
	W^+W^-
	Z^0Z^0
	W^+H^-, W^-H^+
	Z^0A^0
	Z^0H^0, Z^0h^0
	$A^0A^0, H^0H^0, h^0h^0, H^0h^0$
	A^0H^0, A^0h^0
	H^+H^-
	$g\bar{g}, q\bar{q}g$
	$Z^0\gamma, \gamma\gamma$

Table 2.1: Neutralino-neutralino annihilation channels [14]. Here f and \bar{f} are the standard model neutrinos, leptons and quarks, and A^0 are axions.

2.3.1 Antimatter

The annihilation of the neutralino will also produce antimatter such as positrons, antiprotons and so on. Recently an increase in the positron fraction in the

spectrum above 10 GeV has been reported by the PAMELA group [18]. The PAMELA detector uses a mounted superconducting spectrometer and calorimeters. According to [19], the annihilation of the neutralino may affect the spectrum above 10 GeV.

The PAMELA excess is a hot topic but the most common interpretation of the PAMELA excess is that the excess comes from standard astrophysical sources, like pulsars. Furthermore, a high annihilation cross section is required to reproduce the PAMELA excess.

2.3.2 Muon neutrino

A high energy neutrino signal from the Sun, Earth, or galactic center, where the WIMP density may be sufficiently enhanced because of the gravitational capture, may be detected because the trapped neutralino can annihilate and produce various particles.

The muon neutrino from the annihilation can escape from the gravitational trap and be detected by neutrino detectors at Earth such as Super-K or IceCube. The neutralino is indirectly detected as an upward-going muon because the neutrino from the annihilation may undergo a charged current interaction in the rock below the neutrino detector. The energy of the muon will typically be 1/3 to 1/2 of the neutralino mass [20].

2.4 WIMP direct search

The earth is moving in the dark matter halo with the speed of our solar system relative to that of our galaxy. As described in section 1.3 and Appendix A, we assumed that the dark matter exist in our universe with the velocity followed a Maxwell-Boltzmann distribution Eq.(A.4).

The WIMPs from the halo interact with normal matter by elastic scattering. Fig.2.2 and Fig.2.3 show the Feynman diagrams contributing to the spin independent and the spin dependent elastic scattering of neutralinos from quarks. The interaction signals are expected to provide information about the dark matter mass and the neutralino-quark cross section with some astrophysical assumptions.

The event rate of neutralino elastic scattering is quite low and the expected energy spectrum is approximately exponential. Fig.2.4 shows the event rate for the spin independent case. Ambient gamma rays and neutrons make false events which mimic neutralino scattering events. Therefore, in the direct detection experiments, it is very important to discriminate false events and reduce background events.

To reduce the backgrounds induced by cosmic rays, dark matter experiments have been running in deep underground laboratories. In addition, the neutralino event rate increases with lower recoil energy. So, a low energy threshold is required to detect dark matter.

The detection mechanisms of current dark matter experiments is described in Appendix A. In the case of spin independent interactions, the event rate is proportional to the square of the mass number (A^2) of the target nuclei as shown in Eq.(A.30). Therefore xenon, germanium and argon are effective nuclei to search spin independent interactions. On the other hand, in the case of spin

dependent interactions, the event rate is proportional to the square of the Lande factor (Λ^2) and the total spin of the nucleus ($J^2 + J$) as shown in Eq.(A.35). Isotopes such as ^{19}F and ^7Li have some of the biggest enhancement factors.

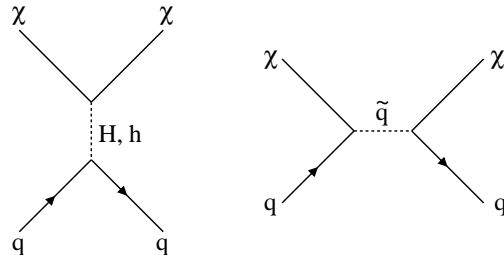


Figure 2.2: Feynman diagram of spin-independent interactions between a neutralino and a quark.

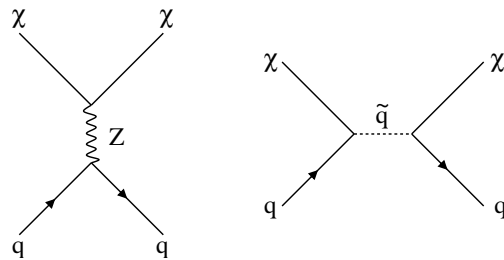


Figure 2.3: Feynman diagram of spin-dependent interactions between a neutralino and a quark.

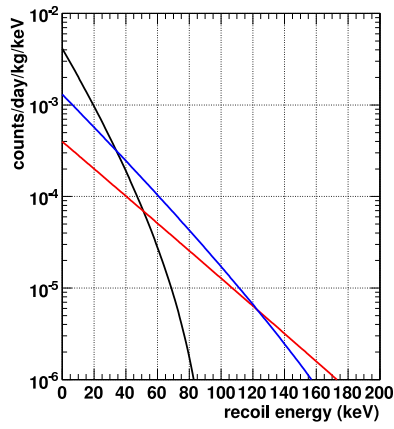


Figure 2.4: The expected event rate as a function of nuclear recoil energy for spin independent case. The neutralino mass M_χ and cross section $\sigma_{\chi-p}^{SI}$ is assumed 100 GeV and 10^{-43} cm². The black, red and blue lines show the expected event rate of Xenon, Argon and Germanium.

2.5 Review of direct detection experiments

In this section, several experiments searching for dark matter are reviewed. These experiments detect the energy deposition of the dark matter-nuclei scattering using scintillation photon, ionization or phonon signals. Key issues of those experiments are as follows.

- Low BG detector

It is very important to distinguish the dark matter signal from the background signal (BG). There are several techniques to reduce BG as follows:

1. To reduce contamination from radioactive impurities such as gamma rays, electrons, and neutrons in detector materials, materials are screened using a HPGe, an ICPMS before detector construction.
2. Operation at deep underground sites to reduce the effects of cosmic rays.
3. Shield to reduce the external radioactivity such as ambient gamma rays and neutron.
4. Development of particle identification using multiple sorts of signals from a single detector and the waveform of these signals.

The reaction of dark matter with xenon is observed as nuclear recoil event. On the other hand, the interaction of gamma rays and β rays with xenon, which is main BG for dark matter, is observed as an event of electron recoil. The discrimination between the nuclear recoil and electron recoil events is very useful for dark matter search experiments. In this thesis, one type of the fourth option for BG reduction, the possibility of particle identification using the scintillation waveform from a liquid xenon detector, is studied in detail.

- Low energy threshold

The event rate of WIMPs exponentially increases as lowering recoil energy. Therefore, it is required to construct detectors with as low energy threshold as possible.

- Large target mass

It is equally important to have a large exposure, i.e. a larger detector, to make a sensitive search for dark matter when low background and low energy threshold are realized. Currently, some ton scale detectors are being constructed and operated.

In the following subsections, the results of the experiments which claimed positive detection of dark matter and which gave highest sensitivity results are described only for spin independent interaction search. The results of the experiments which search for spin dependent interaction are excluded.

2.5.1 DAMA/LIBRA experiment

The DAMA/LIBRA group has searched for dark matter using 233kg NaI(Tl) scintillators. NaI(Tl) scintillators have a large amount of scintillation light yield

and can be produced with very few radioactive contaminants. They achieved an energy threshold of 2 keV_{ee} and $1.17 \text{ ton} \cdot \text{year}$ exposure, corresponding to 13 annual cycles as shown in Fig.2.5. They reported that their data provided model-independent evidence for the presence of dark matter in the galactic halo on the basis of an annual modulation signature with 8.9σ C.L. [23].

In particular, in the $2\text{-}6 \text{ keV}_{ee}$ energy range the modulation amplitude was $0.0116 \pm 0.0013 \text{ cpd/kg/keV}$, the measured phase was 146 ± 7 days and the measured period was 0.999 ± 0.002 year. However, other experiments like XENON10 and CDMS whose sensitivities were higher than that of the DAMA/LIBRA experiment could not confirm the DAMA/LIBRA result.

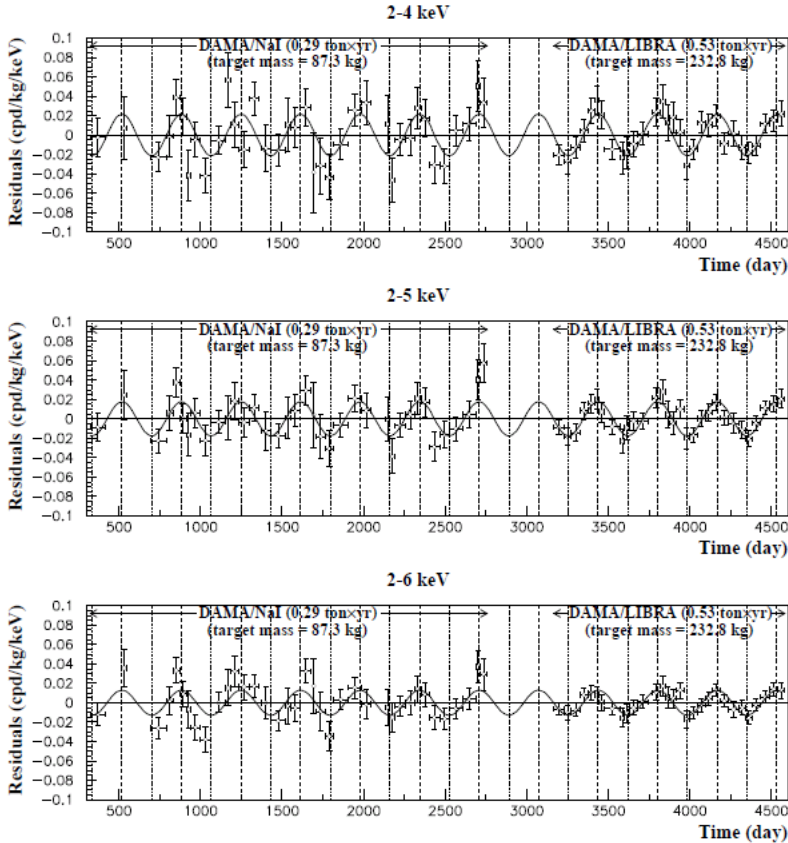


Figure 2.5: Residual rates measured by DAMA/LIBRA experiment [22].

2.5.2 XENON10

The XENON10 collaboration used liquid xenon in a double phase detector. The detector consisted of a liquid and a gas phase. By applying an electric field in the detector volume, the detector was operated as a time projection chamber (TPC).

The main method was the background rejection using the ratio of two types

of scintillation light. One is caused by energy deposition in the liquid phase, called primary signal (S1). The other is caused by drifting electrons in the gas phase called proportional light (S2).

They reported a result from 58.6 live days using a fiducial mass of 5.4kg. The positive results of the DAMA/NaI and DAMA/LIBRA experiments are thought to be inconsistent with this result. However, taking into account some other proposed effects, such as a channeling effect, they may not be inconsistent with each other. Further experimental study is needed. The XENON10 collaboration reported, a 90 % C.L. upper limit for the nucleon spin-independent cross-section of $8.8 \times 10^{-44} \text{cm}^2$ for a WIMP mass of 100 GeV/c² [25].

2.5.3 CDMS experiment

The CDMS collaboration used 19 Ge (230g) and 11 Si (100g) particle detectors operated below a temperature of 50 mK. The interaction of particles in the detectors deposits energy in the form of phonons and ionization. The ratio of the ionization to recoil energy is used to discriminate nuclear recoil signals from electron recoil signals. In addition, the timing parameters of phonon pulses are used to improve rejection power.

They observed two events in the signal region of dark matter. They estimated that the probability of observing two events from BG is 23% [26]. The CDMS collaboration reported, a 90 % C.L. upper limit for the nucleon spin-independent cross-section of $3.8 \times 10^{-44} \text{cm}^2$ for a WIMP mass of 70 GeV/c² [26].

Chapter 3

Liquid Xenon

In this chapter, various properties of liquid xenon as a scintillating material are described in detail.

3.1 The properties of xenon

The summary of liquid xenon properties is listed in Table 3.1. Fig.3.1 shows the phase diagram of Xe. Liquid xenon detectors are usually operated around 170 K using refrigerators or cryogen.

Fig.3.2 shows the attenuation coefficient of gamma rays in xenon. Because the atomic number of xenon is large the coefficient is large compared with other detector materials. In addition, the response of the gamma ray is fast compared to crystal scintillators. Because of these reasons, xenon is often used for gamma ray detectors.

Table. 3.2 shows the natural abundance of xenon. Radioactive isotopes with long lifetimes do not exist. The event rate for the spin independent interaction is larger than argon and germanium detectors because the atomic mass number is larger than in those detectors. Furthermore, as mentioned in Appendix A, the cross section of ^{129}Xe and ^{131}Xe for spin dependent interactions is large. With those advantages, xenon is considered to be a good target material for dark matter search. In addition, it should be noted that ^{136}Xe is one of the double beta decay nuclei.

Property	Value	Condition
Atomic number	54	
Mass number	131.29	
Boiling point	165.1 K	1 atm
Melting point	161.4 K	1 atm
Density	2.96 g/cm ³	161.5 K [27]
Radiation length	28.7 mm	in liquid [27] [28]
Scintillation wavelength	175nm	
Refractive index	1.61	177±5nm [30]
Decay time (recombination)	45ns	electron, gamma ray [31]
Decay time (singlet)	4.2ns	α [31]
Decay time (triplet)	22ns	α [31]
Rayleigh scattering length	30cm [32]	
Absorption length	≥ 100 cm [33]	

Table 3.1: Physical properties of liquid xenon.

Isotope	Abundance (%)
¹²⁴ Xe	0.096
¹²⁶ Xe	0.090
¹²⁸ Xe	1.92
¹²⁹ Xe	26.44
¹³⁰ Xe	4.08
¹³¹ Xe	21.18
¹³² Xe	26.89
¹³⁴ Xe	10.44
¹³⁶ Xe	8.87

Table 3.2: Isotopic composition of natural xenon [35].

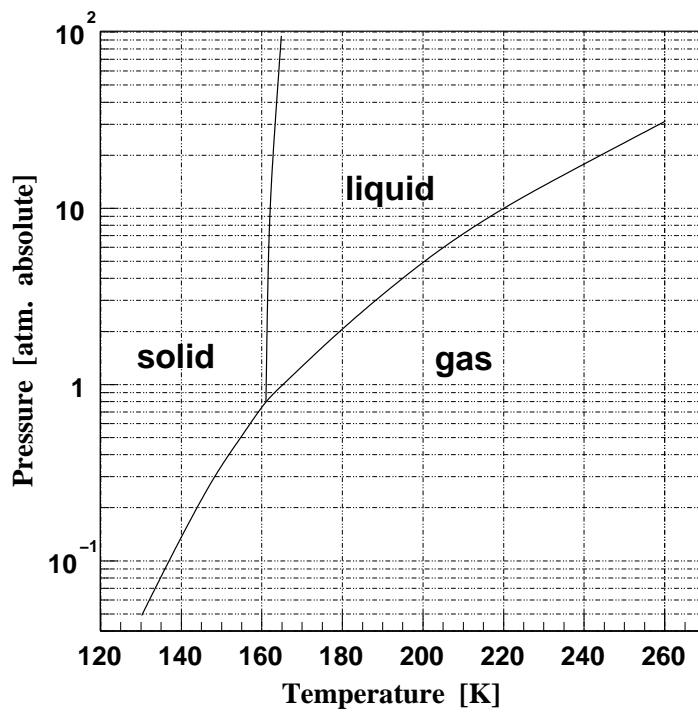


Figure 3.1: Phase diagram of xenon.

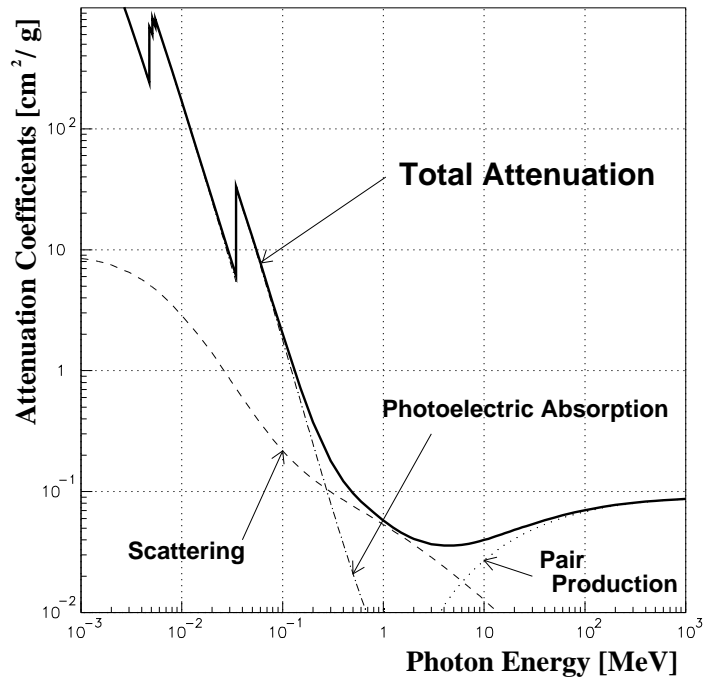


Figure 3.2: Attenuation coefficients of γ -rays in xenon [34].

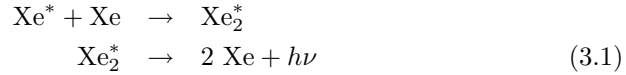
3.2 Scintillation of xenon

In noble gases like neon, argon and xenon, scintillation light is produced by the deexcitation of dimer states. The scintillation process of xenon is shown in Eq.3.1 and Eq.3.2. Fig.3.3 shows the process of the liquid xenon, liquid argon and liquid krypton scintillation.

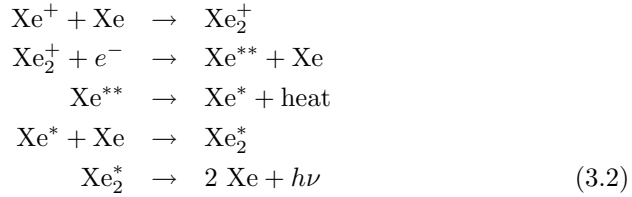
The scintillation mechanism is classified into two processes determined by whether or not the process includes recombination. The process including recombination starts with an ionization process. At first step the ionizing charged particles produce electron-ion pairs. Then the electrons are thermalized. The ions are also localized and make formation of molecular ions (Xe_2^+). The recombination of the free electrons and molecular ions occurs and make excitons of xenon (Xe_2^*). The self-trapping excitons form excited molecules. Finally a de-excitation of the excited molecules emits scintillation photons.

The de-excitation has two components called singlet component and triplet component. The singlet component is caused by a spin singlet state($^1\Sigma_u^+$), and the triplet component is caused by a spin triplet state($^3\Sigma_u^+$).

the process without recombination



the process with recombination



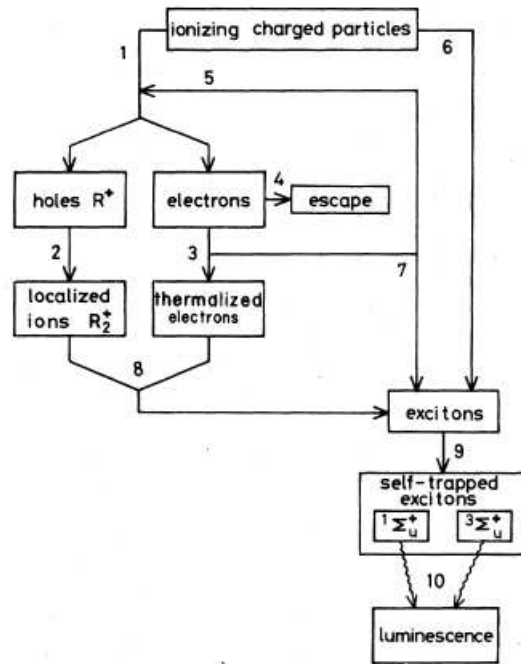


Figure 3.3: The scintillation process of noble gas (argon, krypton and xenon). 1. production of electron-ion pairs. 2. Formation of molecular ions (R_2^+). 3. Thermalization of hot electrons. 4. Escape of hot electrons from the Coulomb attraction of R_2^+ ions. 5. Production of electron-ion pairs by secondary electrons. 6. Production of excitons by the ionizing particle. 7. Production of excitons by secondary electrons. 8. Recombination of free electrons and molecular ions forming excitons. 9. Self-trapping of excitons forming excited molecules. 10. De-excitation of excited molecules emitting scintillation photons. [36].

3.3 Linear energy transfer

The energy deposited by radiation is used to produce electron-ion pairs, excited atoms and free electrons with a kinetic energy smaller than the first excited level known as sub-excitation electrons. In the case where the energy (E) is deposited in the liquid xenon by ionizing radiation, the maximum scintillation yield is given by E/W_{ph} , where W_{ph} is the average energy required to produce a single photon.

The scintillation yield depends on the linear energy transfer (LET), that is the density of electron-ion pairs produced along the track of a particle. As the density of the electron-ion pairs increases, the recombination probability between electrons and ions increases. Therefore, scintillation yield depends on LET.

Fig.3.4 shows the LET dependence of scintillation yield in liquid xenon for various ionizing particles. In the low LET region, the relative scintillation yield decreases as the LET decreases. According to the Onsager model [37], if the electron produced by the ionizing particle is thermalized within the Onsager radius, the electron recombines with parent ion.

On the other hand some electrons escape from the influence of parent ions, called escape electrons. In case of liquid xenon the thermalization range of electron is estimated 4000-5000nm and the thermalization range is beyond the Onsager radius (49nm). Therefore, many electrons escape from the influence of parent ions and can not recombine with parent ions for an extended period time (more than 1 msec). Therefore the relative scintillation yield decreases.

The scintillation intensity per unit absorbed energy, dL/dE , is given [38],

$$dL/dE = \frac{A(dE/dx)}{1 + B(dE/dx)} + \eta_0 \quad (3.3)$$

where dL/dE is normalized to the maximum scintillation yield, that is, in the limit of $dE/dx \rightarrow \infty$, dL/dE becomes $A/B + \eta_0 = 1$. A , B and η_0 are adjustable parameters and η_0 means the scintillation yield at zero electric field in the limit of zero LET. The $W_{ph}(\text{max})$ is estimated to be 13.8 eV and the W_{ph} value for electrons is estimated to be 21.6 eV [38].

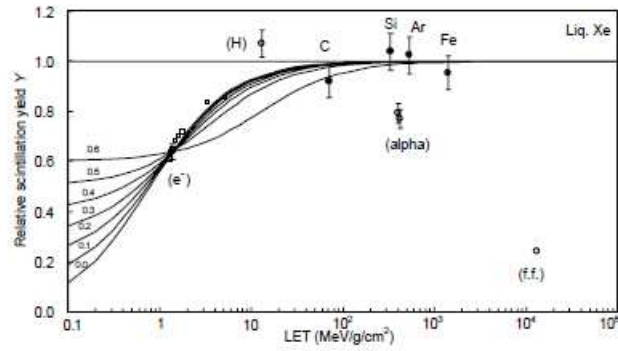


Figure 3.4: The LET dependence of the scintillation yield curves in liquid xenon. Solid circles represent yield for relativistic heavy particles where as open circles represent those for electrons, alpha particles and fission fragments. Open squares represent gamma ray data. Solid curves are obtained from Eq.3.3 using several values of η_0 .

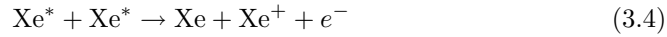
3.4 Relative scintillation efficiency

The electron-ion pair density of nuclear recoils is higher than that of electron recoils with same energy. Therefore the scintillation yield is different for electron recoils and nuclear recoils.

The ratio of scintillation yield between these two types of recoils is called the relative scintillation efficiency (L_{eff}). Since the WIMPs scatter off the xenon nucleus, it is very important to measure L_{eff} . L_{eff} of liquid xenon was measured by many experimental groups and the results are shown in Fig.3.5. As mentioned in chapter 2, the event rate of WIMPs exponentially increases at lower energy. Recently L_{eff} was measured for less than 5 keV_{nr} nuclear recoil. At 5 keV_{nr} L_{eff} is about 0.11 and in the higher energy region up to 50 keV_{nr} L_{eff} is constant at around 0.2 from a global fit to all measurements.

The scintillation yield of nuclear recoils is lower than that of electron recoils due to the nuclear quenching treated by Lindhard [39]. In case of nuclear recoil, most of the recoil energy is used for molecular oscillation (heat).

In addition, the particles that produce high LET, such as non-relativistic protons, fission fragments and neutrons, reduce the scintillation yield because of higher excitation densities. As shown in Fig.3.4 fission fragments reduce the scintillation yield. Because of the high density of excitation, the collisions between two free excitons can occur [40].



The electron loses its kinetic energy very rapidly before recombination. This process reduces the number of excitons available for scintillation.

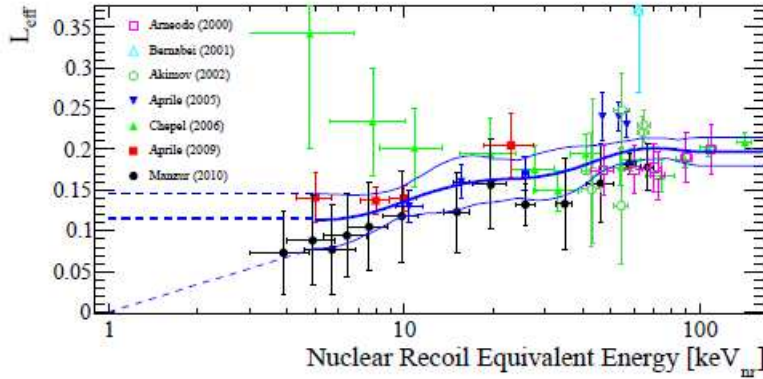


Figure 3.5: The relative scintillation efficiency of nuclear recoil. The solid lines show the global fit to all L_{eff} measurements between 5 keV_{nr} and 100 keV_{nr}, together with 90 % confidence contours. The dashed lines show extrapolations to lower energy [41].

3.5 The advantages of Xenon

Liquid xenon is used for radiation detectors because of its many advantages.

Liquid xenon has a large scintillation yield of 46000 photon/MeV. The event rate of dark matter increases exponentially as the energy threshold is lowered. Thanks to the large photon yield, we can set a low energy threshold and achieve good sensitivity.

In addition, the atomic number of xenon is large ($Z = 54$). Gamma rays are strongly attenuated. If the fiducial volume is restricted to the central region of the detector, low BG is achieved. This self-shielding effect of liquid xenon is a key idea of the XMASS experiment.

Xenon does not have a radioactive isotope with a lifetime longer than a couple of months. The longest lifetime isotope is ^{127}Xe ($\tau_{1/2}=36.4$ days) which decays through electron capture with a Q value of 0.664 MeV. This energy is much larger than the energy of the dark matter signal.

In the case of argon, ^{39}Ar is a radioactive isotope with a long lifetime. It β -decays with $E_{max} = 565\text{keV}$. Therefore ^{39}Ar is the main BG for a dark matter search using liquid argon. So xenon has a clear advantage over argon with respect to cosmogenic backgrounds.

Furthermore, the wavelength of the liquid xenon scintillation is 175nm which can be detected directly using PMTs without wavelength shifters. In the case of liquid argon it is impossible to detect the liquid argon scintillation with PMTs directly because the wavelength is 128nm.

3.6 Pulse shape discrimination of liquid xenon

One of the main topics of this thesis is the detailed study of the pulse shape discrimination for dark matter experiments. The relevant energy for dark matter experiments is around 5-20keV. Various studies of pulse shape discrimination have been done in the world so far, but they are either at higher energy or insufficient data for the recent high sensitivity dark matter experiments. In this section, those previous studies are reviewed with some comments on their differences with the study in this thesis.

Before describing previous studies, the principle of the pulse shape discrimination is discussed based on the fundamental mechanism of the scintillation production. Fig.3.6 shows the schematic illustration of the spread of the Xe_2^+ - e^- pairs produced by the energy deposition in liquid xenon. In the case of electron recoil events, the dE/dx of an electron is small and the Xe_2^+ - e^- pairs spread widely. On the other hand, because of large dE/dx in the case of nuclear recoil events, the Xe_2^+ - e^- pairs are produced with high density.

As described in section 3.2, the scintillation mechanism is classified into two processes determined by whether or not the process includes recombination. In the case of nuclear recoil events, since the density of Xe_2^+ is high, the Coulomb attraction is strong. Therefore the electron recombines with Xe_2^+ rapidly before the electron is thermalized. The pulse shape may be determined by the lifetimes of singlet (4 nsec) and triplet (22 nsec) state of Xe_2^* as described below. On the other hand, in the case of electron recoil events, the recombination occurs after the electron is thermalized because of the weak Coulomb attraction. Therefore the recombination of electron is very slow. For this reason, a difference in pulse

shape between electron recoil and nuclear recoil events may arise.

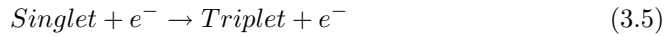
The pulse shapes for electrons and α particles are reported in [31]. Fig.3.7 shows the pulse shape for 1 MeV electrons and 5.3 MeV α particles. In the case of α particle, two components of the lifetime were observed. The lifetimes for singlet and triplet states were about 4 nsec and 22 nsec. On the other hand, in case of electron recoil the two components were not observed and only one component with 45 nsec was observed.

The slow component of electron recoil is treated as the decay time of a triplet state in [42]. However, it is reported that this pulse shape difference is caused by the process of recombination in other papers [40] [43] [44].

The hypothesis that the decay time of electron recoil events is determined by the the recombination was confirmed by measurements with electric field. When an electric field is applied, this slow component is not observed and the two components of the singlet and the triplet are observed as shown in Fig.3.8 [36] [43]. The pulse shape of electron recoil is very close to nuclear recoil in an electric field of 4 kV/cm. Due to the electric field, the electrons in the process of recombination shown in Fig.3.3 are removed from the scintillation process. Therefore, it is strongly suggested that the slow component of 45 nsec is due to recombination at zero electric field.

In the low energy region around 5 keV, the decay time constant of electron recoil events was decreased to 35 nsec which will be described in section 5.10 . This may be caused by the difference of the dE/dx . The dE/dx of low energy electrons is larger than that of high energy electrons. The density of $\text{Xe}_2^+ - e^-$ pairs increases as the energy of electron decreases. Therefore it was observed that the decay time constant decreases as the deposited energy of electron recoil decreases. Since this discussion is the main topic of this thesis, more detail will be discussed later.

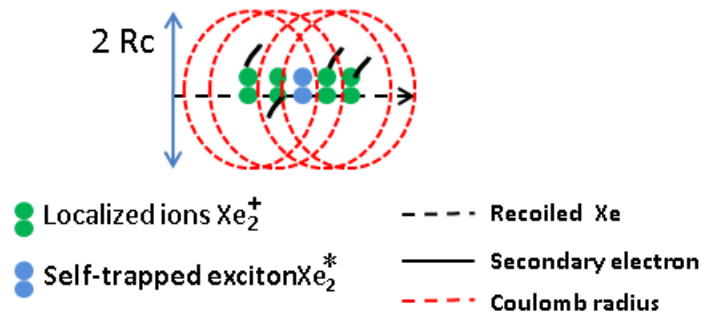
The difference of the number of single and triplet states was reported in [40]. Since the recombination of electron recoil events is very slow, the number of triplet states of electron recoil may be larger than that of nuclear recoil by the following reaction [40].



The reverse process is not likely because of the energy difference of the singlet and triplet states.

The pulse shape studies performed by ZEPLIN [45], DAMA [46] and LUX [44] are described in the following sections.

Nuclear recoil (a)



Electron recoil (b)

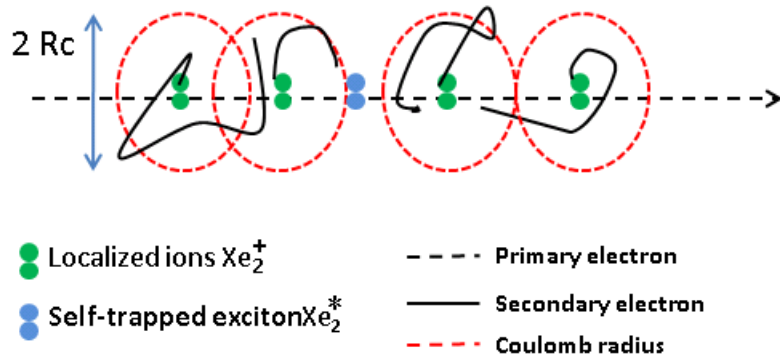


Figure 3.6: The schematic illustration of the spread of local $\text{Xe}_2^+ - e^-$ pairs for nuclear recoil and electron recoil event. The nuclear recoil event in liquid xenon is shown at top (a). The electron recoil event of gamma ray is shown at bottom (b). The red circle shows Coulomb radius Rc (40 nm) [36]. The Coulomb radius defined as the distance from the positive ion at which the Coulomb energy is equal to the thermal energy of electron. The black solid line shows the secondary electron track. The track length of electron recoil is longer than that of nuclear recoil.

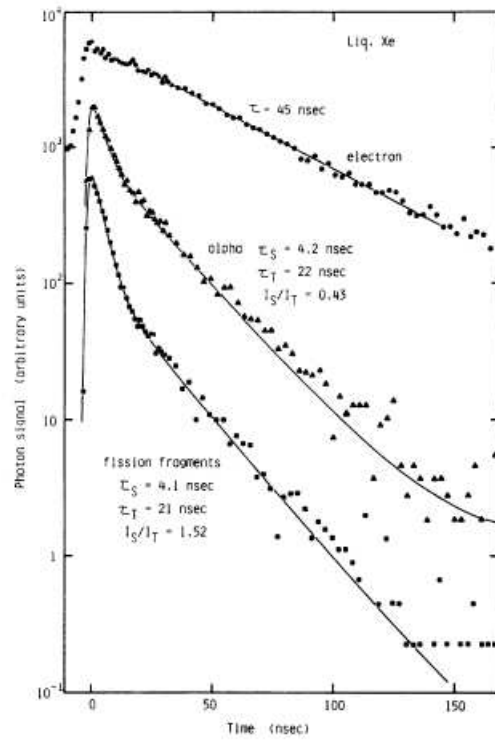


Figure 3.7: Decay curves of the scintillation light obtained for liquid xenon excited by electrons, α particles and fission fragments [31].

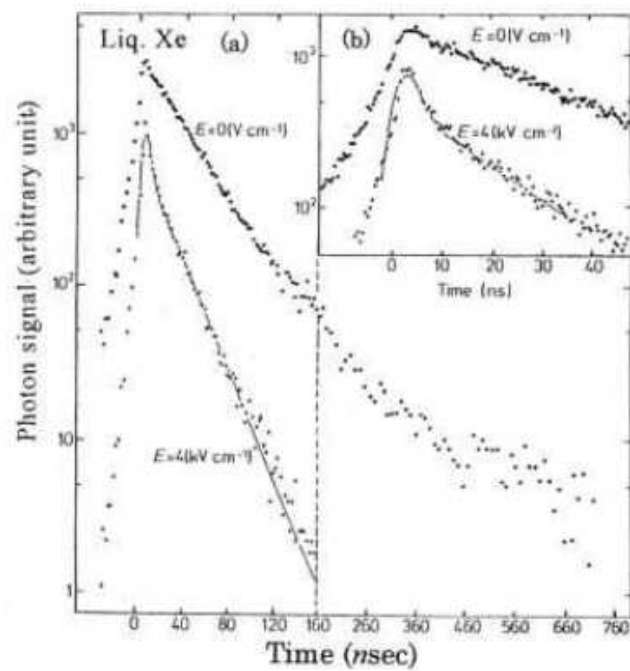


Figure 3.8: Pulse shape of liquid xenon with and without a 4 kV/cm electric field. The long time scale and short time scale are shown in (a) and (b), respectively [36] [43].

3.6.1 ZEPLIN

ZEPLIN studied pulse shape using the 5 kg single phase liquid xenon detector as shown in Fig.3.9 [45]. The scintillation light of liquid xenon was detected using the three 8cm PMTs. The light yield of the detector was 2p.e./keV (about one order of magnitude smaller than the value of the setup in this thesis).

They used the average scintillation time τ_m as the PSD parameter which is defined as the time difference between 90% and 5% points with respect to the maximum pulse height. The results of neutron and electron recoils are shown in Fig.3.10. As a result of this study, they argued that the events near 10 nsec were neutron events and the events near 20 nsec were electron recoil events in Fig.3.10(a).

However there are some doubts in this result and a critical paper [47] was published. One of the doubts is that ZEPLIN applied a noise cut which rejected events with $\tau_m < 10$ nsec and detected p.e. > 2.5 p.e. on any each PMT. Therefore the noise cut might strongly influence nuclear recoil events.

In addition, the number of nuclear recoil events is very small, less than 10 events while the number of background gamma ray events is more than 250 events. Since the electron and nuclear recoil events are not separated, the tail events of neutron run are fitted by a generalized gamma density distribution Eq.(3.6) (3.7) which may not be correct for nuclear recoil signals.

$$\frac{1}{N_T} dN/d\tau_m = G(x, \alpha, \beta) = (1/\beta^\alpha \Gamma(\alpha)) x^{\alpha-1} \exp(-x/\beta) \quad (3.6)$$

$$G(x, \alpha, \beta) = G(\tau_0/\tau_m, 1 + 1/w, w) \quad (3.7)$$

where N_T is the total number of events in the distribution, τ_0 is the peak of the distribution and w is a single parameter characterizing the width.

On the other hand, the neutron data taken in this thesis have much less gamma ray contamination(<10%), which will be described in detail in chapter 5. In addition, the PSD analysis was performed independently for neutron and gamma ray data. In chapter 6, results of a PSD analysis on the data in this thesis using the same analysis method as ZEPLIN are presented. But the difference of τ_m which they argued was not confirmed.

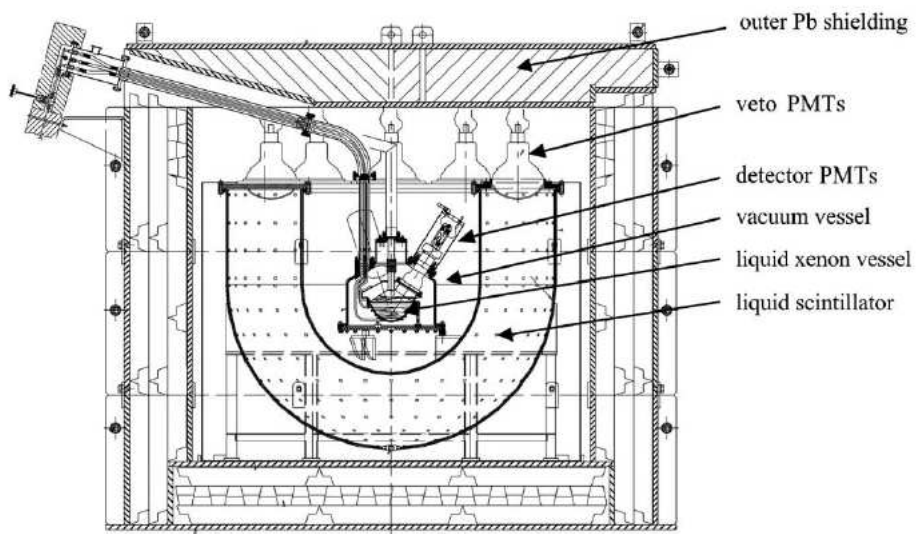
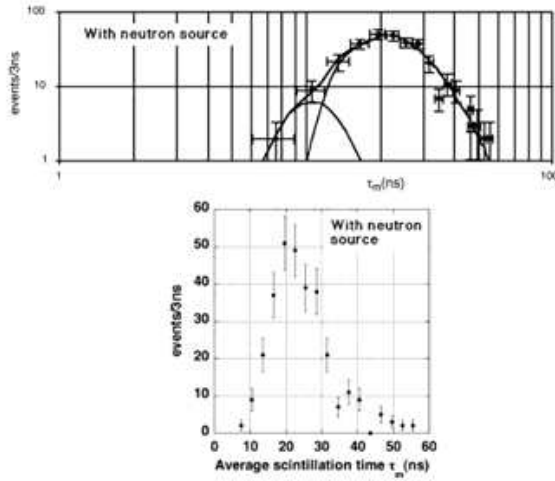
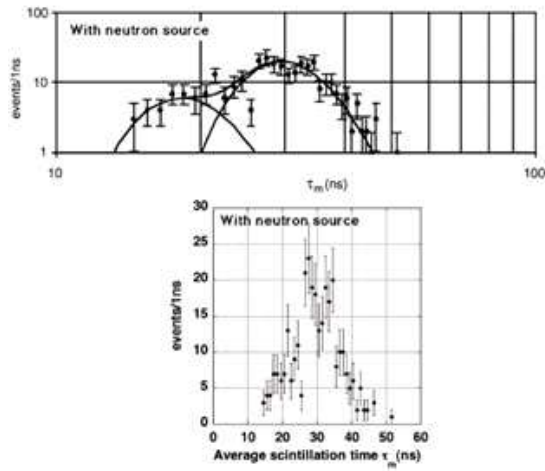


Figure 3.9: The setup of the ZEPLIN detector.

(a) Am-Be source Run 3-8keV



(b) Am-Be source Run 20-30keV



(c) Co60 Run 3-7keV

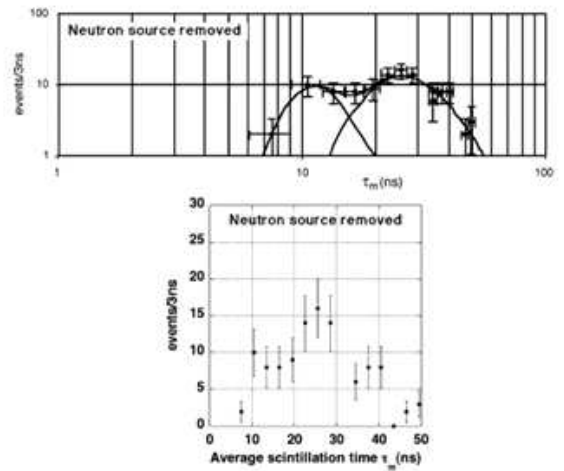


Figure 3.10: Distributions of the average scintillation time τ_m [45] [47]. (a) the Am-Be neutron run without tagging gamma ray at 3~8keV, (b) the Am-Be neutron run with tagging gamma ray at 20~30keV, and (c) the ^{60}Co gamma ray run at 3~8keV. For each distribution the linear scale figure is shown in the bottom position of the figure. It was argued by ZEPLIN that the events near $\tau_m \sim 10$ nsec in (c) are due to ambient neutrons.

3.6.2 DAMA

DAMA studied pulse shape using a 40 cc liquid xenon detector. The scintillation light of liquid xenon was detected using a PMT. They compared the average wave forms of nuclear recoil and electron recoil events above 10keV [46]. They did not discuss wave forms on an event by event basis. They accumulated many events for each recoil category and obtained averaged wave form because the light yield was not enough to analyze event by event basis. The τ for each average wave form was calculated as

$$\tau = \frac{\sum_i h_i t_i}{\sum_i h_i} \quad (3.8)$$

$$h_i = \frac{\sum_j c_{ji}}{N} \quad (3.9)$$

where t_i is the i-th time bin and h_i is the average pulse height of the i-th time bin, and c_{ji} is the pulse height of the j-th pulse in the i-th time bin. They evaluated the discrimination quality factor DQF . It is defined as a function of the relative difference between electron recoil (τ_{comp}) and nuclear recoil (τ_{rec}):

$$DQF = \frac{\tau_{comp} - \tau_{rec}}{\tau_{comp}} \quad (3.10)$$

Fig.3.11 shows DQF for each energy range. In the lowest energy bin, the DQF value is 7%. However it is consistent with zero at ~ 1.5 standard deviations. It should be noted that the lowest energy bin (10 - 15 keV) is the most important energy bin for dark matter search.

The average pulses of many electron and nuclear recoil events are compared in DAMA's PSD analysis. As mentioned above, PSD is not discussed at event by event basis. They only analyzed the center value of τ and they didn't evaluate the spread of τ value for those events. In addition, in the case of dark matter search, the event rate of dark matter is enhanced at low energy. Therefore PSD is required at low energy. In our PSD analysis, PSD is achieved for event by event down to 5keV as shown in chapter 5 while the DAMA result is above 10keV.

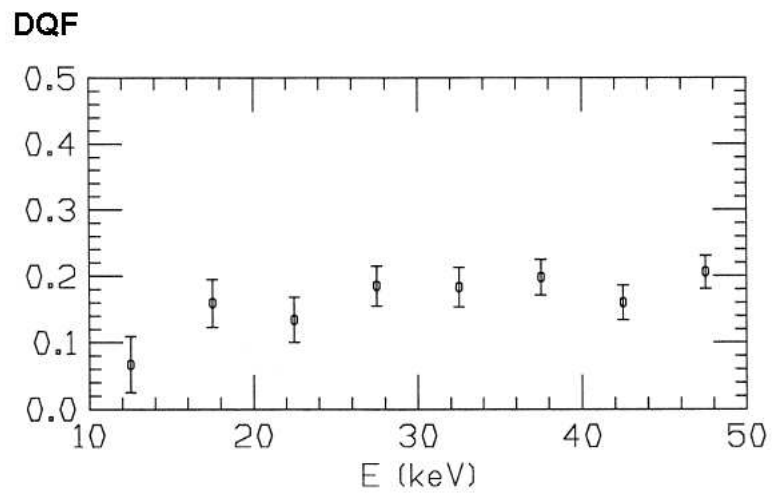


Figure 3.11: DQF distribution as a function of the energy [46].

3.6.3 LUX

The LUX group reported the PSD of liquid xenon using double phase detector consists of gas and liquid phase of xenon in August 2009 [44]. The detector consisted of a gas and a liquid phase using two PMTs as shown in Fig.3.12. The light yield was obtained to be ~ 5 p.e./keV from a ^{57}Co source (122keV) measurement at zero electric field. The PSD analysis was performed using the ratio of prompt to total signal at a drift electric field of 0.06kV/cm. The neutron events were selected using the ratio between primary scintillation (S1) in liquid phase and proportional scintillation (S2) in gas phase. The PSD analyzed using the ratio of prompt/total (fraction of light at the head of the pulse). The PSDratio is defined as

$$PSDratio = \frac{\int_{t_i}^{t_0+t_{window}} S(t)dt}{\int_{t_i}^{t_f} S(t)dt} \quad (3.11)$$

where $S(t)$ is the signal, t_{window} is the prompt window size (10 nsec), $t_i = t_0 - 50$ nsec, $t_f = t_0 + 300$ nsec and t_0 is the leading edge. The leading edge was defined as the time when the pulse reaches 10% of the maximum amplitude. They studied the mean value of PSDratio and the spread of PSDratio. Fig.3.13 shows the rejection power using PSD at double phase detector.

LUX group studied PSD only at the light yield of ~ 5 p.e./keV. On the other hand, this thesis discuss PSD with 20 p.e. /keV which is four times larger light yield. For example, light yield at 5 keV is 25 p.e. in the LUX setup while 100 p.e. in this thesis. So, PSD can be discussed with much smaller statistical error in this thesis. In addition, the light yield dependence of PSD is also discussed in this thesis.

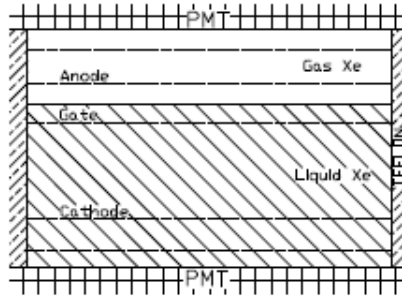


Figure 3.12: The setup of the PSD measurement [44].

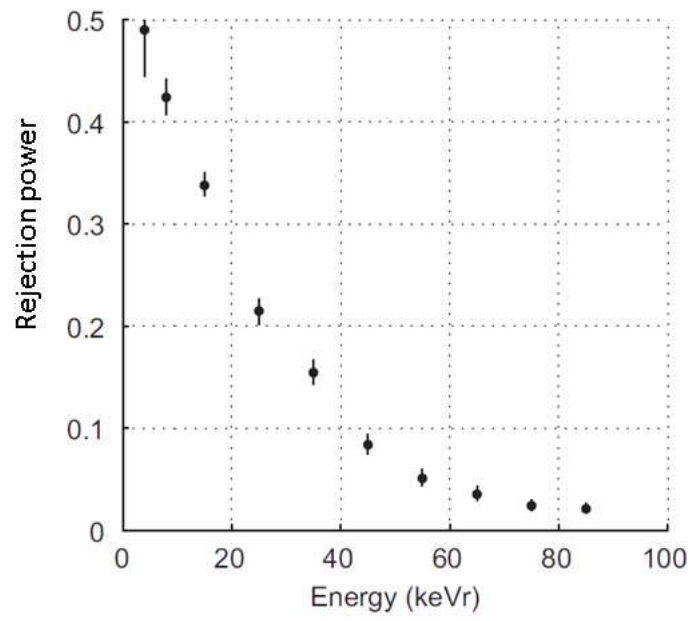


Figure 3.13: The rejection power as a function of energy for the data set taken with a drift electric field of 0.06kV/cm [44].

Chapter 4

XMASS experiment

The XMASS experiment was proposed in 2000 [48]. The physics targets of XMASS are the detection of dark matter, pp and ${}^7\text{Be}$ solar neutrinos and neutrino less double beta decay ($0\nu 2\beta$).

As a R&D of the XMASS experiment, a 100kg prototype liquid xenon detector was constructed with which developments for the detection techniques were performed. The aims of the prototype detector were confirmation of event reconstruction, the self shielding effect and background properties.

Based on this R&D, a 1 ton scale detector was constructed starting in 2007. In section 4.1 and 4.2 the setup of the 1 ton detector and low background techniques are described, respectively. As you will see in these sections, the 1 ton detector was designed to achieve quite low radioactive background level which corresponds to two orders of magnitude better than the current best detector in the world.

The basic idea of background reduction in the 1 ton detector is self-shielding by liquid xenon. However, at the higher energy relevant to $0\nu 2\beta$ of ${}^{136}\text{Xe}$ (i.e. at 2.5MeV), the self-shielding does not work well. So, different detector setup is necessary for the $0\nu 2\beta$ experiment. We have designed a detector setup using high pressure xenon at room temperature. In section 4.3, the detector design for $0\nu 2\beta$ search and scintillation yield of liquid xenon at room temperature are described.

4.1 Detector setup

4.1.1 Underground laboratory

The XMASS detector is being constructed in the Kamioka Mine. The depth of the Kamioka Mine is 2700m.w.e.(meter water equivalent). Table.4.1 shows the muon flux, thermal neutron flux, non-thermal neutron flux, the amount of radon and the gamma ray flux in the Kamioka Mine.

The muon rate is 5 orders of magnitude smaller than that at the surface. An experimental hall for the XMASS experiment was excavated at 200m north of the Super-Kamiokande.

	Surface	Kamioka Observatory
μ [$\text{cm}^{-2} \text{s}^{-1}$] [49]	1.1×10^{-2}	$\sim 10^{-7}$
Thermal neutron [$\text{cm}^{-2} \text{s}^{-1}$]	1.4×10^{-3} [50]	8.3×10^{-6} [51]
Non-thermal neutron [$\text{cm}^{-2} \text{s}^{-1}$]	1.2×10^{-2} [50]	1.2×10^{-5} [51]
Rn [Bq/m^3] (Summer) [52]	40	1200
Rn [Bq/m^3] (Winter) [52]	40	40
$\gamma(> 500\text{keV})$ [53]	-	0.71 / cm^2/s

Table 4.1: Environmental background sources and their intensity at the Kamioka Observatory

4.1.2 XMASS detector

Fig.4.1 shows the schematic view of the XMASS detector. Fig. 4.2 and Fig.4.3 show pictures of the XMASS detector. The detector consists of an inner vessel chamber (IVC) and outer vessel chamber (OVC) made from OFHC copper. The volume in the OVC is kept under vacuum in order to prevent heat flow from the outside.

The IVC contains 1 ton of liquid xenon and 642 hexagonal 2inch PMTs (630 R10789-11s and 12 R10789-11MODs). The PMTs are mounted in triangle shaped holders. Five triangle holders build up one pentagon. 12 pentagons build up a pentakisdodecahedron. The photocathode coverage is 63.4%.

About 800 kg of liquid xenon is filled in the volume inside the PMT photocathode plane, which has a radius of 40 cm. The fiducial volume is the inner 20 cm in radius from the center and the mass of the fiducial volume is 100kg. Fig.4.4 shows the basic structure of the PMT holder made of OFHC copper. The holder works also as a filler to save xenon outside of the photocathode plane. More filler made of OFHC copper fills the space between the PMT holder and the IVC. Radioactivity of all materials in the detector was measured using Germanium detectors in the Kamioka Mine. The result of material screening is described in section 4.2.2.

Fig.4.5 shows the water tank in which the XMASS detector occupies the center. The diameter of the tank is 10m and its height is 11m. Pure water is filled in the tank. The water tank performs as a radiation shield for ambient neutrons, gamma rays and cosmic rays. 72 20-inch-PMTs are mounted on the inner surface of the water tank to veto cosmic ray muons.

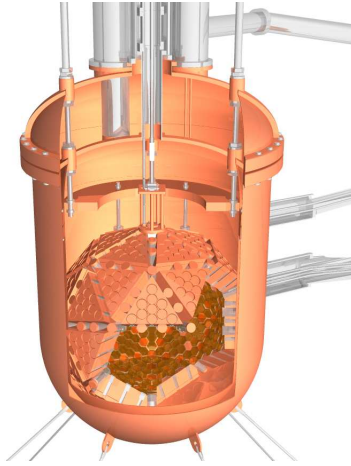


Figure 4.1: The schematic view of the XMASS detector.



Figure 4.2: The picture of installed PMTs and PMT holder.



Figure 4.3: The picture of the detector. 642 PMTs was installed to PMT holder.

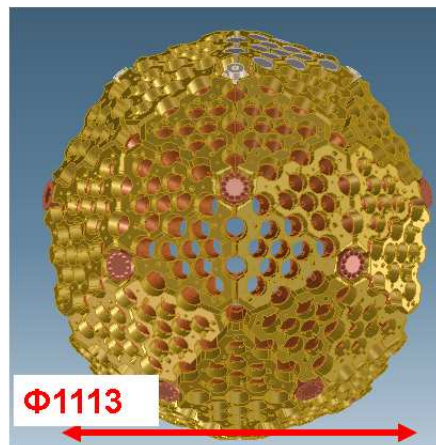


Figure 4.4: The basic structure of the PMT holder.

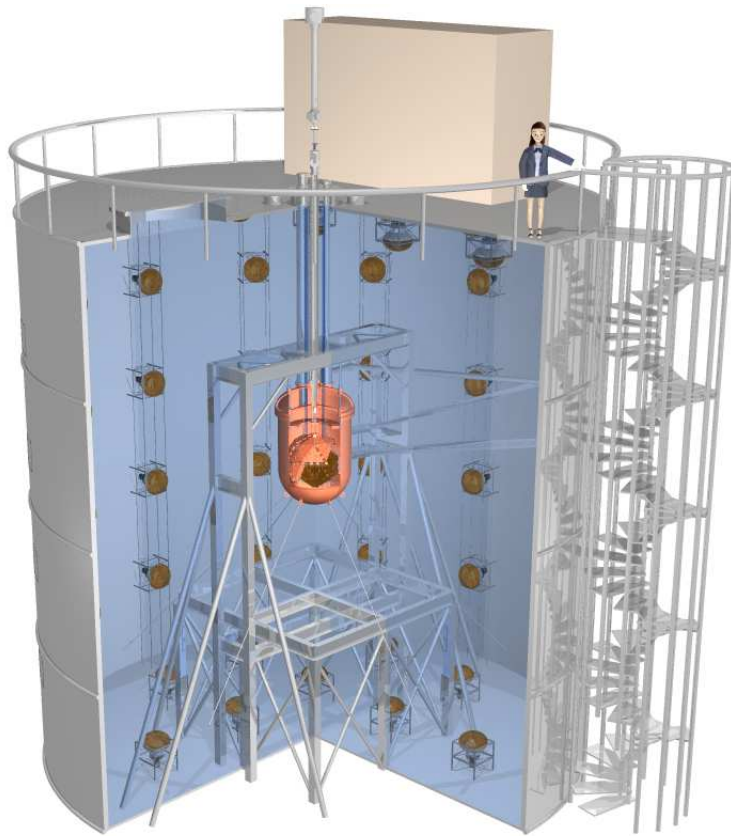


Figure 4.5: The XMASS water tank to veto environmental neutrons, gamma rays and cosmic rays.

4.2 Low background techniques

The estimated background from all PMTs is well less than 10^{-4} counts/day/keV/kg (dru) inside the 20 cm radius fiducial volume. 10^{-4} dru is the required background level for our goal of a spin independent cross section sensitivity of 10^{-45}cm^2 . To reach this sensitivity, various low background techniques were developed as described below.

4.2.1 Low background PMT

The main source of background in this experiment is gamma rays originating from the 642 PMTs in the IVC. The XMASS collaboration developed low radioactivity PMTs (R10789-11) with Hamamatsu Photonics. Fig.4.6 shows the picture of the R10789-11 which is 2 inch hexagonal shape. The opposite side distance is 5.8cm and the effective area of photocathode is a circle with radius 2.5 cm.

All materials used in the PMT and its base circuit were assayed in terms of the content of radioactive impurities using HPGe detectors in the Kamioka Mine. For each component of the PMT, possible products were searched and collected and radioactivity of them were measured. The lowest background product was selected among them.

Table 4.2 shows the measured radioactivity of the selected components. We achieved background reduction factor of a 100 larger than that with ordinary PMTs. The XENON10 collaboration also developed a low BG PMT (R8520-Al) [54]. Table 4.3 shows the comparison of the XMASS PMT with that from XENON10. The photocathod size of the XENON10 PMT is 1 inch square. The radioactivity of the XMASS PMT is lower than that of XENON10 after the correction of effective area except for Th.

In order to reduce heat from the PMT, the base current of the PMTs was reduced to $31.2 \mu\text{A}$ at 1750V. Fig.4.7 shows the circuit of the PMT(R10789-11). We took into account a loss of linearity at high signal rates due to a reduction of this base current. The most severe condition will occur when we take calibration data. We estimate a single PMT has at most 100p.e. signal with 1kHz. The base current guarantees the deviation from linearity is less than 2% which is satisfactory.

To cut the signal reflection caused by impedance mis-match at the inputs of ATM and FADC electronics boards, a 51Ω back termination (R18) was put on the circuit board.

Dark noise is an important issue with PMTs. If the dark noise rate caused by thermal electrons is high, the BG level increases due to accidental coincidences of dark noise hits. The relation between the accidental coincidence rate from dark noise and the number of PMTs in trigger is shown in Fig.4.8. The following equation is used to estimate of the trriger rate:

$$R_{coin} = N_{pmt} C_{N_f} \times N_f \times r^{N_f} \times T^{N_f-1} \quad (4.1)$$

where R_{coin} is the random coincidence rate, N_{pmt} is the number of PMTs (642), N_f is the number of PMTs in trigger (hit PMTs), r is the dark rate and T is the gate width, assumed to be 200nsec. The dark rate of all PMTs was measured at room temperature and at -100 degrees. Fig.4.9 shows the results of the measurements. At room temperature the dark rate was about 200Hz. But at

PMT	U (mBq/PMT)	Th (mBq/PMT)	K (mBq/PMT)	⁶⁰ Co (mBq/PMT)
dynode	-0.03(±0.08)	0.16(±0.09)	-1.02(±0.76)	0.11(±0.04)
electrode	0.10(±0.08)	0.08(±0.08)	-0.80(±0.49)	0.05(±0.03)
side tube upper	0.01(±0.11)	0.17(±0.13)	-1.38(±1.25)	0.98(±0.09)
side tube lower	0.03(±0.11)	0.16(±0.13)	-1.91(±1.18)	1.11(±0.08)
stem	0.02(±0.07)	0.08(±0.07)	0.25(±0.48)	0.81(±0.05)
glass in stem	0.20(±0.01)	0.19(±0.01)	1.35(±0.12)	0.008(±0.004)
lead wire	-0.07(±0.05)	0.09(±0.06)	-1.04(±0.47)	-0.02(±0.02)
window	-0.08(±0.07)	-0.01(±0.07)	0.51(±0.63)	-0.005(±0.03)
sealing parts	-0.03(±0.03)	0.02(±0.04)	-0.75(±0.43)	-0.04(±0.02)
insulator	-0.06(±0.05)	-0.01(±0.05)	0.40(±0.50)	-0.003(±0.002)
insulator2	-0.005(±0.005)	-0.001(±0.005)	0.04(±0.04)	-0.000(±0.002)
others	0.02(±0.02)	0.07(±0.03)	-1.77(±2.94)	-0.01(±0.01)
base	U (mBq/PMT)	Th (mBq/PMT)	K (mBq/PMT)	⁶⁰ Co (mBq/PMT)
resistor	0.03(±0.004)	0.03(±0.004)	0.34(±0.05)	0.000(±0.001)
capacitor dynode	0.004(±0.02)	0.01(±0.02)	0.17(±0.19)	0.004(±0.007)
capacitor coupling	0.22(±0.03)	0.09(±0.02)	-0.85(±0.11)	-0.08(±0.005)
circuit	0.07(±0.01)	0.01(±0.01)	-0.003(±0.10)	0.000(±0.004)
solder	0.007(±0.02)	0.04(±0.03)	0.02(±0.02)	-0.003(±0.007)
connection pin	0.007(±0.03)	0.03(±0.05)	-0.19(±0.45)	0.02(±0.02)
screw M2	0.01(±0.01)	0.05(±0.01)	-0.03(±0.14)	-0.001(±0.006)
HV connector	0.007(±0.004)	0.008(±0.004)	-0.04(±0.04)	-0.002(±0.001)
signal connector	0.006(±0.018)	0.08(±0.02)	-0.08(±0.14)	0.003(±0.007)
teflon holder	0.24(±0.14)	0.15(±0.16)	0.86(±1.26)	-0.007(±0.05)

Table 4.2: Radioactive impurities of parts in PMT and base measured by HPGe detector.

-100 degrees the dark rate was reduced to around 20Hz. The effect of the dark noise can be negligible if we require more than 10 hits which corresponds to 2-3keV_{ee} in our detector.

Fig.4.10 shows the distribution of the PMT gain. At -100 degrees the PMT gain increased by about 10 %. The reason for this increase has not been understood, so far. Fig.4.11 shows the quantum efficiency (QE) of the PMT. The average value of QE is 31 %.

	U (mBq/PMT)	Th (mBq/PMT)	K (mBq/PMT)	⁶⁰ Co (mBq/PMT)
XMASS	0.704(±0.282)	1.51(±0.31)	< 5.10	2.92(±1.61)
XENON10	0.32	0.23	8.6	1.7
	U (mBq/PMT/cm ²)	Th (mBq/PMT/cm ²)	K (mBq/PMT/cm ²)	⁶⁰ Co (mBq/PMT/cm ²)
XMASS	0.036(±0.014)	0.077(±0.016)	< 0.26	0.15(±0.08)
XENON10	0.066	0.048	1.78	0.35

Table 4.3: Radioactive impurities in PMT using XMASS and XENON10 [54]. The radioactivity of PMT using XMASS is lower than that of PMT using XENON10 after the correction of effective area except for Th.



Figure 4.6: Picture of PMT (R10789-11).

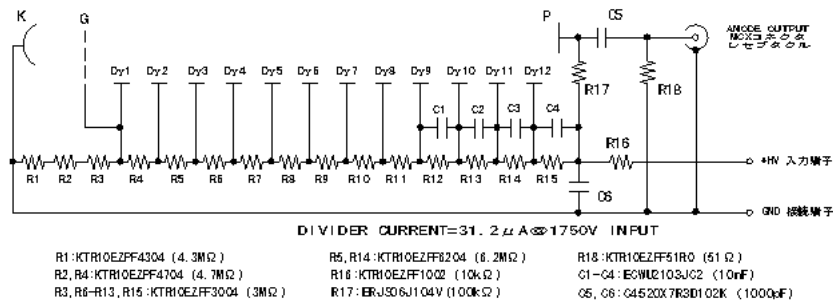


Figure 4.7: Circuit diagram of the PMT base.

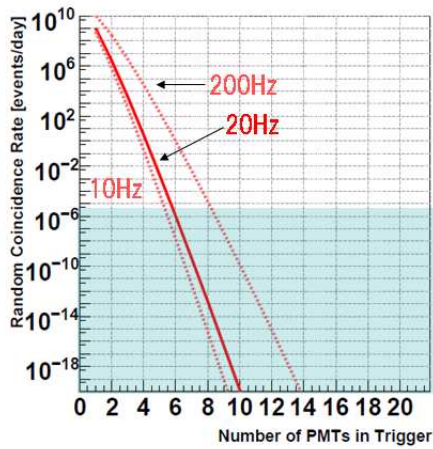


Figure 4.8: The relation between the accidental coincidence rate for dark noise and number of PMTs in a trigger. The horizontal axis shows the number of PMT hits making a hardware trigger. The horizontal axis corresponds approximately to the number of p.e. . The blue region shows the BG rate region below 0.01 % of all of the PMTs BG level assuming the 100kg fiducial volume and 10 keV energy window from 5 to 15keV and 200nsec gate width.

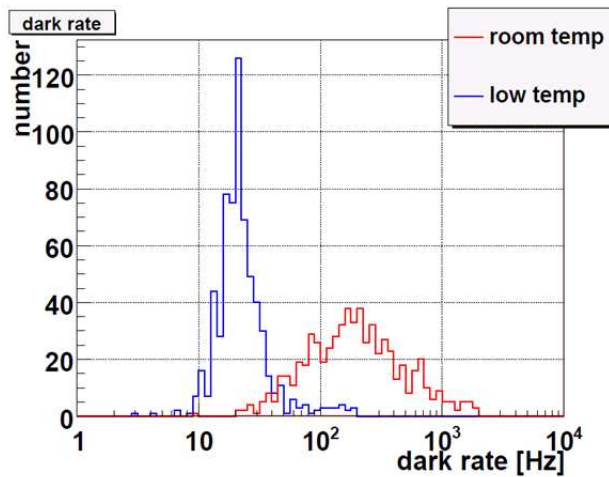


Figure 4.9: The dark rate distribution for the XMASS PMTs at -100 degrees (blue) and room temperature (red).

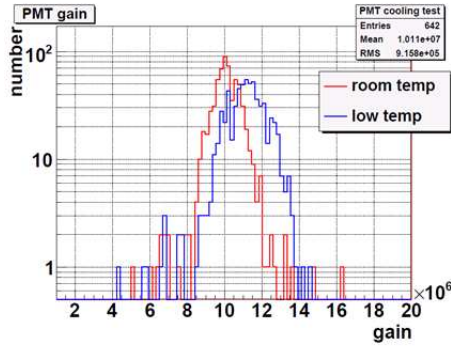


Figure 4.10: The gain distribution at -100 degrees (blue) and room temperature (red). The applied high voltage was corresponded to 10^7 gain at room temperature.

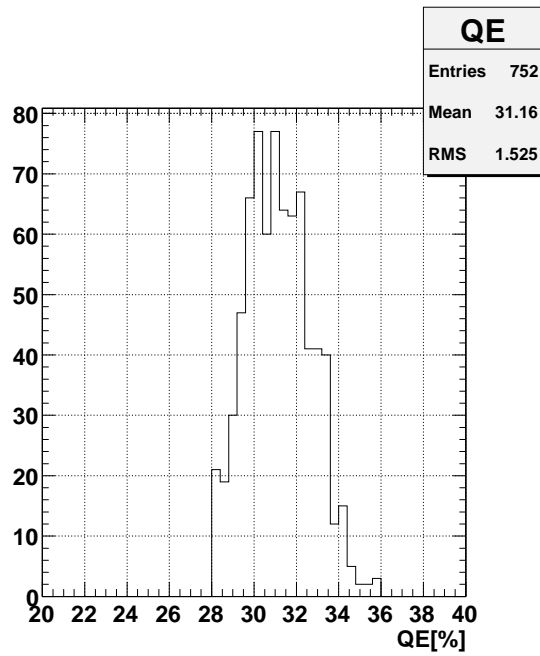


Figure 4.11: The QE distribution.

4.2.2 Material selection

All materials used in the detector structure (PMT holder, IVC, OVC and etc.) were screened by HPGe detectors. Fig.4.12 shows the measured radioactivity of each detector part in units of the total radioactivity of the 642 PMTs.

In order to compare the impact of radioactivities in each part of the detector, we employed Monte Carlo (MC) simulations to correct for the distance from liquid xenon. An exception is the PMT holder since the geometrical condition for the PMT holder is very similar to that of the PMTs, so we did not apply any correction. Other parts are evaluated using MC simulations. It is found that the total background originating from all the parts besides the PMTs is less than 35% compared with those from PMTs.

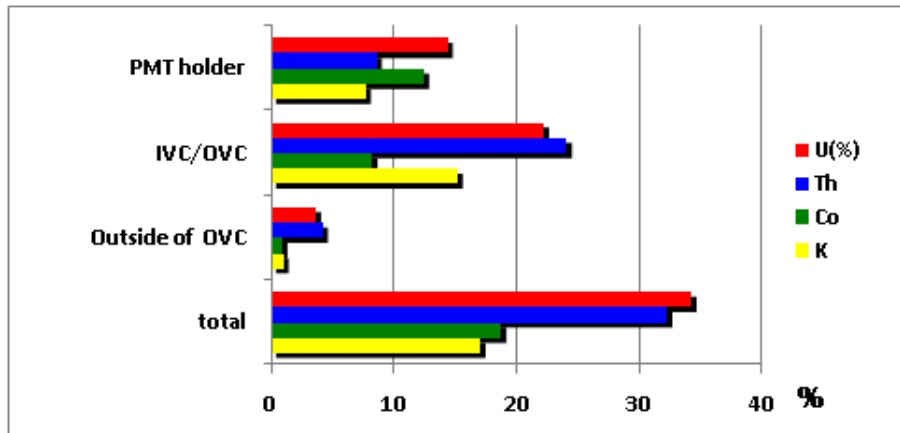


Figure 4.12: The radioactivity of the all materials comprising the XMASS detector. The value relative to the 642 PMTs radioactivity is shown. The value of IVC/OVC and outside of OVC include the dependence of the distance between liquid xenon and each of the materials.

4.2.3 Elution test

Liquid xenon is a highly solvent material. Therefore all detector elements must have been tested in liquid xenon, which we call elution test. Fig.4.13 shows the setup used for this purpose. 9kg liquid xenon was used in the elution test. Two PMTs were set in the chamber and the sample was set on the bottom flange. A ^{57}Co gamma ray source was set in the chamber to monitor the light variation caused by the elution material from each sample. The distance between PMT2 and ^{57}Co source was 100 mm. The light variation of PMT2 was measured.

As an example of the elution test, Fig.4.14 shows the light variation of the run for the base of the PMT bleeder circuit. After ultrasonic cleaning with isopropanol, the 6 bases were set on the bottom flange. Time $t = 0$ shows the time when the xenon filling is finished. Scintillation light was decreasing and after 500 minutes the 122 keV gamma ray peak was not observed as shown by red points in Fig.4.14 . It was found that the bases of PMTs elute something which absorb xenon scintillation light. Fig.4.15 shows the base and bottom flange after the base test. Soldering flux was seen on the base and flange.

Therefore, we tried another cleaning method which uses MK4 for pre-cleaning and isopropanol after the test of some combinations of cleaning product. It was found that this cleaning method was successful and no more absorption was observed by the detector as shown by black points in Fig.4.14. The light yield increased more than factor 2 compared to the method of only for isopropanol cleaning and remained stable at $-0.04\pm 0.11\%$ /day.

Table.4.4 shows the summary of the elution test for all elements which will be used in liquid xenon. The light yield was stable at about 0.1%/day considering the scale factor which is the conversion factor used to correct for the real amount of materials used in 1ton xenon.

list	light variation (%/day)	scale factor	estimated light variation(%/day/ton)
6 bases	-0.04 ± 0.11	1.0	-0.04 ± 0.11
Goretex	0.3 ± 3.7	12.5	0.02 ± 0.30
teflon tube after heat shrink	0.05 ± 0.01	30	0.0017 ± 0.0003
cable	-0.3 ± 0.5	2.2	-0.14 ± 0.23
fiber scope	1.7 ± 1.9	100	0.017 ± 0.019
magnetic fluid	-0.4 ± 0.75	47	-0.009 ± 0.016
LED+Krytox	-0.2 ± 0.8	200	-0.001 ± 0.004

Table 4.4: The result of elution test.

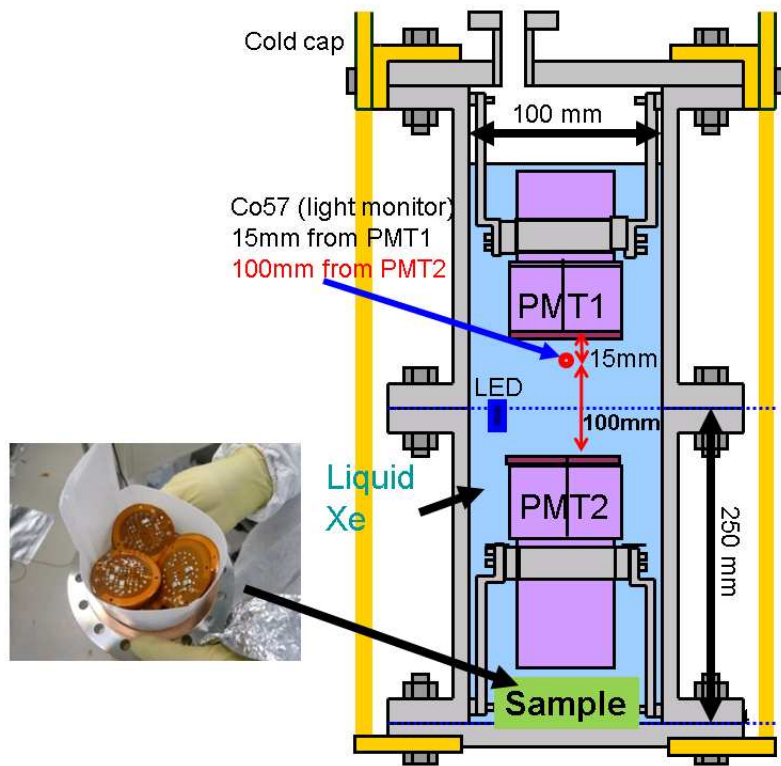


Figure 4.13: The setup for the elution test.

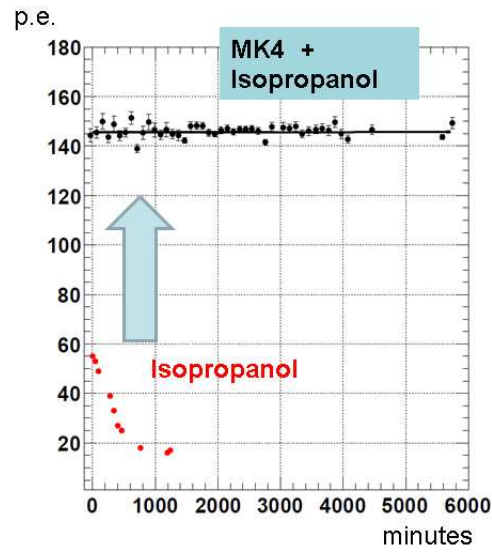


Figure 4.14: Time variation of light yield for a run with the PMT bases. The red and black points show the data for the sample after simple isopropanol cleaning and that after cleaning with MK4 and isopropanol.

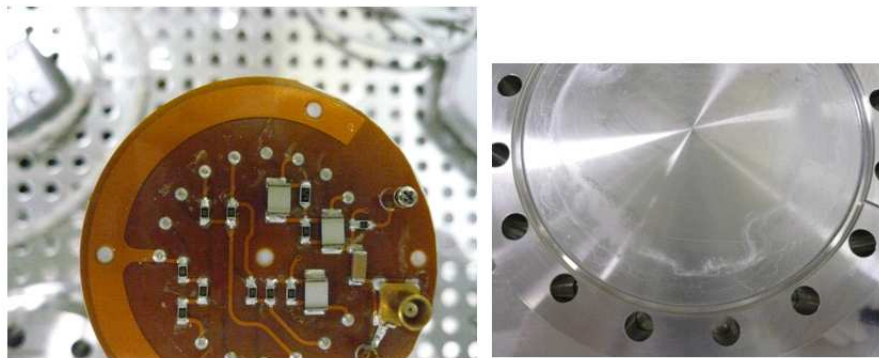


Figure 4.15: Picture of the base and bottom flange after the elution test. The base was cleaned using only isopropanol before the elution test.

4.2.4 Distillation

Typically xenon gas contains 0.1-3ppm krypton (mol/mol, also for all concentration numbers in this sub-section). Long-lived radioactive isotopes are not observed in xenon. However, krypton contains the radioactive isotope ^{85}Kr . The $^{85}\text{Kr}/\text{Kr}$ ratio is estimated to be 1.15×10^{-11} [55]. Fig.4.16 shows the expected event rate from the β decay of the ^{85}Kr for concentrations of 0.1ppm and 1ppt in xenon. To achieve less than 10^{-4} counts/day/kg/keV, krypton must be removed to a level below 1 ppt.

A distillation tower was constructed to remove krypton. The boiling point of xenon is 165 K. On the other hand, that of krypton is 120 K. Therefore, in principle the contaminated krypton in xenon can be removed by distillation. The schematic view of the distillation system developed by the XMASS collaboration [56] is shown in Fig.4.17.

There is a vessel called reboiler at the bottom of the distillation tower to evaporate liquid xenon. At top of the tower, there is a cooling refrigerator to liquefy xenon. Xenon circulates in the tower since the temperature is different between its top and bottom. At the top, xenon gas with higher concentrations of krypton is collected and this gas, called off-gas, is removed. On the other hand, at the bottom, liquid xenon with a very low contamination of krypton is collected. In our system design, 99 % of the xenon is collected as purified xenon and 1 % of the xenon is collected as off-gas. This ratio was determined to collect xenon efficiently.

We made a prototype distillation system in 2001 which was designed to reduce krypton by three orders of magnitude and a process speed of 0.6 kg/hour. We tested the performance of the distillation using the prototype, and based on its results the main distillation system was designed and developed in 2009. The design principle of the prototype system and results of the test are described in this section.

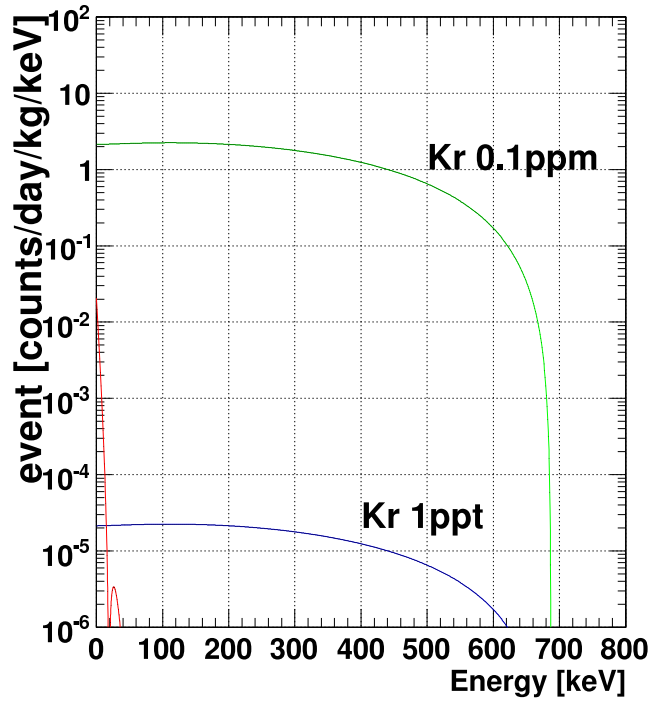


Figure 4.16: The background event rate from krypton. The green and blue lines show the BG rate for concentrations of 0.1 ppm and 1 ppt krypton contamination. The red line shows the event rate for 100 GeV dark matter with $\sigma_{\chi-p}^{SI}$ of 10^{-43}cm^2 . The $^{85}\text{Kr}/\text{Kr}$ ratio is 1.15×10^{-11} . L_{eff} is assumed to be 0.2.

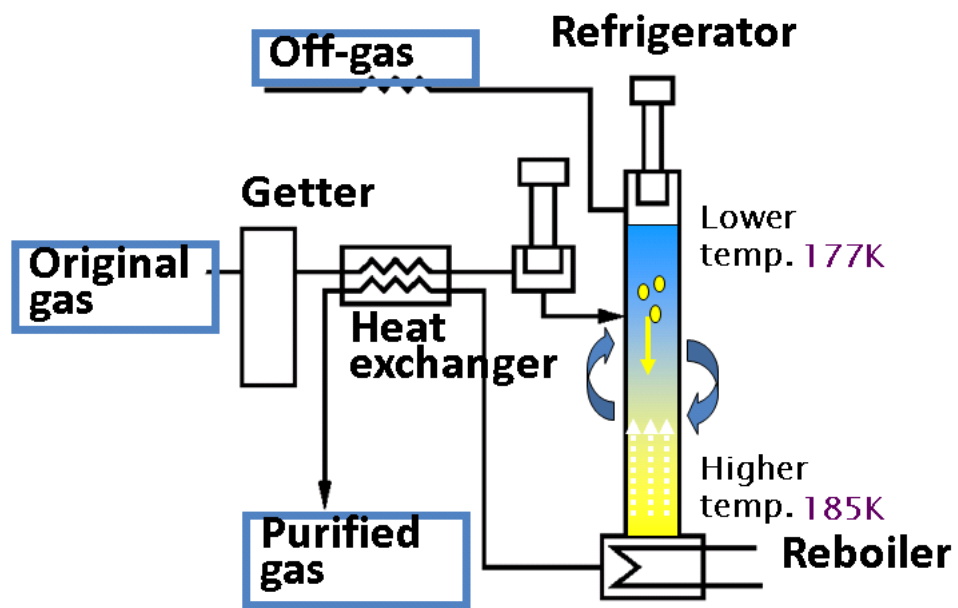


Figure 4.17: The schematic view of the distillation system.

Principle of distillation

The principle of distillation is described by the McCabe-Thiele (M-T) method [57] as shown in Fig.4.18.

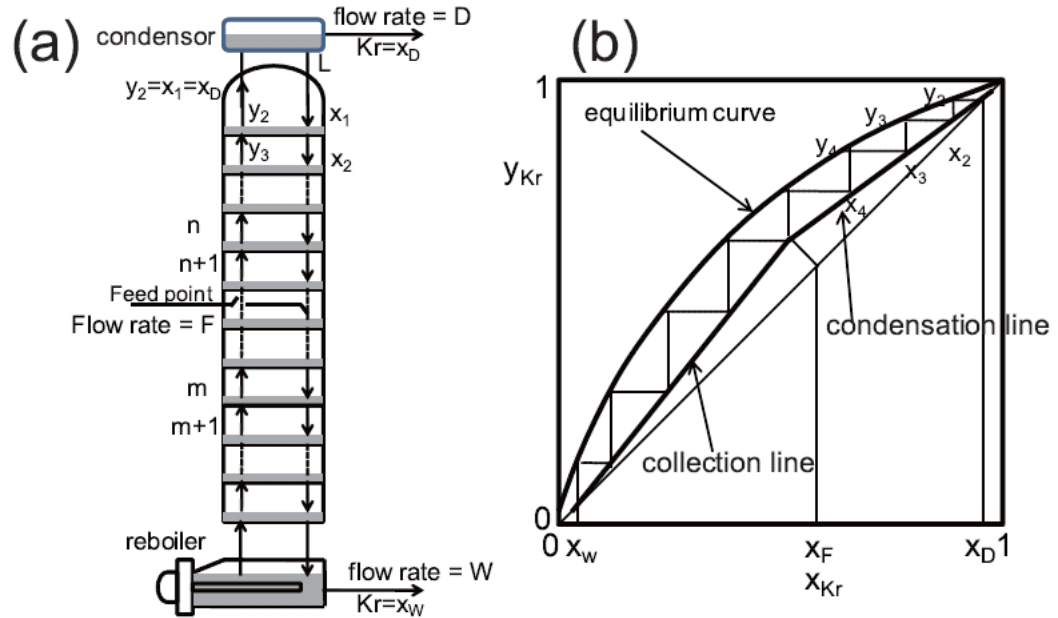


Figure 4.18: (a) The flow diagram for the McCabe-Thiele (M-T) method. (b) Calculation of the number of theoretical cells using the M-T method. The horizontal and vertical axes represent the krypton concentration in the liquid and gas phases, respectively. The thick solid curve is the equilibrium curve, and the thick solid lines are the condensation line and the collection line.

The main element in the distillation system is a tower in which a gas-liquid equilibrium is maintained. In the reboiler, liquid xenon is boiled using a heater. In order to keep the temperature around -100 degrees in the distillation tower, a refrigerator is set at the top. The original xenon gas is cooled down to near the boiling point by the heat exchanger and refrigerator, and then supplied to the feed point in the tower at flow rate (F) as shown in Fig.4.17 and Fig.4.18. The purified xenon is collected from the reboiler at flow rate (W), and xenon with a higher krypton concentration is collected from the top of the distillation tower at flow rate (D). The krypton concentration in the xenon at feed point, reboiler and top side is expressed as x_F , x_W and x_D , respectively. The flow of xenon in the tower (L) is controlled using the heating power at the reboiler and cooling power of refrigerator.

In the M-T method, the distillation tower consists of a connected series of the theoretical cells with the gas-liquid equilibrium changing by one step in each cell. The number of theoretical cells is calculated from the boundary conditions imposed by F , D , W , x_F , x_W , x_D and R , where $R = L/D$ is the reflux ratio.

In case of equilibrium between the liquid and gas phases in the mixture of krypton and xenon, the partial pressure of the gas phase (p_{Kr} and p_{Xe}) depends on the composition of each element in the liquid phase (x_{Kr} and x_{Xe}) by Raoult's law,

$$p_{Kr} = P_{Kr} \cdot x_{Kr} \quad (4.2)$$

$$p_{Xe} = P_{Xe} \cdot x_{Xe} \quad (4.3)$$

where P_{Kr} and P_{Xe} are the vapor pressures of pure krypton and pure xenon, respectively. At 178K, P_{Kr} and P_{Xe} are 2.09MPa and 0.201MPa, respectively. Using Raoult's law, the concentrations of krypton in the gas phase (y_{Kr}) is shown using the liquid phase (x_{Kr}),

$$y_{Kr} = \frac{\alpha \cdot x_{Kr}}{1 + (\alpha - 1)x_{Kr}} \quad (4.4)$$

where α is the ratio of vapor pressures of krypton and xenon, P_{Kr}/P_{Xe} (10.4 at 178 K). Eq. 4.4 is called the equilibrium curve, and it is shown by the thick solid curve in Fig. 4.18(b). For each theoretical cell, krypton concentrations in the neighboring cells are shown using the conservation of mass flow,

$$y_{n+1} = \frac{R}{R+1}x_n + \frac{1}{R+1}x_d \quad (4.5)$$

$$y_{m+1} = \frac{R'}{R'-1}x_m - \frac{1}{R'-1}x_W \quad (4.6)$$

Eq. 4.5 and Eq. 4.6 show the krypton concentration for the cells above and below the feeding point, respectively. n and m are the number of theoretical cells. R' is $(L + qF)/W$, where q is the fraction of liquid with respect to the total feed material. Eq. 4.5 and Eq. 4.6 represent the condensation line and the collection line, respectively; these are shown as solid lines in Fig. 4.18(b). Fig. 4.18(b) illustrates the method of estimating the number of required theoretical cells.

The prototype distillation system was designed to fulfill the following requirements:

- The krypton concentration of the purified xenon should be three orders of magnitude smaller than that of the original xenon, i.e. $x_W = \frac{1}{1000} \times x_F$.
- The collection efficiency of xenon should be 99%, i.e. $W/F = 0.99$ and $D/F = 0.01$.
- The system should have a process speed of 0.6 kg/hour, which allows 100 kg xenon to be purified within one week.
- The system should have reflux ratio $R = 191$, which means the required heating power at the reboiler is 14 W.
- Xenon should be fed into the system in the gas phase, i.e. $q = 0$.

A M-T diagram based on these requirements is shown in Fig. 4.19, in which the concentration of krypton in original xenon (x_F) was assumed to be 3×10^{-9} . 6 stages of theoretical cells are required from the M-T diagram as shown in Fig. 4.19. The total length of the prototype distillation tower is 208 cm and the diameter of the column is 2 cm.

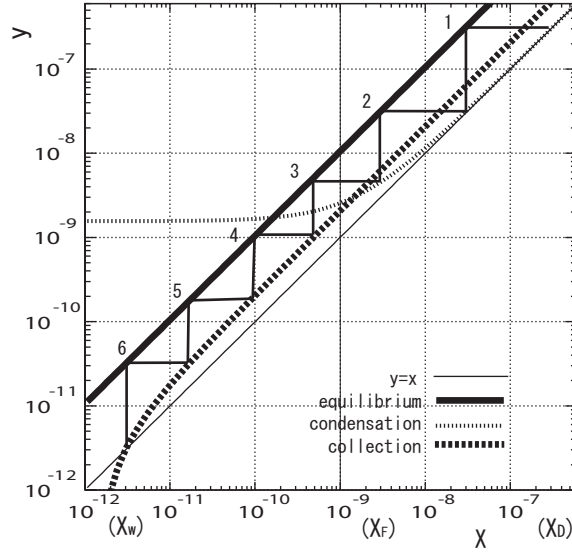


Figure 4.19: M-T diagram with system requirements.

Distillation test

As described above, the krypton removal efficiency depends on the reflux ratio R which is a function of the heating power at reboiler and process speed. A distillation test was performed to confirm the relationship between the the krypton removal efficiency and those operation parameters using a prototype distillation system whose krypton removal efficiency is designed to be 3 orders of magnitude with a processing speed of 0.6 kg/hour. The prototype distillation system was used for the 100kg XMASS prototype detector, and actually 100kg xenon was processed in 2004 [56]. The krypton concentration was reduced to 3 ppt from 3ppb in the process of the 100kg xenon.

The xenon used for the 1ton XMASS detector has 0.1 ppm of krypton while we required 1 ppt level for the experiment. The new system was needed to reduce krypton contamination more than 5 orders of magnitude. In addition the process speed was also required to be a factor 10 higher than prototype to process 1.2 ton xenon within ~ 10 days.

To develop the new distillation system, the precise measurement of krypton removal was tested using the prototype system for various operation parameters as shown in Table.4.5. In this test, xenon containing 60 ppm of krypton was used.

Run	process speed	heating power	evaporation
Run1	0.6kg/hr (1.7liter/min)	22W	2.4 liter/min
Run2	0.6kg/hr (1.7liter/min)	5.6W	0.6 liter/min
Run3	1.2kg/hr (3.4liter/min)	22W	2.4 liter/min
Run4	1.2kg/hr (3.4liter/min)	44W	4.8 liter/min
Run5	1.66kg/hr (4.8liter/min)	66W	7.2 liter/min

Table 4.5: The parameter list from the krypton removal tests. The heating power shows the heater power of the re-boiler and the evaporation shows the amount of evaporation at the re-boiler. The collection level shows the collection level of xenon in the re-boiler.

The dependence of the amount of evaporation was tested at Run1 and Run2. The process speed was increased by a factor of 2 at Run3 and Run4, and a factor of 2.8 at Run5. The purified xenon was sampled every hour for 3 hours for each run and the krypton contamination in the sample gas was measured.

The krypton concentration after the distillation was measured using column of gas chromatography and API-MS (atmospheric pressure ionization mass spectroscopy). Fig.4.20 shows the schematic view of the system of the krypton measurement. The column was used to separate krypton from xenon using the difference in diffusion time. The difference of transmission time through the column (called retention time) between krypton and xenon is about 2 minutes. Fig.4.21 shows the mechanism of API-MS. Pure argon gas was used as a carrier gas. At the first stage the sample gas is ionized by the Corona discharge, and then at the second stage the charge is transferred to the material (krypton) with lower ionization potential than carrier gas (argon) by the ion-molecule reaction. After that the ionized gas is measured with a mass spectrometer.

Table.4.6 shows the result of krypton measurements. In the case where the amount of evaporation is larger than the process speed, about 4 orders of

Run	1st (ppb)	2nd (ppb)	3rd (ppb)
Run1	11	7.0	6.5
Run2	4500	3100	3100
Run3	2600	2500	3000
Run4	< 3	13	< 3
Run5	< 3	< 3	< 3

Table 4.6: The result of the krypton measurements.

magnitude of krypton removal is achieved even though the process speed is three times larger than the designed value.

As a result of this test, the new system was developed with a relatively compact scale. Fig.4.22 shows the new distillation tower and a column put in the distillation tower. The height of the distillation tower is 4m in which series of columns are placed, and the diameter of the column is 4cm. Each column is made from thin SUS mesh, through which xenon reach gas-liquid equilibrium. The designed process speed is 6 kg/hour assuming the flow rate is proportional to the cross section of the column. This process speed corresponds to 7days' to process 1 ton of xenon.

The new distillation system was constructed from January to March in 2009. In order to check the performance of the new distillation system, a test was performed in 2009 using xenon gas containing 10ppm krypton. The process speed was 4.7kg/hour, which is about 80% of the design speed. This is because the pipe line for collecting the purified xenon was too narrow to flow with the designed flow rate. The krypton contamination of the purified xenon was less than 0.1 ppb. Thus, more than 5 orders of magnitude of krypton removal from xenon was achieved. Since the performance test was performed with the flow rate of 4.7kg/hour, we plan to process 1 ton of xenon at this speed. It would take about 9 days to process 1 ton of xenon.

We performed the test with a much higher krypton concentration than our real value of the 1 ton of xenon. It is because the high sensitivity krypton measurement system was not installed at Kamioka at that time. One uncertainty is whether the performance demonstrated at higher krypton concentration can be applied to low krypton concentrations or not. However, if the krypton reduction factor is not satisfactory at lower krypton concentrations, we plan to repeat the distillation process until we reach the 1 ppt krypton level. In order to evaluate such low levels of krypton, a high sensitivity API-MS system and a setup for condensing krypton in xenon has been installed. XENON100 collaboration bought the same prototype distillation system developed by XMASS. The new distillation system achieved the highest krypton removal with high process speed.

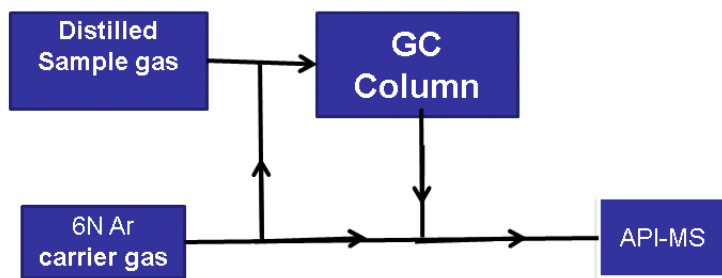


Figure 4.20: The setup of krypton measurement.

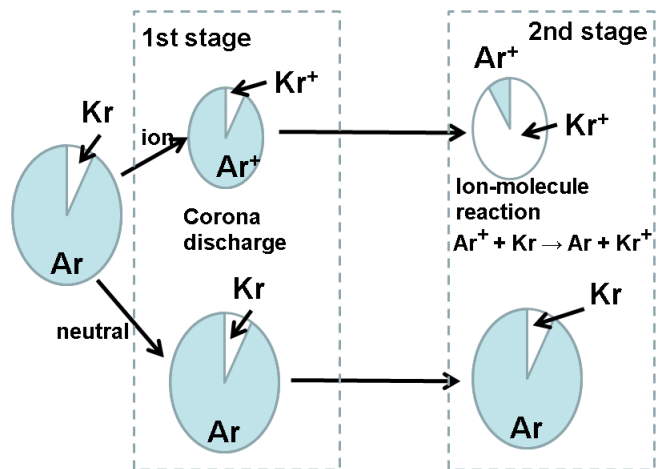


Figure 4.21: The mechanism of API-MS.



Figure 4.22: The picture of column and distillation tower whose krypton removal efficiency is 5 orders of magnitude and the processing capacity is 4.7 kg/hour.

4.2.5 Xenon circulation system

A xenon circulation system was constructed to remove impurities in the liquid xenon. Since the wavelength of the scintillation of liquid xenon is 175nm, the scintillation light is absorbed by oxygen, water and organic contaminants. In the case of oxygen and water, a getter and molecular sieves are known to be used to remove them. Impurities emanating from materials in liquid xenon have to be taken into account. Since we wish to avoid any unexpected but nonvolatile contamination due to the elution in the real detector, a special evaporation device will be employed in the circulation system. The device is expected to evaporate liquid xenon but keep the nonvolatile contamination inside.

Another internal BG is radon. Radon is a noble gas. Therefore Rn emanates from materials into the liquid xenon. Fig.4.23 shows the decay chain of ^{238}U . ^{222}Rn causes radioactive decays and some of these decays make ^{214}Pb . The half life of ^{214}Pb is very short at only 26.8 minutes, and causes β decay. Therefore ^{214}Pb is a BG for dark matter signals and the Rn has to be removed from xenon. To achieve BG level of 10^{-4} dru, the contaminated Rn has to be reduced to less than $7\mu\text{Bq}/\text{m}^3$ -xenon gas. Removal tests of Rn from liquid xenon using many types of charcoal are being studying now.

In order to estimate the decay rate of ^{222}Rn , the successive decay of Bi-Po chain is used. Fig.4.24 shows the decay scheme of Bi-Po chain. The two signals from β -decay with a Q-value of 3.27 MeV caused by the decay of ^{214}Bi and α with 7.69 MeV caused by the decay of ^{214}Po are measured in delayed coincidence.

4.2.6 The energy and vertex reconstruction

The XMASS experiment utilizes the self-shielding effect of liquid xenon to reduce BG as illustrated in Fig.4.25. Most of the gamma-rays are stopped at the edge of the detector and the low BG environment is achieved in the central region.

The vertex position is reconstructed using a pattern of p.e. from PMTs, and the energy is reconstructed using the number of p.e. after correcting for the vertex position. Currently, the reconstruction assumes a single vertex. The method of vertex and energy reconstruction was demonstrated using a prototype detector containing 100kg xenon [58]. The hit pattern of PMTs is made using detector MC. MC events are generated at 306 grid points in the detector (typically 6cm spacing), and the obtained hit pattern is used to reconstruct the vertex position as described below. The scattering length, absorption length and refractive index of xenon are assumed to be 41cm, 100cm and 1.61, respectively. Light yield is set at 42 photons/keV.

The hit patterns are defined as

$$F = F_i(r, \theta, \phi) \tag{4.7}$$

Here $F_i(r, \theta, \phi)$ is the expected number of p.e. of PMT No. i for a 1 p.e. signal which is generated at vertex (r, θ, ϕ) .

The vertex is reconstructed with the following likelihood for which the Poisson expectation is compared with the measured p.e. of each PMT with $F_i(r, \theta, \phi)$,

$$\log(L) = \sum_{i=1}^{642} \log \left(\frac{\exp^{-\mu_i} \mu_i^{n_i}}{n_i!} \right) \tag{4.8}$$

Here n_i is the number of p.e. detected by PMT No. i and μ_i is defined as

$$\mu_i = F_i(r, \theta, \phi) \times \text{“ number of generated p.e.”} \quad (4.9)$$

where “ number of generated p.e.” is calculated as

$$\text{“ number of generated photons”} = \frac{\sum_{i=1}^{642} n_i}{\sum_{i=1}^{642} F_i} \quad (4.10)$$

The vertex reconstruction consists of the following steps.

- Step 1: The rough position (P1) is calculated using the light weighted average of the hit PMT positions.
- Step 2: The likelihood is calculated around the point P1. The best grid point (G1) with maximum likelihood is selected using eq.4.8
- Step 3: 8 fine grid points are prepared around G1 and the map F is estimated for the 8 grids. The grid (G2) which gives the maximum likelihood is selected using the new map.
- Step 4: 20 grid points are prepared around G2 and the map F is estimated for 20 grid points. The grid point which gives the maximum likelihood is determined as the reconstructed position.

Fig.4.26 shows a typical event generated by MC. A Mollweide projection is used to map the spherical photoelectric surface into a 2D figure. The circles show the PMTs and color shows the number of photons detected by each PMT.

The light yield is estimated using MC. Fig.4.27 shows the position dependence of light yield. 12600 photons are generated at various position in the detector and then the total number of photoelectrons detected by all PMTs is counted. Because of the light attenuation in liquid xenon, the light yield of the central region is smaller than that of the outer region. Near the edge of the detector, the light yield decreases from the effect of light absorption by the copper wall. In the fiducial volume which is defined as the region within 20cm from the center, the light yield is 4.5 ± 0.1 p.e./keV .

After the vertex reconstruction, the reconstructed energy is calculated as

$$E [\text{keV}] = \frac{\text{“ number of generated p.e.”}}{N_{p.e.}(1\text{keV})} \quad (4.11)$$

Here $N_{p.e.}(1\text{keV})$ is the number of p.e. for 1 keV of energy deposit after the correction of the vertex position is applied.

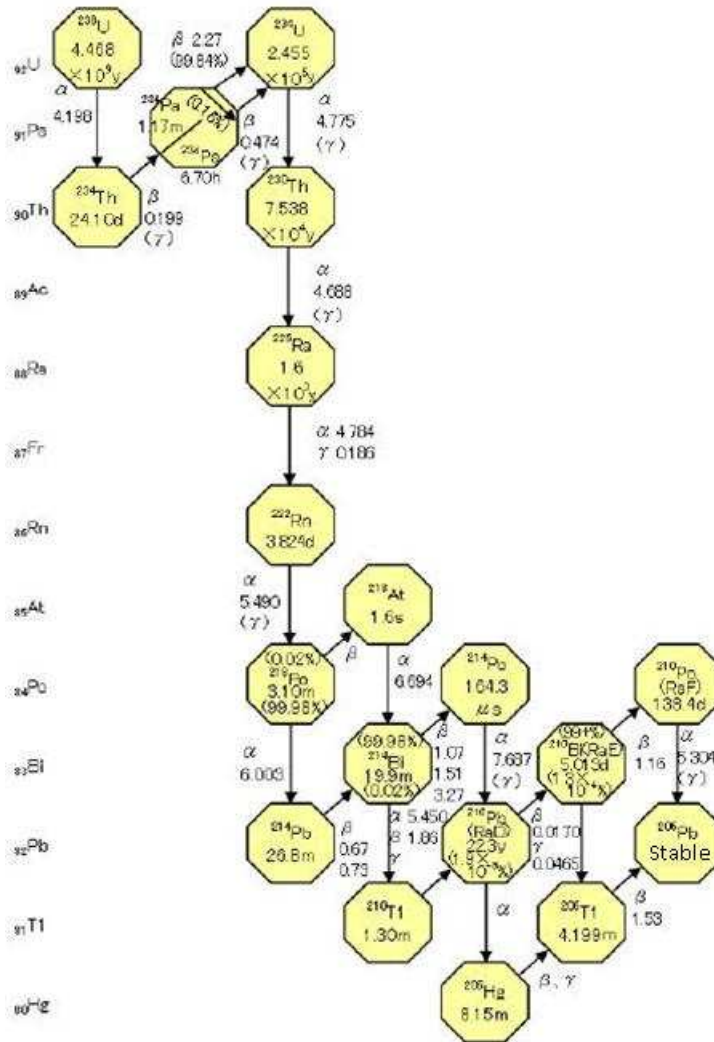


Figure 4.23: The Uranium 238 decay chain.

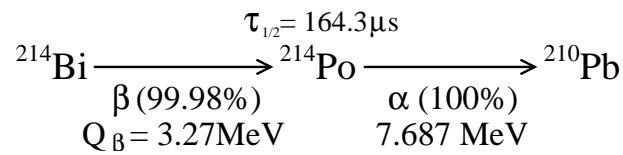


Figure 4.24: The decay scheme of Bi-Po decay.

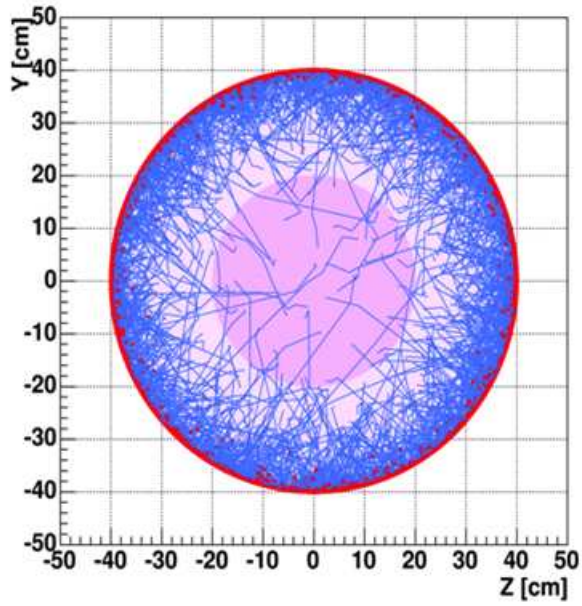


Figure 4.25: The schematic illustration of the self-shielding of liquid xenon. The dark pink region shows the fiducial volume. The blue lines show the tracks of gamma rays.

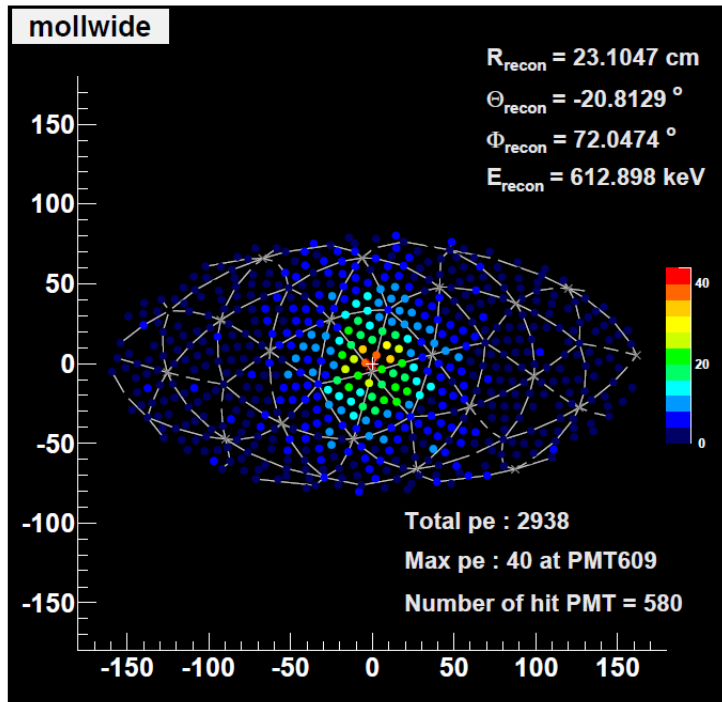


Figure 4.26: A typical event generated by MC. The circles show the PMT position. The color shows the number of photons detected by a PMT.

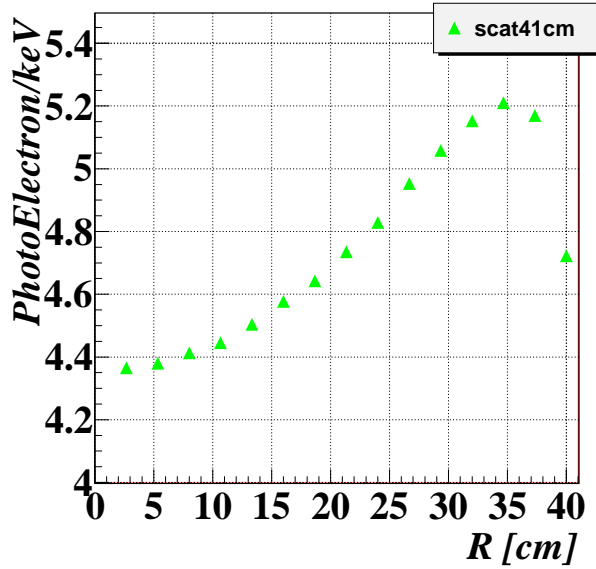


Figure 4.27: The relation between light yield and vertex position. Horizontal axis is the distance from the center of the detector.

- Position resolution

The position resolution is estimated using the detector MC for several energy ranges. Scintillation light is generated in the liquid xenon caused by the energy deposition of a point source. The distribution of distances between the generated positions and reconstructed positions is evaluated. The position resolution is estimated using the σ_{posi} of a Gaussian distribution. The Fig.4.28 shows the σ_{posi} distribution for several energy ranges. In the fiducial volume, the σ_{posi} is 3cm in the range of 5-25keV.

- Energy resolution

The energy resolution is also estimated using the detector MC. The distribution of the difference between true energy deposited and reconstructed energy is evaluated. Then the energy resolution is estimated using the σ_{ene} of a Gaussian distribution. Fig.4.29 shows the σ_{ene} distribution for several energy ranges. The energy resolution is uniform through out the detector. In the 5-25keV range σ_{ene} is 2keV.

4.2.7 BG MC

The main BG source in the XMASS detector is gamma-rays from the 642 PMTs. As mentioned in section 4.2.1, the total activity level of U, Th and ^{60}Co from all 642 PMTs is 0.45 Bq, 0.97 Bq and 1.9 Bq, respectively. All other materials were measured using HPGe. As a result of the measurements, it is found that the total BG caused by materials besides the PMTs is less than 35% than that of the PMTs. The energy spectrum of the background of them is similar to

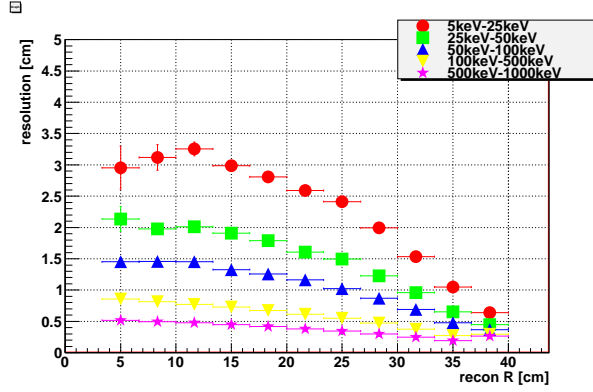


Figure 4.28: The position resolution. The horizontal axis shows the radius of reconstructed position and vertical axis shows the σ_{posi} .

that of the 642 PMTs. So, the total background can be estimated by simply increasing the PMT background, which will be described below, by a factor of at most 1.35 .

The detector simulation program was developed based on GEANT4 [59] package. Table.4.7 shows the list of simulation parameters.

Parameter	Value
light yield of liquid xenon	42 photons/keV
Absorption length of liquid xenon	100cm
Scattering length of liquid xenon	41 cm
Refractive index of liquid xenon	1.64
Reflectance on inner wall	10%
Complex refractive index of photoelectric surface	$1.5+0.5i$
Quantum efficiency of PMT	30%
Collection efficiency of PMT	100%

Table 4.7: List of simulation parameters.

Fig.4.30 shows the BG spectrum caused by the radioactivity in the PMTs using a BG MC simulation with 1 year equivalent statistics. The BG rate is estimated $2.5 \times 10^{-4} dru$ below 20 keV_{ee} .

Below 200 keV the spectrum increases even though a fiducial volume cut is applied. This signature is caused by miss reconstructed events near the wall called "wall effect". It does not happen if the true vertex position for the event selection is used since low energy gamma-rays are attenuated due to absorption at the edge of the detector.

Even though the photocoverage is 63.4 %, the remaining surface is copper, whose reflectance is $\sim 10\%$. Therefore the scintillation light of events which occur near the wall of the detector is almost absorbed by copper. The scintillation light which is emitted in the direction opposite to the wall and spreads in various directions. The detected photon pattern looks like an event occurring

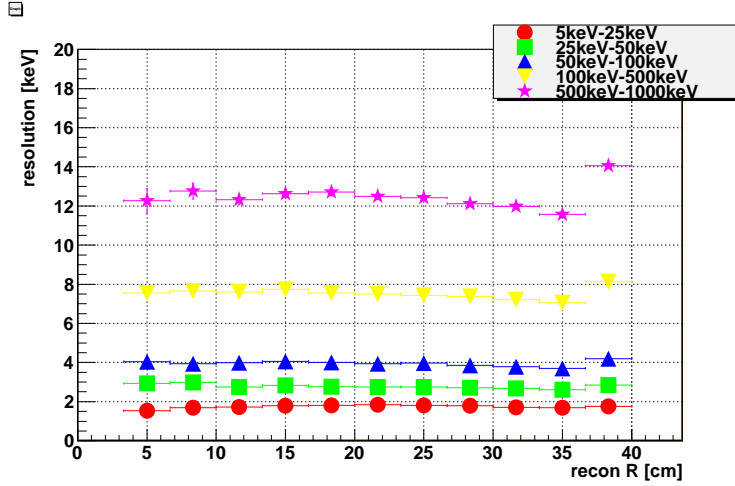


Figure 4.29: The energy resolution. The horizontal axis shows the radius of reconstructed position and vertical axis shows the σ_{ene} .

around the center. Since some events from near the wall are reconstructed as if events occurring around the center, the BG spectrum rises up below 200keV even after applying the fiducial volume cut.

The main motivation of this thesis is to reduce this "wall effect" using pulse shape analysis. The detailed discussion is described in chapter 6.

Environmental gamma rays from the rock are also estimated. The water tank is used to reduce environmental gamma rays. The gamma ray flux at energies higher than 500keV is $0.7 /cm^2/sec$. To reduce the BG level to less than the PMT level, at least 200cm is needed. The radius of the water tank is 2.5m and copper is used for IVC/OVC, PMT holder and filler. Therefore the BG from environmental gamma ray is reduced to less than that of the PMT BG.

4.2.8 Neutron background

Neutrons are an irreducible BG for dark matter searches. Single nuclear recoils by a fast neutron cannot be discriminated from dark matter signals. The neutron BG is categorized into two types, one is neutrons produced outside the water tank, and the other is neutrons produced by (α, n) reactions from radioactivity in the detector materials.

In the case of environmental neutrons, the water tank is used to reduce neutron BG. Fig.4.31 shows the reduction of environmental neutrons in the water tank using MC in which 10 MeV neutrons are generated on the outer surface of the water tank. None of the neutrons, out of 10^7 generated neutrons, reach the liquid xenon. Assuming all the neutrons in the Kamioka mine $(1.15 \pm 0.12) \times 10^{-5}/cm^2/sec$ have 10MeV kinetic energy this can be translated to an upper limit of the rate of neutrons entering the detector. The result is 2×10^{-2} counts/day which is not negligible but is limited by MC statistics. Further study with more statistics will be done.

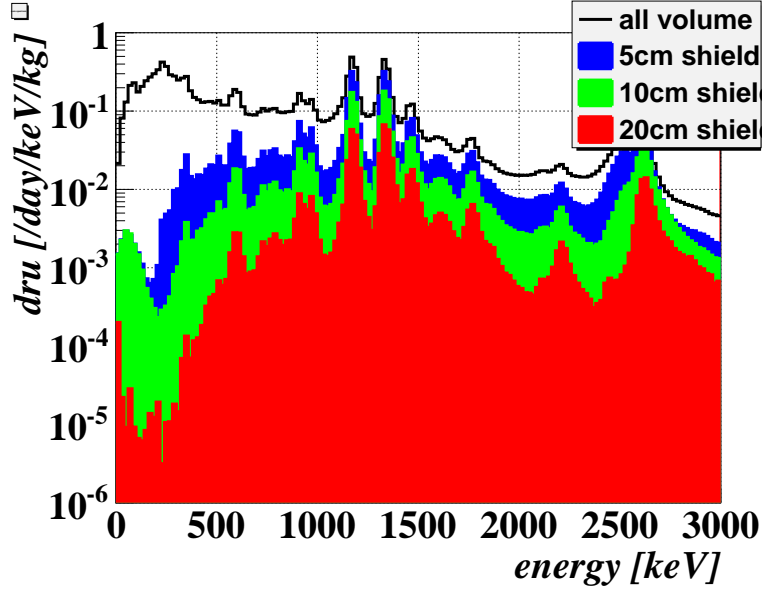


Figure 4.30: The expected BG spectrum caused by the radioactivity in 642 PMTs integrated over 1 year. Black, blue, green, red show 0cm, 5cm, 10cm and 20cm shielding.

The neutrons caused by (α, n) reactions are estimated using SOURCES [60]. Fig.4.32 and Fig.4.33 show the energy spectrum of neutron caused by (α, n) using the U/Th contamination of PMTs. The energy spectrum is shown in Fig.4.34. The BG level is less than 2×10^{-5} dru.

4.2.9 Expected sensitivity

The expected sensitivity of the XMASS experiment is shown in Fig.4.35 assuming $L_{eff} = 0.2$ and 2.5×10^{-4} dru BG level. Around a WIMP mass of 100GeV the sensitivity reaches $2.9 \times 10^{-44} \text{cm}^2$. In the chapter 6, the 90 % C.L. exclusion limit is discussed more detail. The sensitivity of the XMASS experiment is further improved using PSD which is the main topic of this thesis.

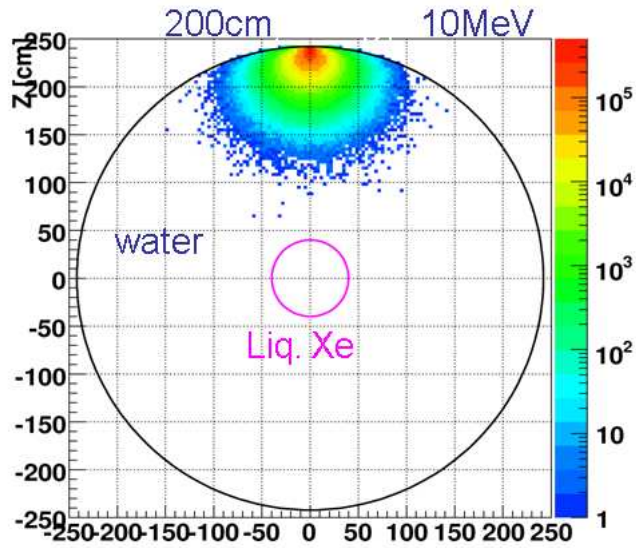


Figure 4.31: The attenuation of neutrons using MC. No events out of 10^7 generated neutrons reach the liquid xenon.

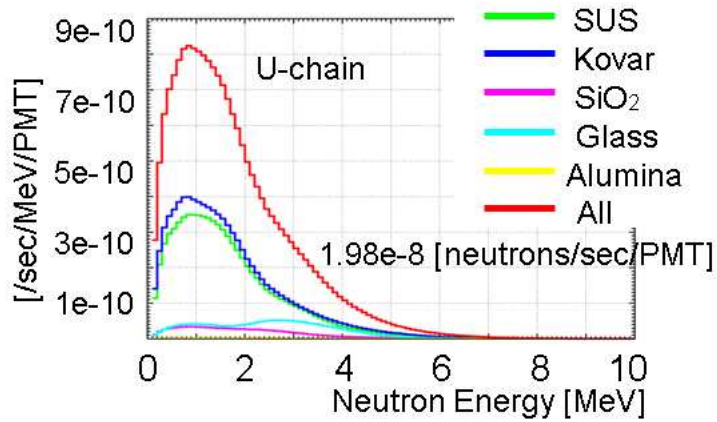


Figure 4.32: The energy spectrum of neutrons caused by (α, n) of U chain. The reactions with various materials used in PMT are estimated.

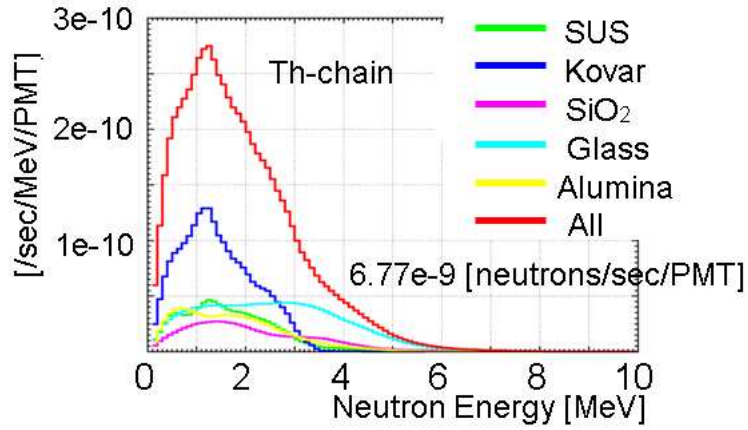


Figure 4.33: The energy spectrum of neutrons caused by (α, n) of Th chain.

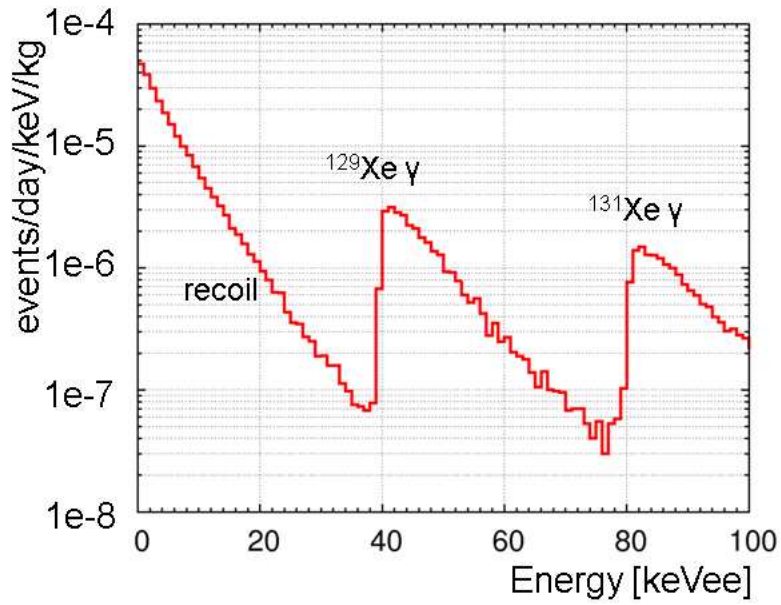


Figure 4.34: The BG level of neutrons caused by (α, n) reactions. The horizontal axis shows the visible energy assuming $L_{eff} = 0.2$. Inelastic events are seen at 40keV_{ee} and 80keV_{ee} .

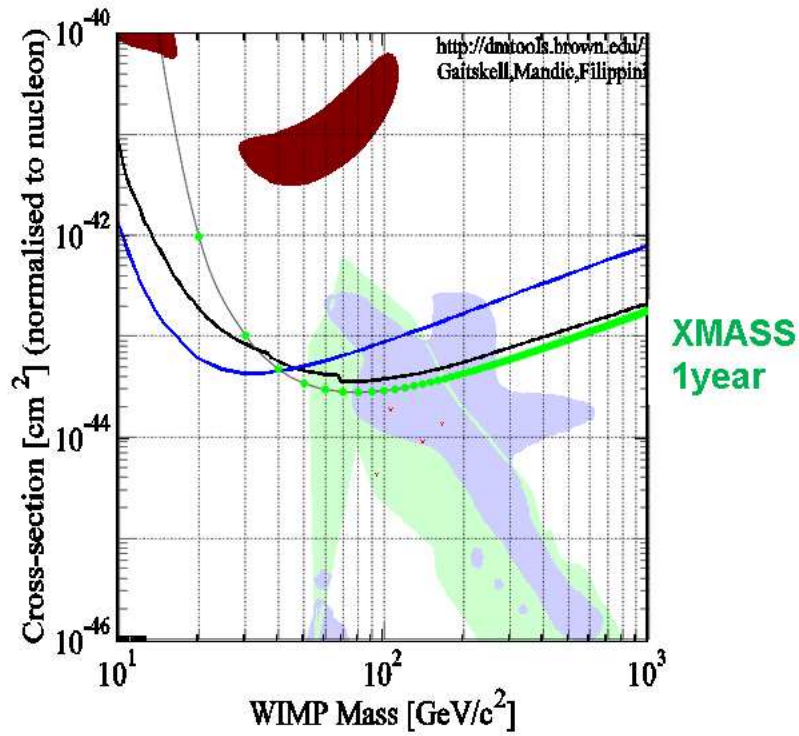
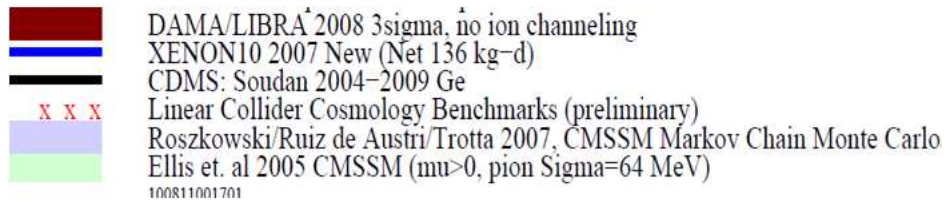


Figure 4.35: The 90 % C.L. exclusion limit of the XMASS experiment assuming $L_{eff} = 0.2$, $2.5 \times 10^{-4} dru$ BG level.

4.3 Detector design and concept for $0\nu 2\beta$ search

One of the main physics goals of the XMASS experiment is the high sensitivity search for $0\nu 2\beta$. In this section the detector design for the $0\nu 2\beta$ search is described. At low energy, the self shielding effect of liquid xenon is useful to reduce BG as described in previous section. However, in the case of $0\nu 2\beta$ search in ^{136}Xe , the self shielding effect does not work well at around the Q-value of ^{136}Xe (2.48MeV) even with a 10 ton fiducial volume detector as shown in Fig.4.36. To reduce BG around the Q-value, a different detector design is required.

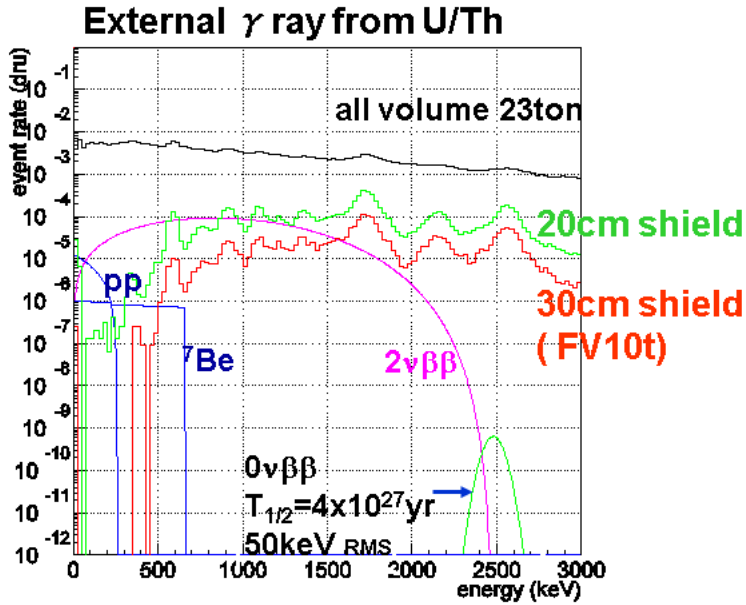


Figure 4.36: The expected BG spectrum using 23 ton liquid xenon. The black, green and red lines show the BG spectrum of all volume, with 20cm shield and 30cm shield. To reach the sensitivity of half life at 4×10^{27} year, a lower BG level is required by more than 4 orders of magnitude. $2\nu 2\beta$ is shown by a pink line assuming a half life of 8×10^{21} years. Solar neutrinos such as pp and ^7Be are shown as the dark blue and blue lines.

The conceptual design of the detector is shown in Fig.4.37. The detector consists of an elliptic tank (ELT) filled with water, an acrylic vessel filled with ^{136}Xe and a few photosensors. The acrylic vessel is put at one focus and photosensors are put at the other focus. Since the scintillation light of liquid xenon is vacuum ultra violet (VUV), the scintillation light is absorbed by the acrylic vessel and water. Therefore the wavelength shifter is set on the inner surface of the acrylic vessel. To collect the scintillation light with high efficiency, the inner surface of the ELT is mirror. Because of the convergence of photons to a relatively small focus point, the number of photosensors can be reduced drastically.

Usually, one of the most serious BG sources in low background experiments is radioactivity in the photosensors. The large reduction in the number of photosensors helps a lot in reducing the BG. Furthermore, because the gamma rays from the photosensors are attenuated by pure water in the ELT, it is possible to reduce the BG further.

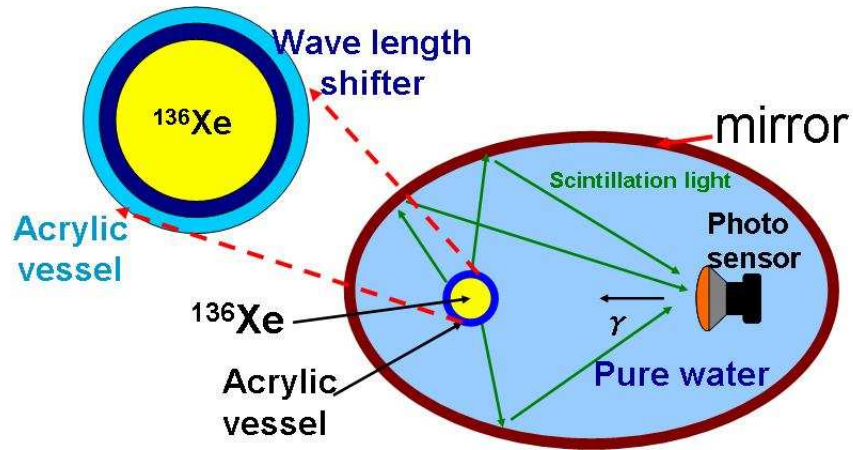


Figure 4.37: Conceptual design of a double beta decay experiment. The ELT detector consists of photosensors and enriched liquid xenon. Since the inner surface of ELT is mirrored, the scintillation light from the ^{136}Xe is detected with high efficiency. Furthermore, the photosensors which are the main BG source are kept away from ^{136}Xe .

4.4 Scintillation yield at room temperature

Usually liquid xenon is operated at around -100 degrees. However, in the ELT liquid xenon is used at room temperature. The light yield of liquid xenon at room temperature has not been reported so far. Therefore, we measured it with a dedicated setup for this pressure. The result of this measurement of the light yield at room temperature was published [61].

4.4.1 Experimental setup

Fig. 4.38 shows a schematic view of the high pressure vessel. The vertical cylindrical hole (16 mm diameter, 45 mm length) and the horizontal cylindrical hole (10mm diameter, 70 mm length) are completely filled with liquid xenon; the volume is 15 cc. The pressure of liquid xenon at room temperature is about 5 MPa. Therefore, the window where the scintillation light passes is made from MgF_2 with a thickness of 10 mm. In order to transmit scintillation light to a PMT, a light guide made from MgF_2 is placed between the MgF_2 window and the PMT. The light guide is needed because oxygen in air easily absorbs the VUV. A 2 inch PMT (R8778 Hamamatsu), which is sensitive to VUV, is used in this measurement. The gain of the PMT is set to 6.0×10^6 with an applied high voltage of +1544V. The quantum efficiency (Q.E.) of the PMT is 28% at room temperature for 175 nm. The gain and Q.E. vary with temperature. Therefore the temperature dependence of the Q.E. and gain were measured independently. As a results, Q.E. \times gain increased 15 ± 5 % from 1 degree to -100 degrees. The temperature dependence of the gain and Q.E. are taken into account in the following measurements. In order to collect scintillation light efficiently, Dupont Krytox 16350 is used as an optical grease on both sides of the light guide. The transmittance of the Krytox at 175 nm was more than 90% with a thickness of 25 μm . The refractive index of Krytox is estimated to be 1.35 at 175 nm [51].

Setup for the reference measurement

The light yield at room temperature was compared with that at reference temperature (T=-100 degrees, P=0.18 MPa). The light yield at around (T=-100 degrees, P=0.18 MPa) is summarized in [62]. Fig. 4.39 shows the setup for the reference measurement. The liquid xenon vessel, together with the 75 cc bottle and the PMT, are placed in a vacuum chamber. There is a container of liquid nitrogen on the vacuum chamber and it is connected to a cooling rod and cooling plate made from copper in the vacuum chamber. The liquid xenon vessel is cooled down by the cooling plate. The temperature was controlled using a heater wrapped around the cooling rod. The temperature of the liquid xenon vessel is kept at -100 ± 2 degrees. In order to control the pressure in the vessel, a 300 cc bottle is connected as shown in Fig.4.39.

4.4.2 Measurement

The scintillation light of liquid xenon was measured using the 122 keV gamma rays emitted from a ^{57}Co source with 7.4 kBq. The ^{57}Co source was put at the edge of the light guide as shown in Fig.4.38. In liquid xenon, 122 keV gamma

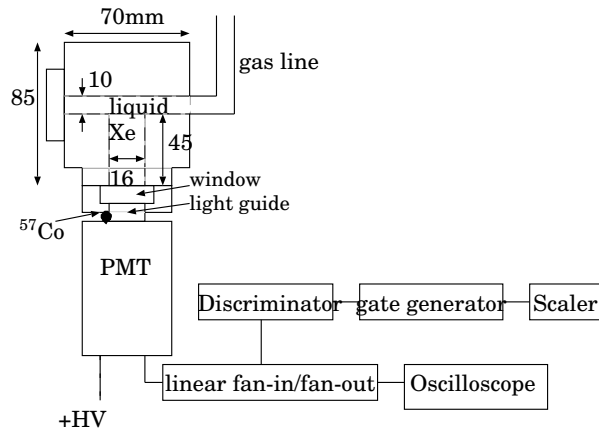


Figure 4.38: The schematic view of the liquid xenon vessel and measurement diagram; the inner volume of the high pressure vessel is 15 cc. The ^{57}Co source is located at edge of light guide.

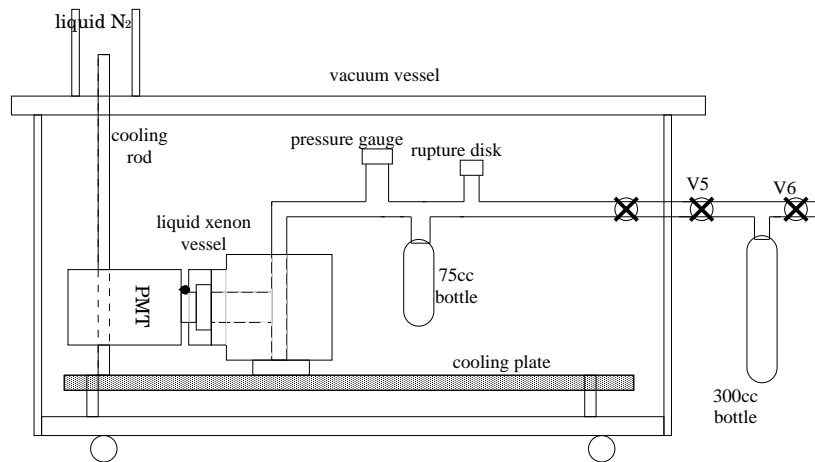


Figure 4.39: Setup for the reference measurement. The liquid xenon vessel is put in a vacuum chamber and is cooled down using liquid nitrogen. The 300 cc bottle is used to drain xenon gas from the liquid xenon vessel.

rays are attenuated within 2 mm. Hence, the scintillation light was emitted near the window. Data were taken using an oscilloscope (TDS 3064B). The trigger threshold was set to -16 mV (3 photoelectron level) and the waveform was recorded with a 500 MHz sampling rate.

First, the scintillation light at room temperature was measured. Since the critical point of xenon is 17 degrees [63], the temperature of the liquid xenon was kept at 1 ± 2 degrees which was well below the critical point. The pressure of the liquid xenon was 5.5 MPa. The event rate with the ^{57}Co source was 80 Hz.

Secondly, the scintillation light at -100 degrees was measured. The liquid xenon vessel was placed on the cooling plate in the vacuum chamber. Using liquid nitrogen and the cooling plate, the liquid xenon vessel was cooled down from room temperature to -100 degrees.

Since the liquid xenon vessel was connected to the 75 cc bottle whose temperature was still room temperature, the pressure of liquid xenon was still high around 4.5 MPa even at -100 degrees. In order to compare the scintillation yield at (T=-100 degrees, P=0.18 MPa) with the scintillation yield at (T=1 degree, P=5.5 MPa), the pressure of liquid xenon had to be reduced from 4.5 MPa to 0.18 MPa at -100 degrees. Xenon gas was drained from the liquid xenon vessel to the 300 cc bottle as shown in Fig.4.39. When the pressure in the 300 cc bottle was about 0.4 MPa, xenon gas was drained from the 300 cc bottle to atmosphere by opening V6 (V5 was closed before hand). After draining, the 300 cc bottle was evacuated. We continued to drain xenon gas from the liquid xenon vessel to atmosphere until the pressure in the liquid xenon vessel was reduced to 0.18 MPa at -100 degrees. Even during draining, the temperature of the liquid xenon vessel was kept to be -100 ± 2 degrees. Scintillation light yield was measured at each step of draining xenon, thus pressure dependence was measured. Finally, the scintillation light at (T=-100 degrees, P=0.18 MPa) was measured. The event rate at this temperature was 61 Hz. Since the PMT dark rate decreases at low temperature, the event rate also decreases.

4.4.3 Comparison of the light yield

The black line in Fig.4.40 shows the p.e. distribution of liquid xenon at (T=1 degree, P=5.5 MPa). The mean value from the Gaussian fit is 33.8 ± 0.6 p.e. On the other hand, the black line in Fig.4.41 shows the p.e. distribution of liquid xenon at (T=-100 degrees, P=0.18 MPa). The mean value for this case is 41.7 ± 0.6 p.e.

Fig. 4.42 shows the pressure dependence from 4.5 MPa to 0.18 MPa at -100 degrees. The number of p.e. is stable to within 4%.

In order to obtain the relative scintillation light yield between -100 degrees and 1 degree, the difference in refractive index between those temperatures must be taken into account. This is because the acceptance of the PMT depends on the refractive index of liquid xenon. The density (ρ , g/cm^3) at (T=-100 degrees, P=0.18 MPa) and (T=1 degree, P=5.5 MPa) is $2.88 \text{ g}/\text{cm}^3$ and $1.88 \text{ g}/\text{cm}^3$ [63], respectively. Generally, the refractive index changes if the material density changes. The following equation shows the refractive index as a function of

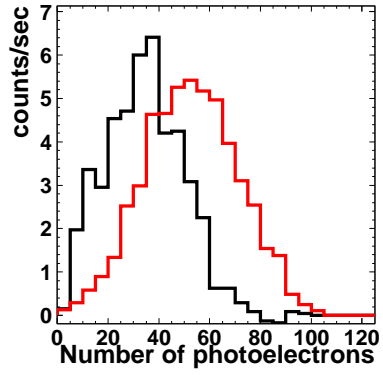


Figure 4.40: The p.e. distribution at (T=1 degree, P=5.5 MPa). The black line shows the data. The red line shows the MC.

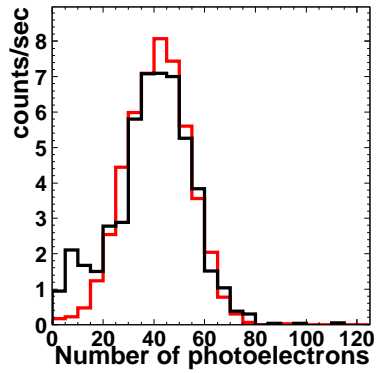


Figure 4.41: The p.e. distribution at (T=-100 degrees, P=0.18 MPa). The black line shows the data. The red line shows the MC.

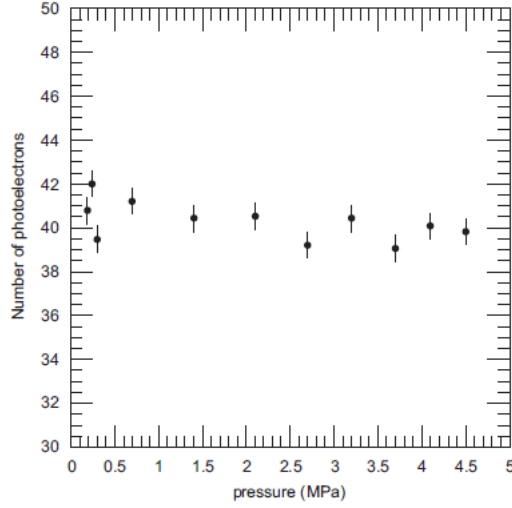


Figure 4.42: pressure dependence of the pulse height measured at $T = -100$ degrees. It is stable to within 4%. The errors are statistical only.

density [64]:

$$n = \sqrt{\frac{(1 + 2x)n_0^2 + (2 - 2x)}{(1 - x)n_0^2 + (2 + x)}} \quad (4.12)$$

where n_0 ($=1.62$) is the refractive index at ($T=-100$ degrees, $P=0.18$ MPa) and x is the density ratio, which is $\rho(1 \text{ degree}, 5.5 \text{ MPa}) / \rho(-100 \text{ degrees}, 0.18 \text{ MPa})$. In this case x is 0.65. From this equation the refractive index at ($T=1$ degree, $P=5.5$ MPa) is estimated to be 1.37. Because the refractive index of the MgF_2 window is 1.44 [65], the acceptance of the PMT increases as the refractive index of the liquid xenon becomes smaller. Hence, the acceptance for ($T=1$ degree, $P=5.5$ MPa) is larger than that for ($T=-100$ degrees, $P=0.18$ MPa). In order to estimate the difference of the acceptance, a simulation based on the GEANT4 package [59] was used. Table.4.8 shows the list of simulation parameters.

light yield at ($T=-100$ degrees, $P=0.18$ MPa)	42 photons/keV
density	1.88 g/cm^3 (1 degree), 2.88 g/cm^3 (-100 degrees)
refractive index	1.37(1 degree),1.62(-100 degrees)
PMT Q.E.	28%
MgF_2 refractive index	1.44
MgF_2 absorption length	14.6 cm

Table 4.8: List of simulation parameters.

Using same simulation parameters except for density and refractive index, the difference of the p.e. distribution between ($T=-100$ degrees, $P=0.18$ MPa) and ($T=1$ degree, $P=5.5$ MPa) was simulated. The red line in Fig.4.40 and Fig.4.41 shows the result of the simulation. At ($T=-100$ degrees, $P=0.18$ MPa)

the mean value of pulse height (M_{ph}) is 41.5 ± 0.3 p.e. The simulated M_{ph} for (T=1 degree, P=5.5 MPa) is 52.7 ± 0.4 p.e., while the observed M_{ph} for this condition was 33.8 ± 0.6 p.e.. The relative scintillation light yield was obtained using the following equation :

$$eff_{acc} = \frac{M_{ph}(-100degrees, MC)}{M_{ph}(1degree, MC)} \quad (4.13)$$

$$Ratio = \frac{M_{ph}(1degree, data)}{M_{ph}(-100degrees, data)} \times eff_{acc} \quad (4.14)$$

As a result, the ratio of scintillation yield is

$$Ratio = 0.64 \pm 0.02(stat.) \pm 0.06(sys.) \quad (4.15)$$

The systematic error includes reproducibility error (0.03) and the increase of the PMT Q.E. \times gain error (0.05).

4.4.4 Expected sensitivity

In this subsection the expected sensitivity is discussed assuming the mass of ^{136}Xe is 1 ton, the run time is 5 years. The light yield at room temperature is about 29 photons/keV. Therefore the new detector design is useful for $0\nu 2\beta$ search as shown in Fig.4.37. The experiment of $0\nu 2\beta$ search is required high energy resolution to reject the events of $2\nu 2\beta$ which is standard double beta decay. Assuming the following conditions for the ELT detector,

- efficiency of wavelength shifter: 50%
- photon collection efficiency of ELT: 50%
- Q.E. of photosensor: 25%

the number of expected p.e. at Q-value (2.48MeV) is 4500 p.e. If the energy resolution is determined only by the photon statistics, the expected energy resolution is $1.5 \%_{RMS}$ at 2.48 MeV. Fig.4.43 shows the sensitivity of life time as a function of energy resolution. This plot only takes into account the $2\nu 2\beta$ background. In the case that the energy resolution is 1.5 %, the expected sensitivity of the life time reaches 10^{27} years.

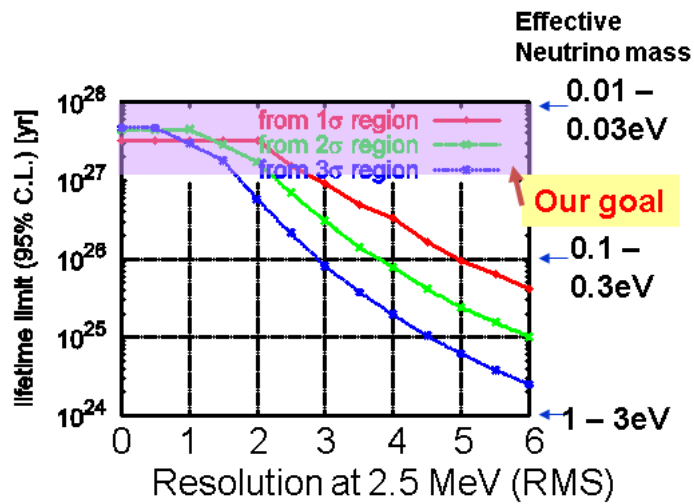


Figure 4.43: The life time limit of $0\nu 2\beta$ as a function of energy resolution using 1 ton ^{136}Xe for 5 years. The red, green and blue lines show the sensitivity assuming the signal window is $\pm 1\sigma$, $\pm 2\sigma$ and $\pm 3\sigma$, respectively. The life time of $2\nu 2\beta$ is assumed to be 8×10^{21} years.

Chapter 5

Pulse shape discrimination of liquid xenon

In this chapter, measurements and their results for the pulse shape discrimination (PSD) method are described.

The discrimination between the nuclear recoil and the electron recoil event is very useful for dark matter search experiments. In the case of xenon, double phase experiments like the XENON10 experiment use the ratio of primary scintillation (S1) and proportional scintillation (S2). On the other hand, for liquid argon experiments the pulse shape is used for discrimination because the two argon dimer states have vastly different lifetimes (about 6 nsec for the singlet and $1.6\mu\text{sec}$ for the triplet state).

As described in the previous chapter, the XMASS experiment is able to reach a sensitivity of $2.9 \times 10^{-44} \text{cm}^2$ without using particle discrimination. If the pulse shape of xenon scintillation can be used to discriminate nuclear/electron recoils, it would further improve the sensitivity of the XMASS experiment, and give independent support for dark matter signals if they are really detected.

In this chapter, the measurements for pulse shape discrimination of liquid xenon are described. As described in chapter 3, de-excitation is the origin of the scintillation emission. Two dimer states of xenon have decay times of 4.2ns and 22nsec, and this is believed to be the time constant of the nuclear recoil. On the other hand, in the case of electron recoils, the recombination process which has time constant of $\sim 45\text{nsec}$ is dominant in the time constant of scintillation emission. So, it could be possible to use PSD of xenon. However, careful evaluation of PSD is necessary at low energy ($\sim 5\text{keV}$) relevant for dark matter experiments.

As mentioned in section 4.2.7, the remaining BG after the 20cm fiducial volume cut in the low energy region is caused by mis-reconstruction of electron recoil events which happen near the edge of the detector with higher energy than reconstructed events. Therefore the pulse shape information is also useful for understanding the background of the XMASS experiment.

5.1 Detector setup for pulse shape measurement

A detector setup which held 3.3kg of liquid xenon and two PMTs was constructed for the PSD measurement. The setup was exposed to neutron and gamma ray sources. The data with the neutron source provided nuclear recoil events. On the other hand, the data with gamma ray source provided electron recoil events.

Fig.5.1 show a schematic view of the setup. The vessel which held the liquid xenon is shown in Fig.5.2. The vessel is made from SUS304 with an inner diameter of 10 cm and a height of 40 cm. The inside of the detector is shown in Fig.5.3 and Fig.5.4. Two hexagonal PMTs (PMT1 & PMT2) were set with a holder made from SUS304. The distance between the two PMTs was 6.0 cm. To increase light yield, a light guide made from PTFE surrounded the side of the liquid xenon volume. The total liquid xenon weight is 3.3kg which corresponds to 570 liters of xenon gas. To keep the temperature of liquid xenon at -100 degrees, the outer vacuum chamber (OVC) as shown in Fig.5.5 is used for heat insulation, and a copper cold finger connected to a liquid nitrogen reservoir was used. To control temperature a heater rolled around the vessel was used.

A ^{57}Co source and an LED were set at the center of the liquid xenon vessel to monitor the light yield of liquid xenon and the gain of the two PMTs. When the neutron data was taken, a ^{252}Cf fission source was used. A plastic scintillator and a PMT (PMT3) were set outside of the liquid xenon detector to tag the fission of ^{252}Cf . The spontaneous fission of ^{252}Cf emits several neutrons and gamma rays. The average number of neutrons emitted per fission is 3.8 . The energy distribution of neutrons is shown in Fig.5.6, and can be expressed as,

$$\frac{dN}{dE_n} = E_n^{1/2} e^{-E_n/T} \quad (5.1)$$

where $T = 1.42\text{MeV}$ [66]. Neutron events were selected using the time of flight (TOF) of neutrons. The distance between the ^{252}Cf and liquid xenon detector was 80cm.

The relation between the energy (E_n) of the incident neutron and TOF (t_n) is expressed as,

$$E_n = \frac{1}{2} M_n \left(\frac{d}{t_n} \right)^2 \quad (5.2)$$

where M_n is neutron mass (0.94GeV c^{-2}) and d is the distance between the ^{252}Cf source and the liquid xenon detector ($d=80\text{cm}$).

Lead bricks were put in front of the ^{252}Cf source in order to reduce the gamma rays entering the liquid xenon detector. For the electron recoil measurement, Compton electrons produced by gamma rays from a ^{137}Cs source were used. The ^{137}Cs source was set at 450mm from the center of the liquid xenon detector and a collimator made from a lead brick was used to reduce back scattered events.

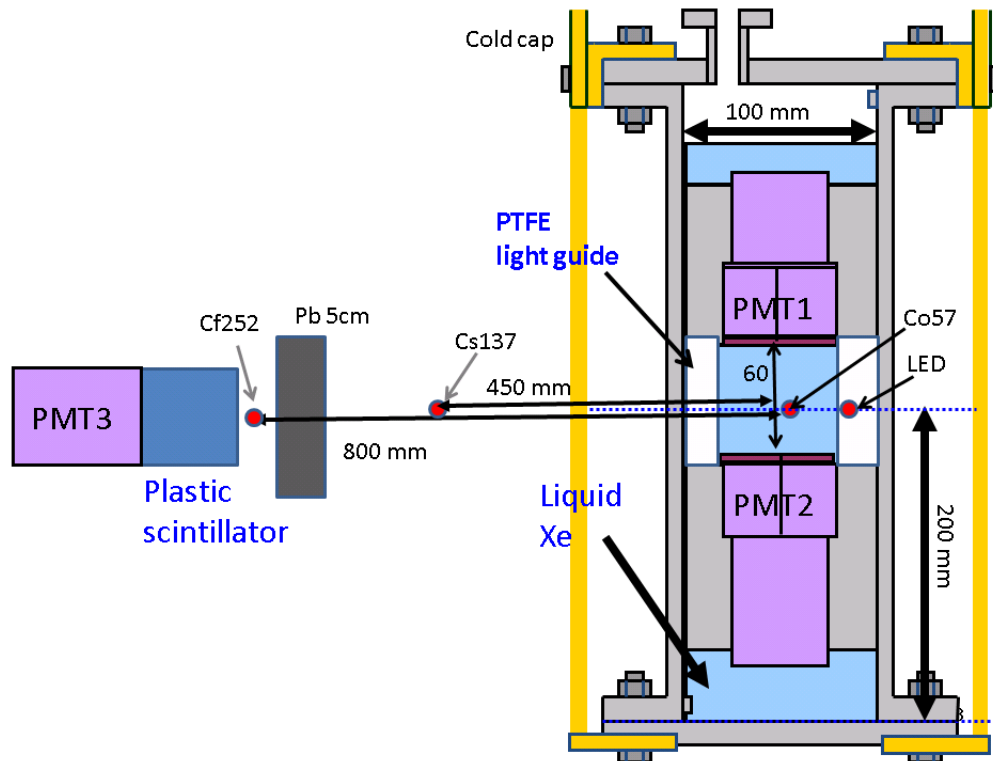


Figure 5.1: A schematic view of the detector used in the PSD measurement.



Figure 5.2: A picture of the liquid xenon detector. Two heaters were rolled to heat the detector outside of the detector.

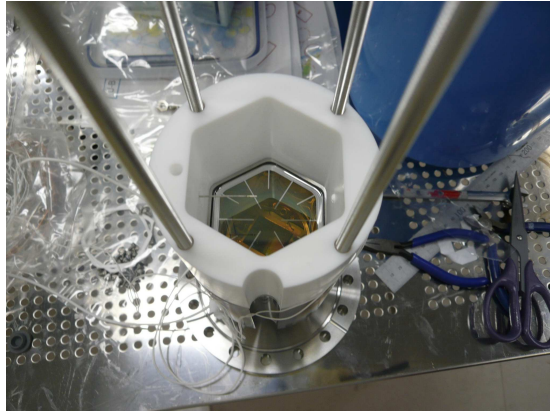


Figure 5.3: The picture of bottom PMT (PMT2) set in the PMT holder with its light guide made from PTFE.

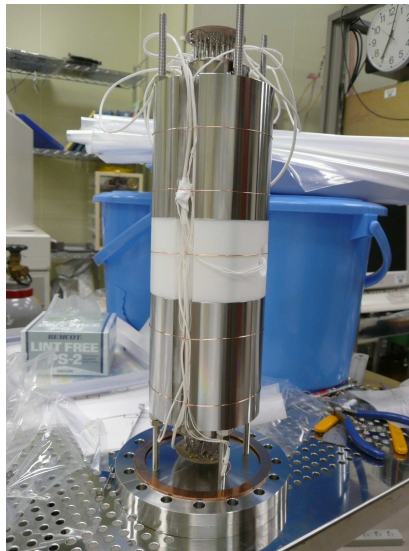


Figure 5.4: The picture of inner structure of the liquid xenon detector.



Figure 5.5: The picture of the OVC. The container of liquid nitrogen can be seen at the top.

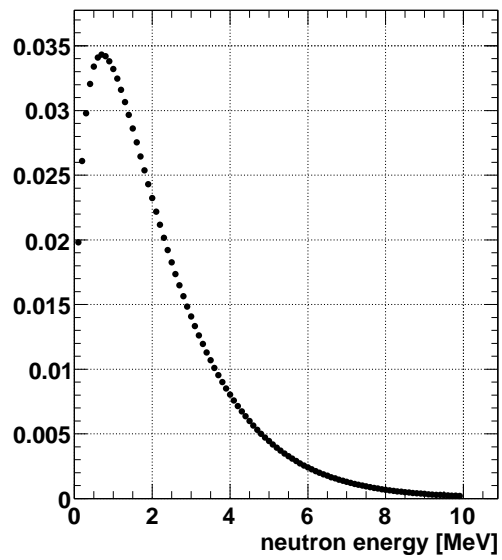


Figure 5.6: The energy spectrum of neutrons from a ^{252}Cf fission source assuming Eq.5.1.

5.2 Gas line

Fig.5.7 shows the gas line of this measurement. The xenon gas was passed through a SAES getter to remove impurities in the xenon. Table 5.1 shows the performance of the SAES getter. Before filling xenon gas, the liquid xenon detector was baked at 40 degrees Celsius for 24 hours under vacuum. The vacuum level reached 10^{-3} Pa at the head of the pump and the exhaust gas rate was 0.1 Pa/min.

Impurities	H ₂ O	O ₂	CO	CO ₂	N ₂	H ₂	CH ₄
Out gas	<1 ppb	<1 ppb	<1 ppb	<1 ppb	<1 ppb	<1 ppb	<1 ppb

Table 5.1: Guaranteed performance of SAES getter.

After baking, the OVC was evacuated and liquid nitrogen was filled in its reservoir to cool down the liquid xenon detector. When the temperature of the liquid xenon detector reached less than -100 degrees, xenon gas was supplied to the detector.

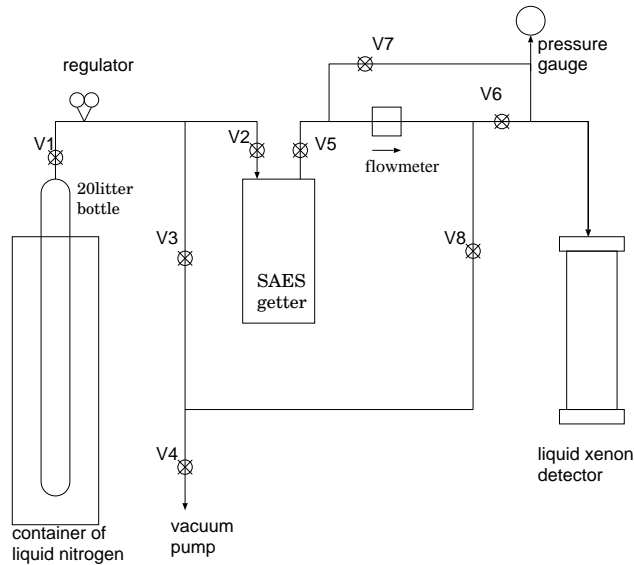


Figure 5.7: The schematic diagram of xenon gas line.

5.3 Data Acquisition System

Data was taken using a 1GHz Oscilloscope (Lecroy Wavepro900). The wave form was recorded for 10 μsec time range with 1 nsec resolution. The dynamic range of the voltage was 8 bits (+128 \sim -128 count). In this measurement the oscilloscope range was used at 50mV/div. Therefore an event the pulse height of which is larger than 400mV is saturated.

Fig.5.8 shows a diagram of the data acquisition system. Each PMT signal was divided into two cables by a divider. One cable was connected to the input channel of the oscilloscope. The other cable was amplified by a factor of 8 and then connected to a discriminator. The discriminator was fired when the input signal was more than 2 photo-electron (p.e.) equivalent, and the discriminator output with 100 nsec width is connected to a coincidence module.

The gamma-ray data was taken using the coincidence of PMT1 & PMT2. In the case of neutron runs, the PMT3 signal was used for tagging the fission of ^{252}Cf . A 140ns gate was opened after the PMT3 signal. Neutron data was taken using the coincidence of PMT1, PMT2 and PMT3.

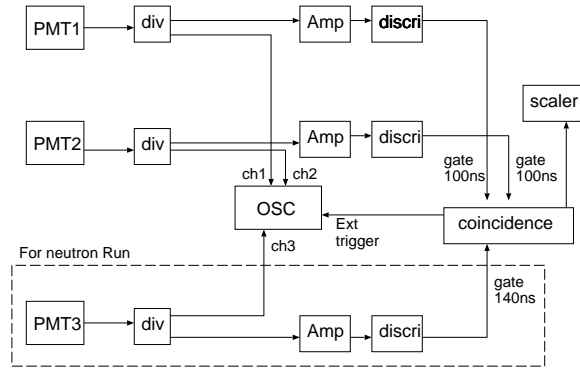


Figure 5.8: The schematic diagram of data acquisition system.

The gains of the PMT1 and PMT2 were set at 3.8×10^6 at -100 degrees with an applied high voltage of +1260V and +1210V, respectively. 1 p.e. signals were monitored using an LED.

5.4 Gain and light yield calibration

The neutron and gamma-ray source data were taken over about 5 days. The gain of the PMTs and the stability of the light yield of liquid xenon was monitored throughout the data taking period. Neutron and gamma-ray data taking started after the PMT gains became stable. That was usually about 20 hours after filling xenon into the detector. The 122 keV gamma rays emitted from a ^{57}Co source were used as a light yield monitor.

Fig.5.10 shows the source. 300Bq of ^{57}Co were enclosed in a thin stainless steel container with a diameter of 0.9 mm and a length of 32 mm. The ^{57}Co source was placed at the center of the detector.

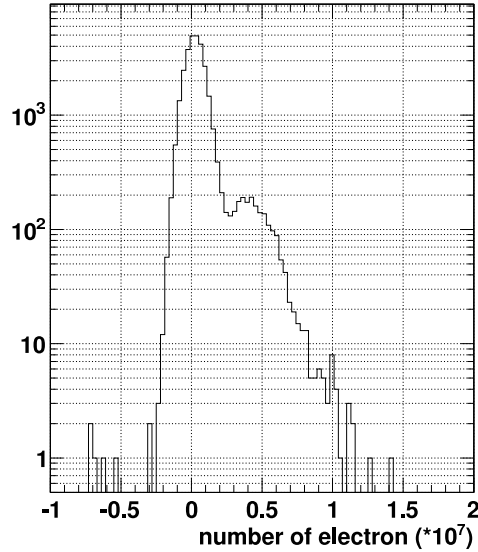


Figure 5.9: Typical integrated charge distribution of LED data for the gain calibration.

The gain of the PMTs was monitored using an LED light source. It was located at the center of the light guide as shown in Fig.5.1. The intensity of the LED was tuned to give approximately 1 p.e. signals at each PMT. Thus, the peak of the integrated charge distribution corresponds to a 1 p.e. signals and it is a good measurement of the PMT gains. LED calibration data was taken every day. Fig.5.9 shows a typical integrated charge distribution. The peak at $\sim 3.0 \times 10^6$ is due to the 1 p.e. signal. The peak was fit with a Gaussian function and the fitted central position is assumed to be the gain of the PMT.

Fig.5.11 and Fig.5.12 show the time variation of the gain of PMT1 and PMT2. Time 0 is the time when xenon filling was finished. The gain of the PMTs became nearly stable after about 20 hours. Therefore the neutron and gamma-ray source data were taken only after 20 hours had passed. There was up to 10% gain change even then, especially in PMT2. Therefore, the time variation of the gain was corrected in the following analysis.

In order to monitor the stability of the light yield of liquid xenon, the pulse height distribution of the ^{57}Co internal source was used. Fig.5.13 shows the total p.e. distribution of the ^{57}Co data, where the "total" is the sum of PMT1 and PMT2. The mean value from the Gaussian fit was 2.55×10^3 p.e. , which corresponds to 20.9 p.e./keV. The energy resolution was 5.4 % at 122keV.

Fig.5.14 and Fig.5.15 show the time variation of the 122 keV gamma ray peak over 5 days for PMT1 and PMT2, respectively. The change of the light yield is $1.11 \pm 0.26\%$ /day for PMT1 and $0.93 \pm 0.33\%$ /day for PMT2.

The energy resolution was also checked using the ^{137}Cs source. In order to avoid saturation of the PMT signal, the gain of the PMTs was decreased to 21% and 22% for PMT1 and PMT2, respectively. Fig.5.16 shows the p.e. distribution of the ^{137}Cs data. The energy resolution was 7.5% at 662keV. Light yield at 662keV was 19.5p.e./keV. The difference in light yields between 122keV and 662keV was 7%. This difference in light yield was caused by the non-proportionality of the scintillation yield [67].



Figure 5.10: A picture of the ^{57}Co source.

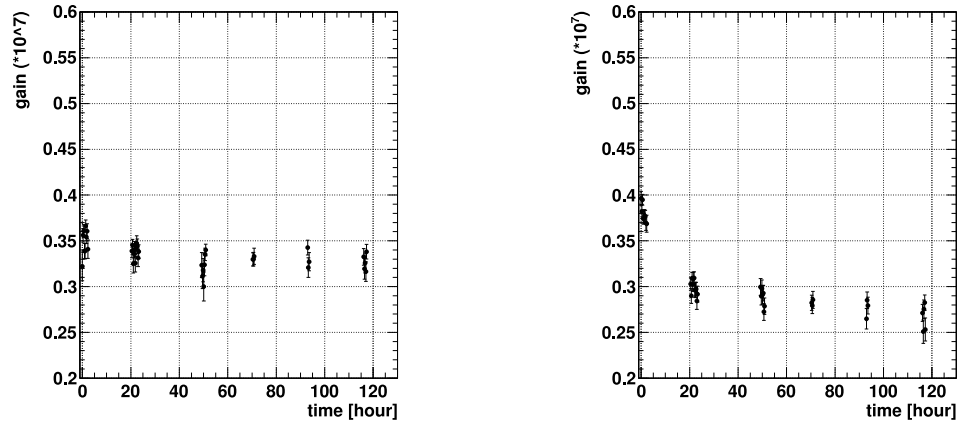


Figure 5.11: Time variation of the gain of Figure 5.12: Time variation of the gain of PMT1. PMT2.

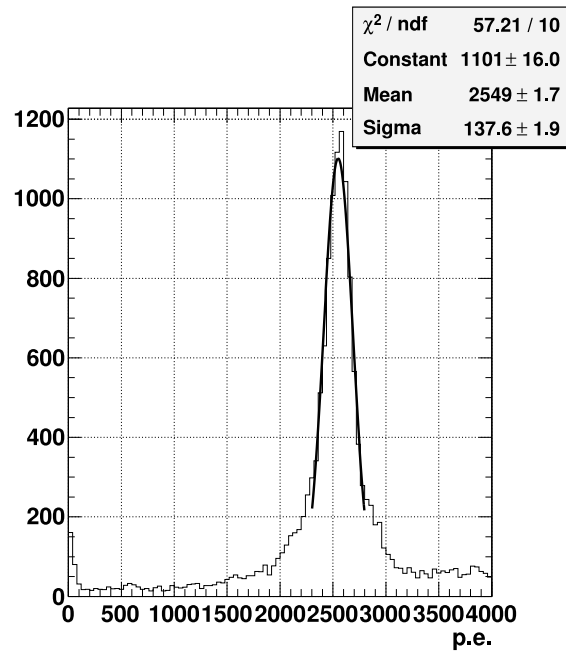


Figure 5.13: A typical total p.e. distribution of ^{57}Co data.

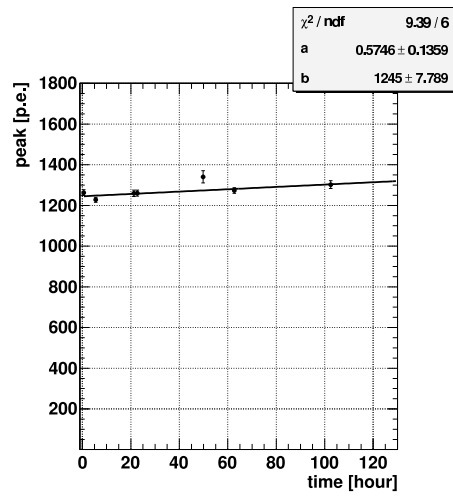


Figure 5.14: Time variation of the ^{57}Co peak value of PMT1.

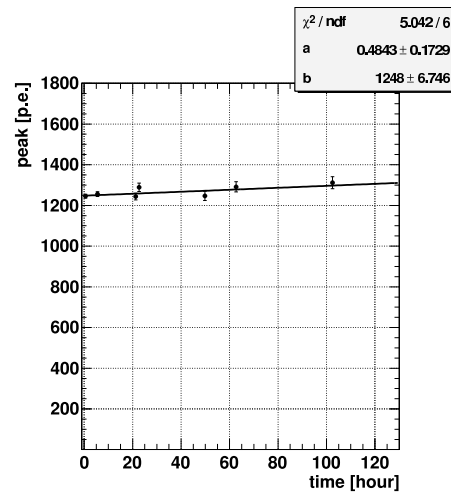


Figure 5.15: Time variation of the ^{57}Co peak value of PMT2.

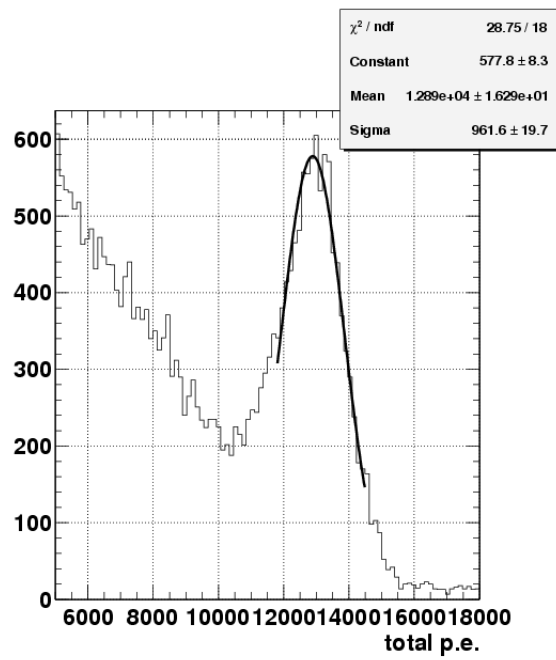


Figure 5.16: The p.e. distribution of the ^{137}Cs data.

5.5 Data reduction

The summary of neutron and gamma-ray source data is given in Table 5.2.

Source	trigger rate	Real time (hour)	Live time (hour)	number of recorded events
neutron	13.2 Hz	43.3	16.8	8.0×10^5
gamma ray	4.52 kHz	1.33	0.02	4.0×10^5
BG(including ^{57}Co)	912 Hz	2.75	0.2	6.6×10^5

Table 5.2: Summary of neutron, gamma ray and BG data. The BG data included events from the ^{57}Co source.

In order to purify the neutron and gamma-ray samples, several cuts are applied. Detail of the cuts are described in this section.

5.5.1 Pre-activity cut

Fig.5.17 shows a typical wave form. The offset of the oscilloscope signal was adjusted to 115 counts. The external trigger position was set at 260nsec, such that the waveform from 260nsec before trigger was recorded. The charge and maximum pulse height of each event was calculated with the following steps,

- The baseline calculation
The baseline of the event was determined using the mean counts (M_{base}) from 0 to 150nsec.

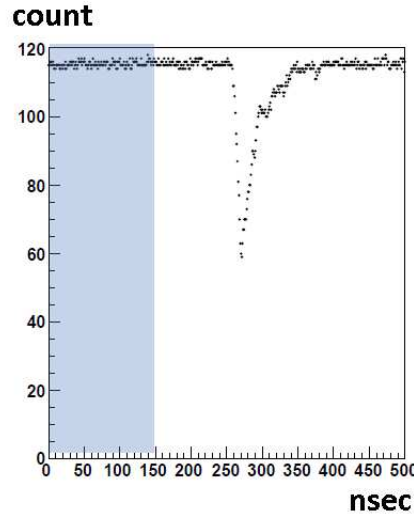


Figure 5.17: The typical wave form. The shaded region was used to determine the baseline.

$$M_{base} = \sum_{t=1}^{150} \frac{i(t)}{150} \quad (5.3)$$

Fluctuation of the baseline was estimated by S_{base} defined as,

$$S_{base} = \sqrt{\sum_{t=1}^{150} \frac{(i(t) - M_{base})^2}{150}} \quad (5.4)$$

where $i(t)$ is the count value at time t .

- charge integration

The charge integration was started from the point where the signal crosses 112 counts for the first time, which is defined as the leading edge. This signal level at the leading edge corresponds to ~ 3 p.e. since the pulse height of 1 p.e. corresponds to 1.3 counts. The leading edge was searched for from the timing point of 150 nsec. The width of the integration was 200nsec from the leading edge. The maximum pulse height was searched for in this 200nsec window.

M_{base} and S_{base} were calculated for each event individually. If noise or accidental events happened in the time range from 0nsec to 150 nsec, the calculated charge and maximum pulse height may be shifted. Therefore, a cut to reject events with pre-activity was applied. Fig.5.18 shows the distribution of M_{base} and S_{base} for each PMT. Events with more than $\pm 2\sigma$ deviation from the mean value were cut, called the pre-activity cut.

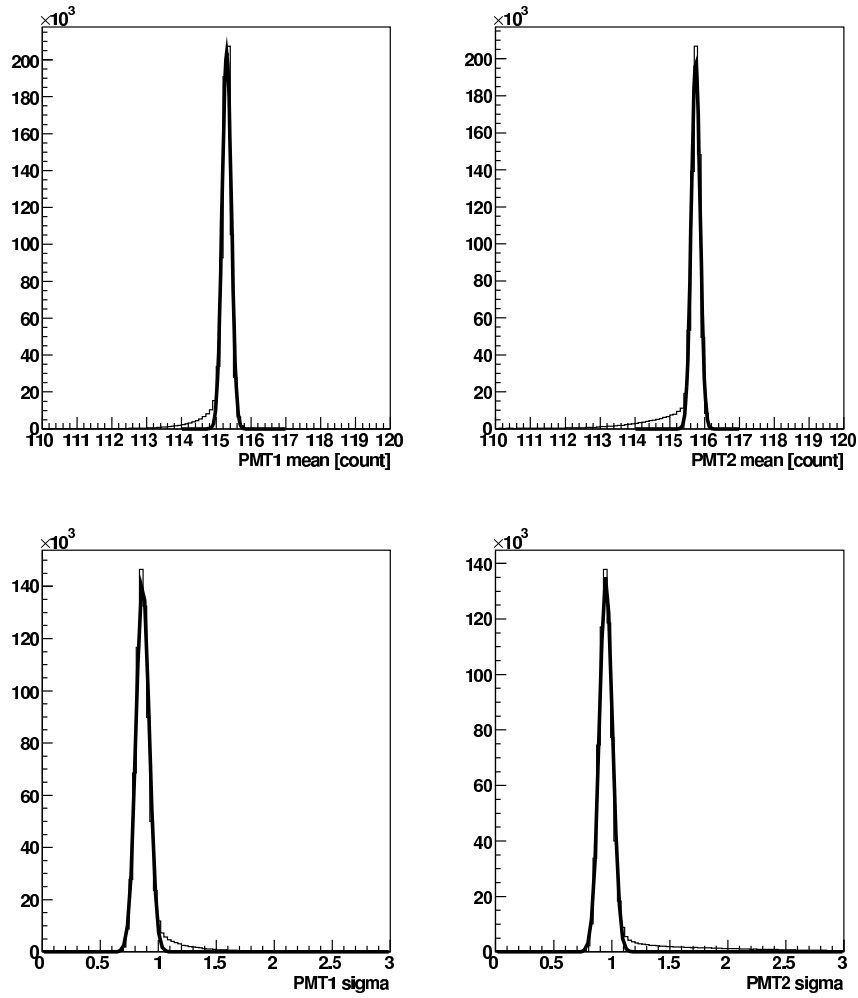


Figure 5.18: The distributions of M_{base} and S_{base} . Events for the final samples were selected from within $\pm 2\sigma$ from the mean value.

5.5.2 Saturation cut

Events whose maximum pulse height is close to the overflow of the dynamic range of the oscilloscope (8bit) were rejected. Fig.5.19 shows the scatter plot between total p.e. and the pulse height for PMT1. Events with less than 1000 p.e. were recorded without saturation. Therefore events with a maximum pulse height less than 350mV were selected.

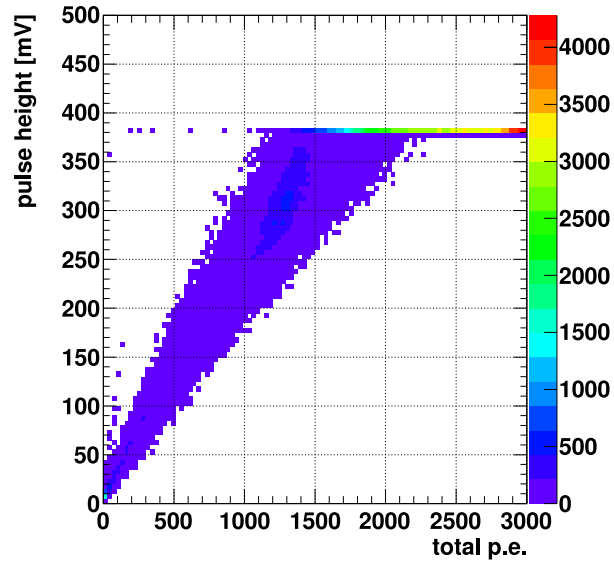


Figure 5.19: Scatter plot between total p.e. and pulse height for PMT1.

5.5.3 Timing cut for neutron selection

The neutron events were selected using a time of flight measurement. Fig.5.20 shows the time difference of the leading edges from PMT2 and PMT3 signals, called TOF. The peak around time 0 is caused by fission gamma rays producing scintillation in the liquid xenon. A lead brick is placed between the ^{252}Cf source and liquid xenon, but some gamma rays penetrate or back scatter to reach the liquid xenon volume.

Events with $\text{TOF} > 15$ nsec are due to the case when neutrons produce nuclear recoils that give rise to scintillation in the liquid xenon volume. To confirm the TOF of gamma rays, ^{60}Co data was taken. ^{60}Co emits two gamma rays at the same time, giving rise to events where one gamma ray is recorded in PMT3 and the other interacts in the liquid xenon. Fig.5.21 shows the TOF distribution for the ^{60}Co run. Only the $\text{TOF} \sim 0$ peak was observed in the case of gamma source.

Neutron events from two TOF ranges are selected: one is TOF from 15 to 30 nsec and another from 30 to 40 nsec. Fig.5.22 and Fig.5.23 show the p.e. distribution of a ^{252}Cf Run for each of the TOF ranges, respectively. Recoil events including inelastic scattering were observed. The two different TOF windows select different energy windows for the incident neutrons. To estimate the systematic error about the energy of the incident neutron, those two TOF windows were analyzed, separately.

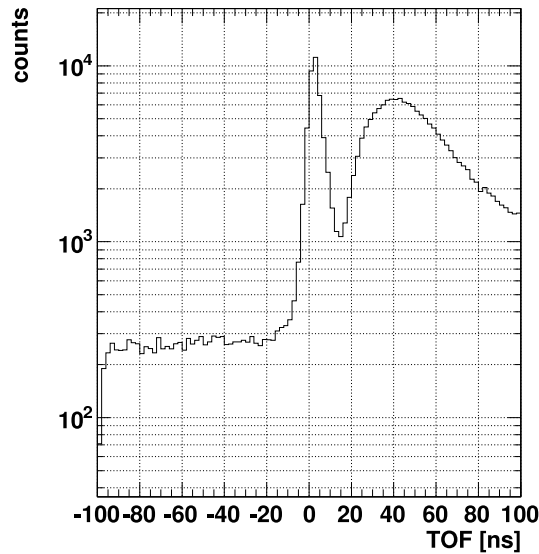


Figure 5.20: TOF distribution of ^{252}Cf Run.

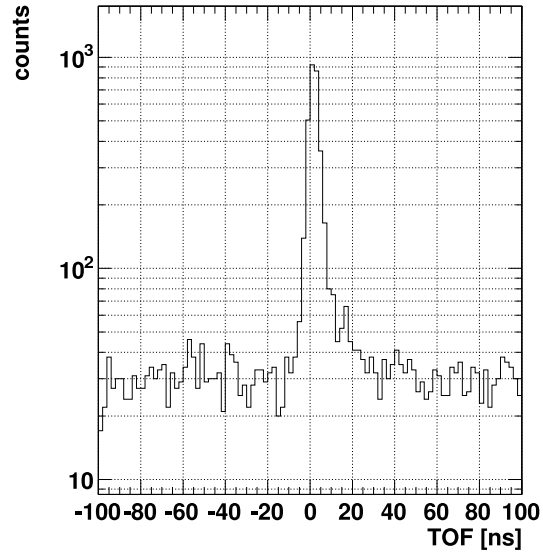


Figure 5.21: TOF distribution of ^{60}Co Run.

5.5.4 Summary of the data reduction

The number of events taken in neutron and gamma ray runs were 8.0×10^5 and 4.0×10^5 events, respectively. Table 5.3 shows the data reduction summary.

	^{252}Cf (neutron) Run	^{137}Cs (gamma ray) Run
No cut	8.0×10^5	4.0×10^5
Pre-activity cut	5.6×10^5 (69.4%)	3.5×10^5 (88.2%)
Saturation cut	2.2×10^5 (27.1%)	7.4×10^4 (18.4%)
neutron selection cut (15~30nsec)	2.2×10^4 (2.73%)	
neutron selection cut (30~40nsec)	2.7×10^4 (3.41%)	

Table 5.3: Cut summary for PSD measurement.

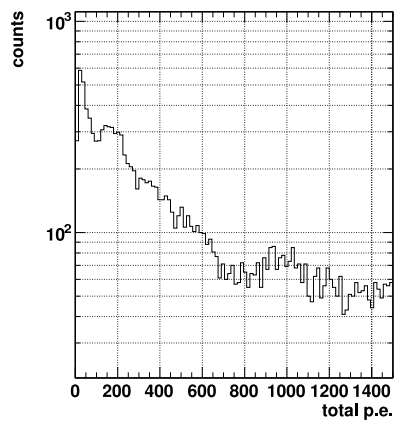


Figure 5.22: Total p.e. distribution for TOF from 15 to 30 nsec.

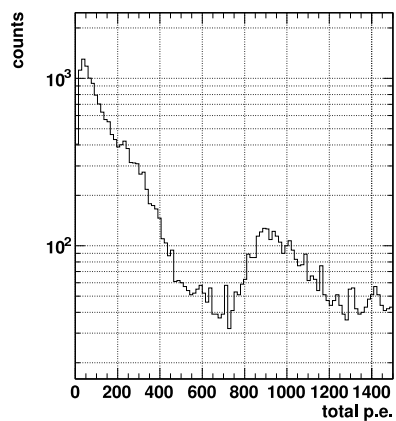


Figure 5.23: Total p.e. distribution for TOF from 30 to 40 nsec.

5.6 PSD

There are various methods to compare the pulse shape difference. The most popular ones are the fitting method of slope, mean timing method, and the prompt/total method. The fitting method of slope is useful for understanding the basic features of PSD. However, in the case of dark matter search in which light yield is small in each event, fitting error is too large to discuss PSD for event by event basis.

The mean timing method uses the time difference between the leading edge and the time at which the pulse has fallen by the several percentage from its peak position. In this method, the full information from the pulse is not used.

On the other hand, the prompt/total method fully utilizes the PSD information especially for liquid xenon because most of the excitation photons are in the prompt time window while the protons through recombination are often outside the prompt window. As described in section 3.6, the fundamental difference of pulse shapes between nuclear recoils and electron recoils is due to the time scale of the recombination process.

Because of the reasons described above, we have selected the prompt/total method for this PSD study. The prompt/total method defines a ratio of the waveform integrals over two different time windows. The time intervals for the prompt and the total are optimized to maximize the PSD performance, which will be discussed in detail in section 5.6.3. After the optimization, we have chosen a prompt timing window of 20nsec and a total time window of 200 nsec from the leading edge.

Fig.5.24 shows the schematic view of the prompt and total time windows. The following ratio was defined to evaluate PSD,

$$PSDratio = \frac{PromptPE(PMT1) + PromptPE(PMT2)}{totalPE(PMT1) + totalPE(PMT2)} \quad (5.5)$$

5.6.1 Neutron data

The recoil energy (E_r) of xenon scattered by a neutron with energy E_n is expressed by the following equation,

$$E_r = E_n \frac{2(A + 1 - \cos^2 \theta - \cos \theta \sqrt{A^2 - 1 + \cos^2 \theta})}{(1 + A)^2} \quad (5.6)$$

where A is the mass number of the recoil nucleus, and θ is the scattering angle of the neutron.

The maximum recoil energy at $\theta \sim 180^\circ$ is 220 keV_r for a neutron with 8 MeV. Assuming $L_{eff} \sim 0.2$, the maximum visible energy for a 8 MeV neutron recoil is 44 keV_{ee}.

The trigger rate of the ²⁵²Cf Run was 13.2Hz (PMT1&PMT2&PMT3). The trigger rate of only PMT3 was 16.2kHz and that of PMT1 & PMT2 was 1.12kHz. The width of the gate to make the trigger was 100nsec for PMT1 and PMT2, 140nsec for PMT3. Therefore 33% (= 4.4Hz/13.2 Hz) were caused by accidental coincidences.

Fig.5.25 shows the TOF distribution for several low p.e. ranges. Most of the accidental events were caused by gamma rays with a large energy deposit in

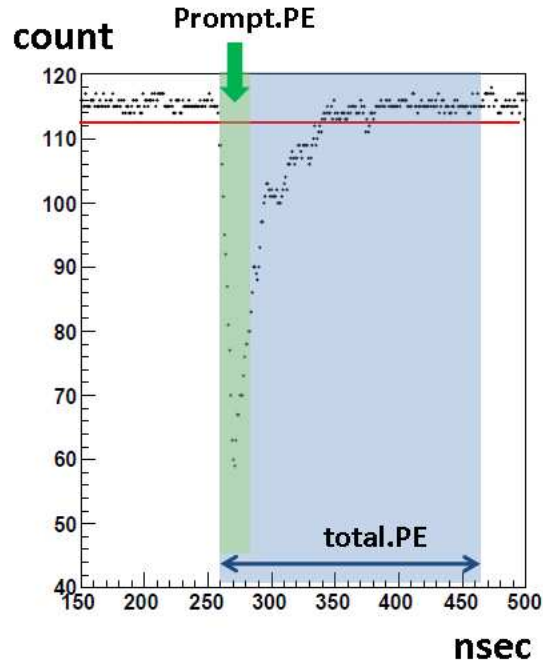


Figure 5.24: A typical waveform. The green and blue regions show the prompt and total integration intervals. The red line shows the 112 counts line that determines the leading edge.

the liquid xenon. Therefore the accidental events at low p.e. range were much smaller. Table 5.4 shows the number of events for several TOF ranges (-90 ~ -30nsec, 15~30nsec and 30~40nsec) and the contamination rate by accidental events assuming the accidental events have a flat distribution.

The contamination is less than 1~2% in most of the cases. Fig. 5.26 and Fig. 5.27 show the relation between total p.e. and the *PSDRatio* for TOF=15~30 nsec and TOF=30~40 nsec, respectively. In the low p.e. region a nuclear scattering like cluster is observed. In addition, at 800 p.e. ($\sim 40 \text{ keV}_{ee}$), a nuclear scattering cluster including inelastic gamma rays is observed.

5.6.2 Gamma-ray data

Gamma ray data was taken using a ^{137}Cs source. The trigger rate of the ^{137}Cs Run was 4.52kHz (PMT1&PMT2). The trigger rate without the source was 912Hz. Fig. 5.28 and Fig. 5.29 show the p.e. spectrum of the ^{137}Cs run including BG and that of ^{137}Cs run after BG subtraction, respectively. Table 5.5 shows the contamination of BG events.

Fig. 5.30 shows the relation between total p.e. and *PSDRatio*. The *PSDRatio* gets smaller as the total p.e. gets larger.

	-90~-30nsec	15~30 nsec		30~40 nsec	
		event	expected accidental event	event	expected accidental event
50~100p.e.	236	1072	59 (5.5%)	3245	40 (1.2%)
100~150p.e.	88	990	22 (2.2%)	2165	15 (0.7%)
150~200p.e.	59	1026	15 (1.4%)	1586	10 (0.6%)
200~250p.e.	44	867	11 (1.3%)	1329	8 (0.6%)
250~300p.e.	29	629	8 (1.2%)	1057	5 (0.5%)
300~400p.e.	45	1137	12 (1.0%)	1377	8 (0.5%)

Table 5.4: Estimates of the contamination by accidental events for the two TOF windows.

p.e.	50~100	100~150	150~200	200~250	250~300	300~400
BG contamination	25%	16%	19%	16%	15%	18%

Table 5.5: The contamination of BG events.

5.6.3 Optimization of the PSD parameter

To optimize the PSD parameter, timing windows of 10, 15, 20, 30, 40 and 50nsec were explored. Fig.5.31 shows the difference in means between ^{252}Cf and ^{137}Cs divided by the sigma of ^{137}Cs for several PSD windows. The 20nsec window was the best PSD window for almost all energy ranges.

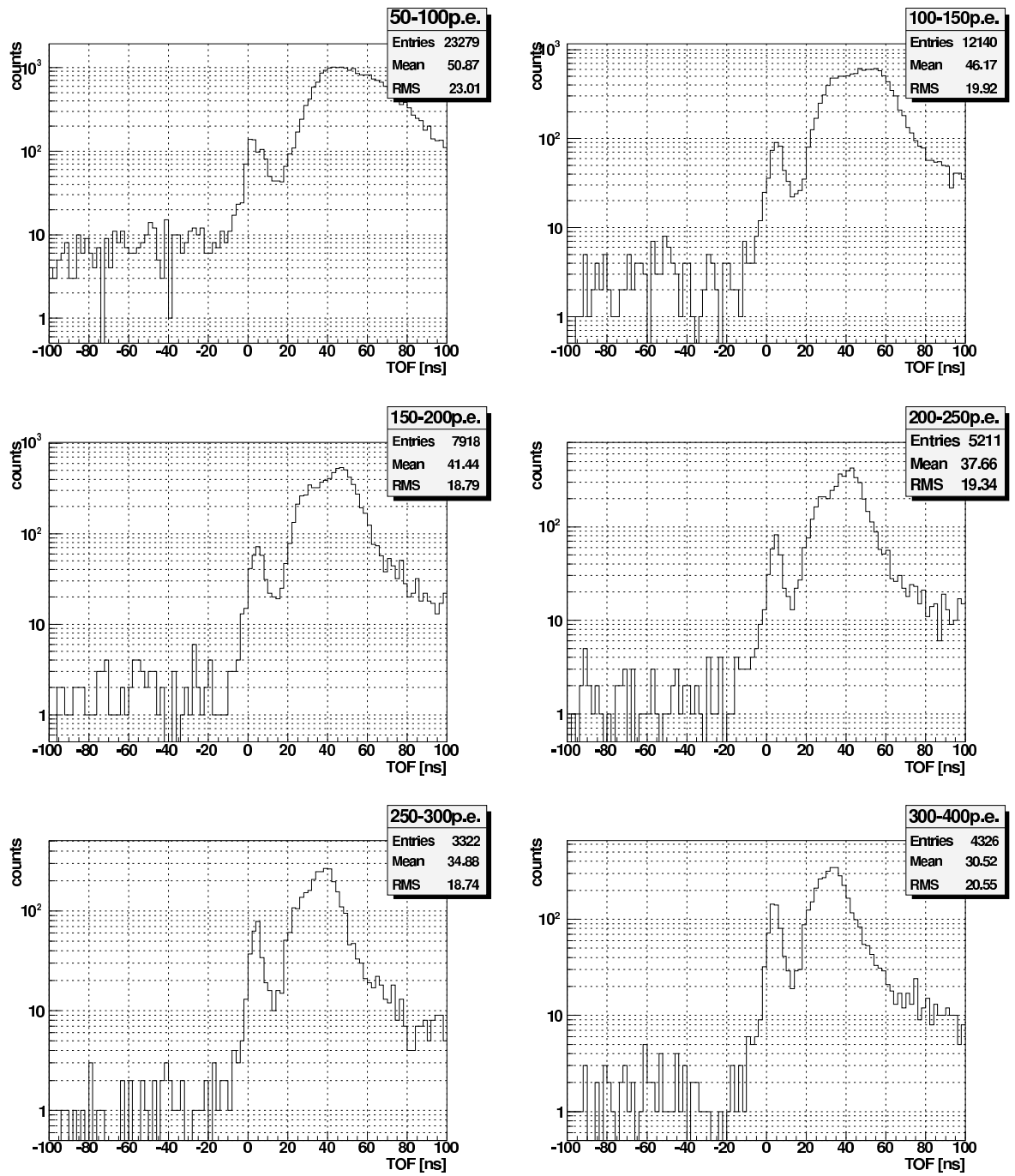


Figure 5.25: TOF distribution of low p.e. ranges from 50p.e. to 400p.e. in the ²⁵²Cf data.

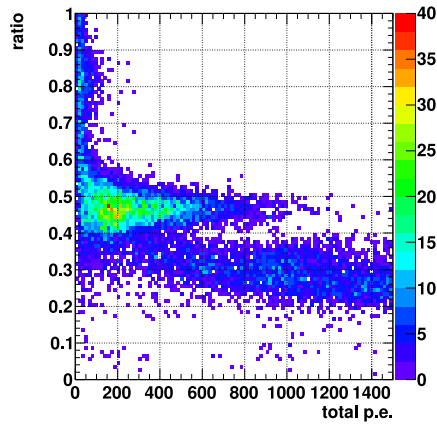


Figure 5.26: Scatter plot between total p.e. and *PSDratio* for TOF from 15 to 30 nsec in the ^{252}Cf data.

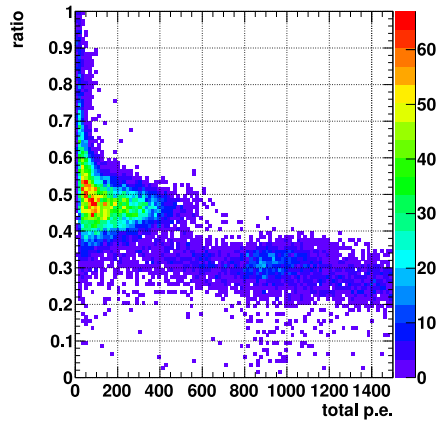


Figure 5.27: Scatter plot between total p.e. and *PSDratio* for TOF from 30 to 40 nsec in the ^{252}Cf data.

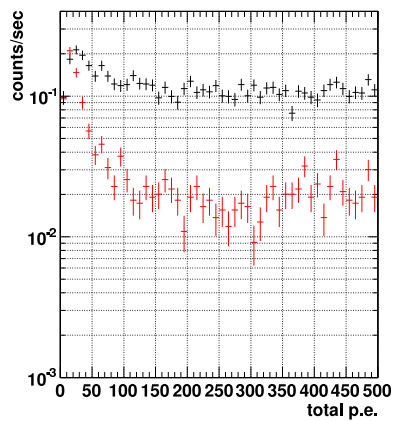


Figure 5.28: The ^{137}Cs p.e. spectrum (black) and BG p.e. spectrum (red) .

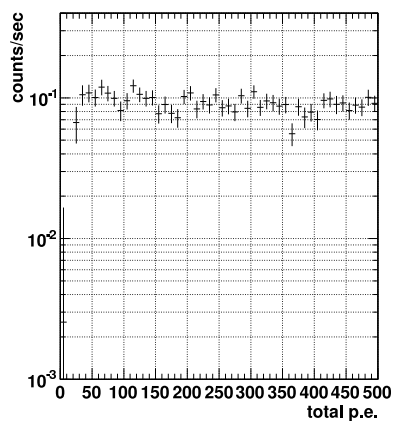


Figure 5.29: The ^{137}Cs spectrum after BG subtraction.

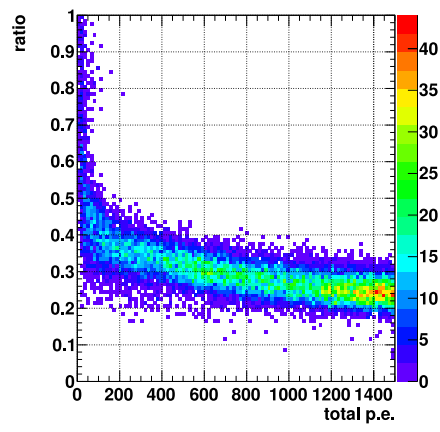


Figure 5.30: The ^{137}Cs scatter plot between total p.e. and PSD_{ratio} .

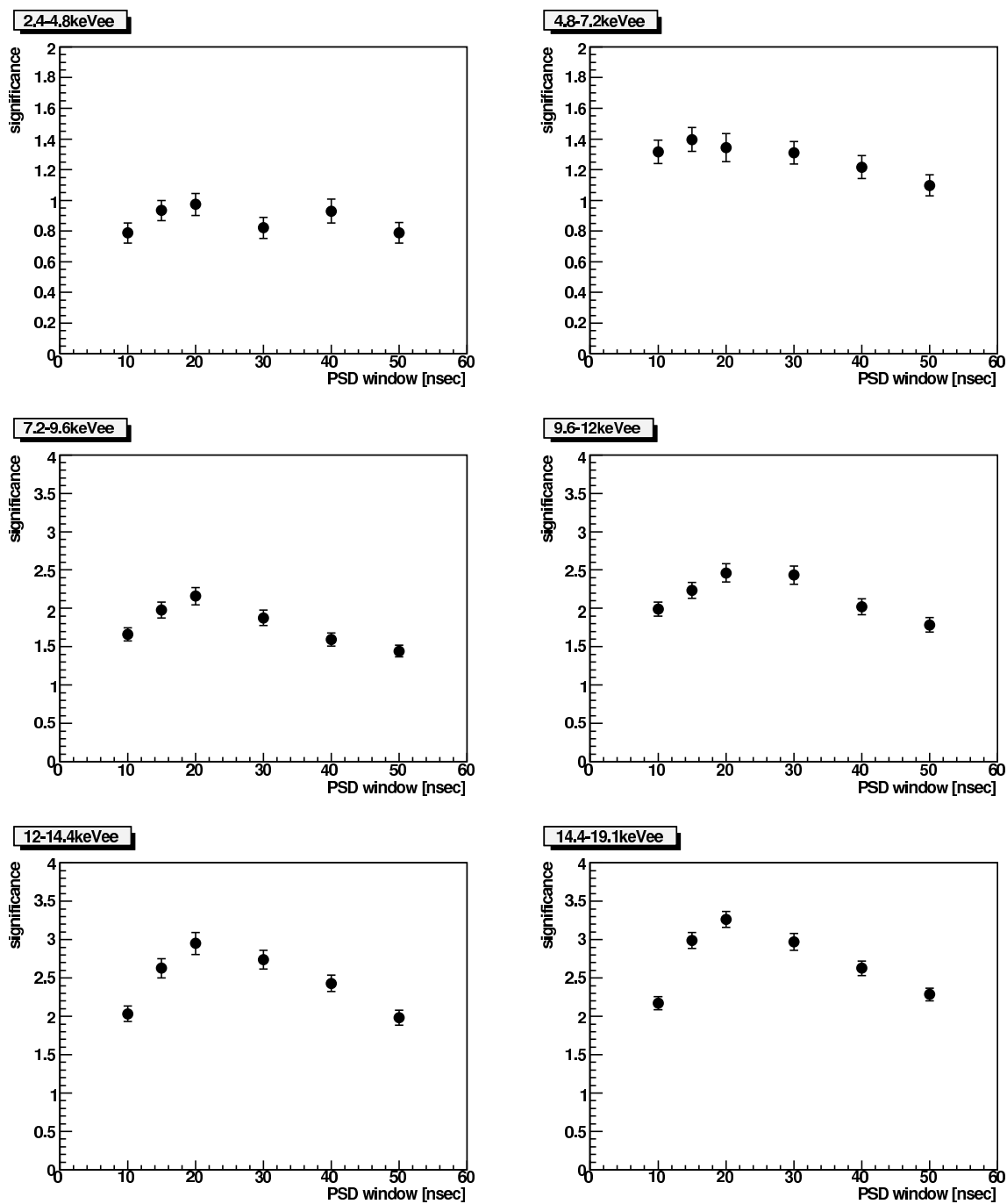


Figure 5.31: The significance distribution, which is the difference in means between ^{252}Cf and ^{137}Cs divided by the sigma of ^{137}Cs as a function of the width of the prompt timing window. The vertical axis shows the value of sigma.

5.7 PSD result

PSD was evaluated for p.e. ranges of 50~100, 100~150, 150~200, 200~250, 250~300 and 300~400 p.e.. Using a conversion factor of 20.9 p.e./keV_{ee}, these p.e. ranges correspond to 2.4~4.8, 4.8~7.2, 7.2~9.6, 9.6~12, 12~14.4 and 14.4~19.1 keV_{ee}. Fig.5.32 shows the *PSDRatio* distributions for each energy range. The black line shows the ¹³⁷Cs data and the red line shows the ²⁵²Cf data. Each data set was fitted using a Gaussian distribution function. The rejection power was estimated in the following way:

- The difference in means (M_{dif}) of the *PSDRatio* distributions between the ¹³⁷Cs and ²⁵²Cf was calculated for each energy range.
- The M_{dif} was divided by the σ of the ¹³⁷Cs distribution. The rejection power of gamma rays is evaluated at the point where the efficiency for nuclear recoil is 50 %.

Fig.5.33 shows the result of the rejection power as a function of recoil energy in keV_{ee}. The black and red points show the data using neutron selection TOF windows of 15~30nsec and 30~40nsec. For the 4.8~7.2 keV_{ee} data the rejection power was more than 1 order of magnitude greater with 50% efficiency for nuclear recoil events.

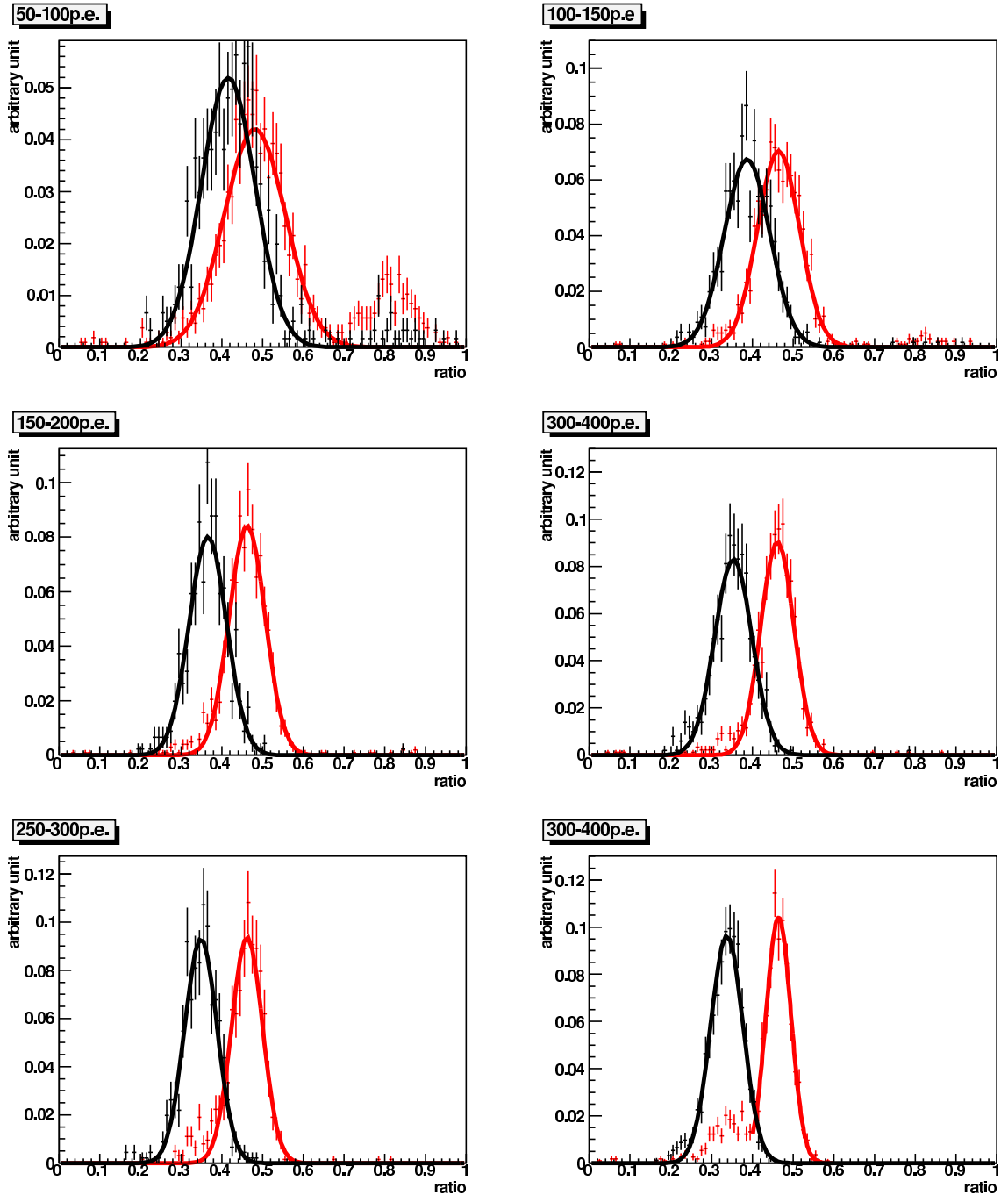


Figure 5.32: The *PSDratio* distribution of each p.e. range. The black and red line show the ^{137}Cs data and the ^{252}Cf data, respectively. The peaks around 0.8 in the upper left figure was due to Cherenkov lights generated in the PMT windows. In the bottom right figure, the nuclear recoil data contained inelastic reactions which accompanied gamma ray emissions and caused a bump around 0.35.

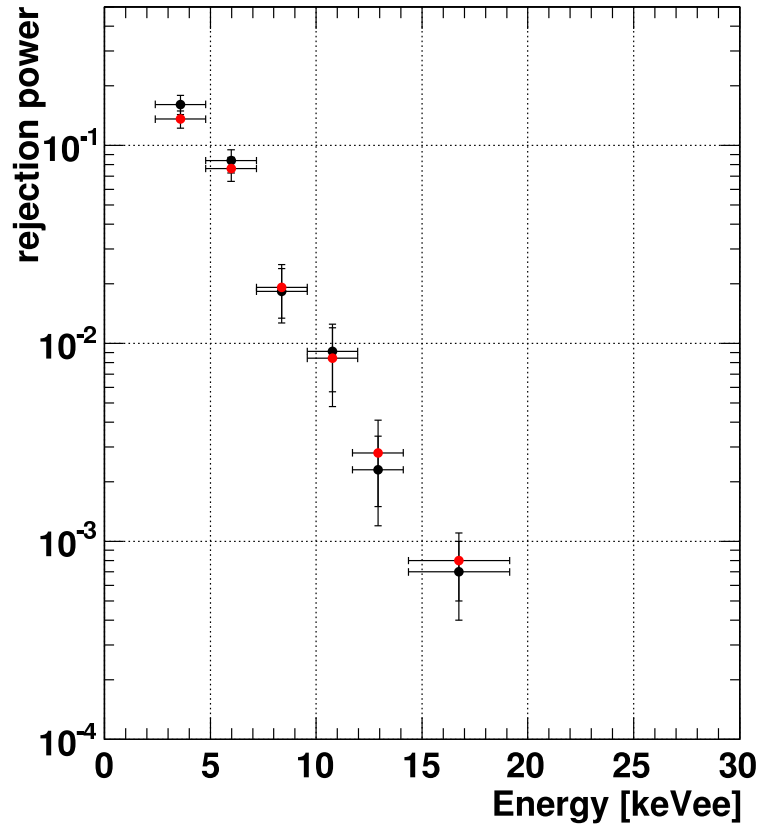


Figure 5.33: Rejection power as a function of energy in keV_{ee} . The black and red points show the neutron data for the 15~30nsec and 30~40nsec TOF windows, respectively.

5.8 Spread of the *PSDratio* distribution

As seen in Fig.5.32, the *PSDratio* distributions have some spread. The spread could be due to the statistics of the observed number of p.e. and some physics mechanism which may cause event by event fluctuation. In order to understand the reason for the spread, the *PSDratio* distributions were compared with a MC simulation. The MC was made with the following steps,

- Step 1: A total p.e. (T_{mc}) was selected randomly from 50 to 400p.e..
- Step 2: The *PSDratio* was calculated using the fit function shown in Fig.5.34.
- Step 3: Using the total p.e. and the *PSDratio*, the prompt p.e. (P_{mc}) was produced randomly using the binominal distribution.

$$P(k) = {}_n C_k p^k (1-p)^{n-k} \quad (5.7)$$

where $n = T_{mc}$, $p = PSDratio$ and k is produced value as a P_{mc} .

- Step 4: the *PSDratio* was calculated as (P_{mc}/T_{mc}) .

The *PSDratio* distribution was made repeating Step 1~ 4. Then, the distribution was fit with a Gaussian function and the fitted sigma value was calculated.

It was found that the mean values of *PSDratio* were reproduced in the MC. On the other hand, Fig.5.35 and Fig.5.36 show the sigma value as a function of the total p.e., for ^{137}Cs and ^{252}Cf , respectively. The difference between the MC and data for ^{252}Cf was smaller than that for ^{137}Cs .

As mentioned in section 3.4 and 3.6, in the case of electron recoils the density of excitons spreads over a wide region. Therefore the recombination process of electron recoil events is slow. On the other hand, in the case of nuclear recoil, the density of excitons is high and recombination happens in much shorter time than the recombination of electron recoils. Because of those phenomenological considerations, the extra spread of ^{137}Cs data could be due to fluctuations in the recombination process, which is caused by fluctuations of each individual track.

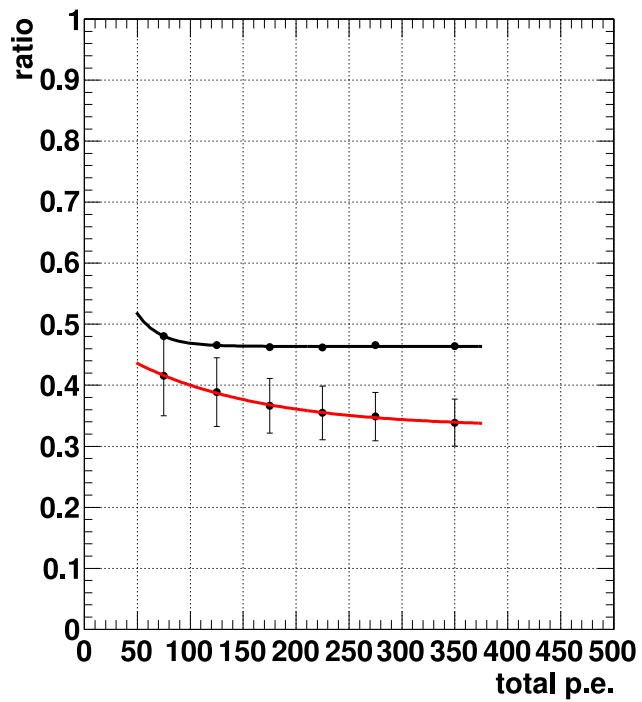


Figure 5.34: The relation between *PSDratio* and total p.e.. The black and red lines show the fit function of ^{252}Cf and ^{137}Cs . The error bars of ^{137}Cs represent the 1 sigma deviation from the mean value.

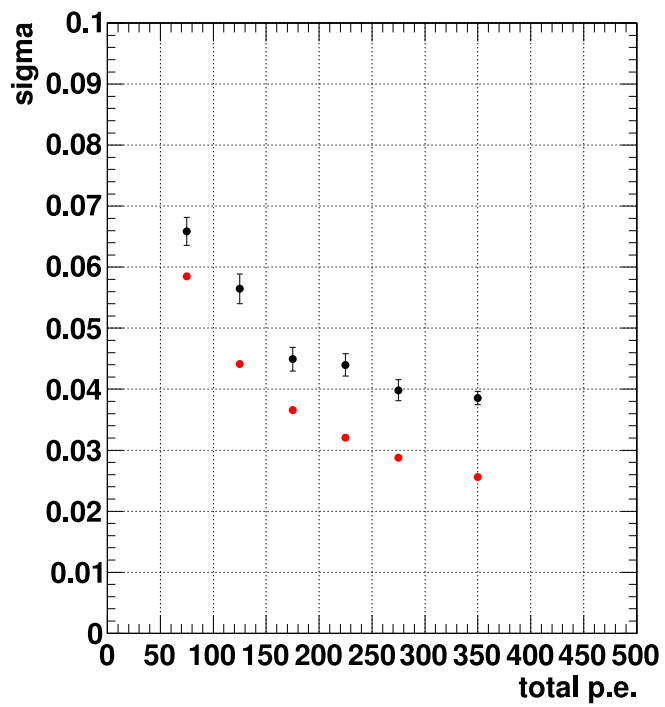


Figure 5.35: The sigma distribution of ^{137}Cs for each p.e. range. The black and red points show data and MC respectively.

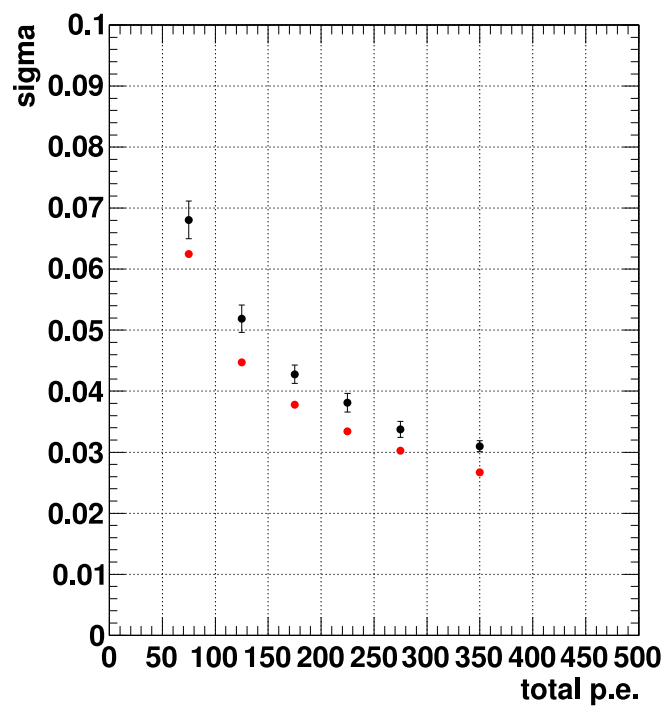


Figure 5.36: The sigma distribution of ^{252}Cf for each p.e. range. The black and red points show data and MC respectively.

5.9 Light yield dependence of PSD

In this section, the light yield dependence of PSD is evaluated. As noted in the section 4.2.6, the expected light yield for the XMASS experiment is about 4.6 p.e./keV. To estimate the rejection power in the XMASS experiment, a new set of data was taken with reduced light yield. In order to reduce the light yield, a mask made from copper was placed on the bottom PMT (PMT2) as shown in Fig.5.37.

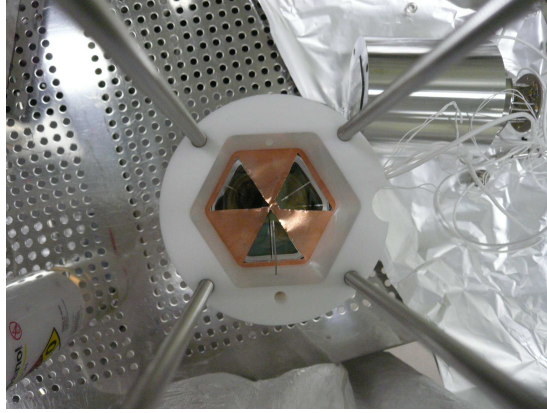


Figure 5.37: A picture of the mask on the bottom PMT (PMT2). The light yield was reduced to half using this mask.

The light yield of PMT2 was decreased to 4.6 p.e./keV as shown in Fig.5.38. The energy resolution using one PMT was 11.7% at 122keV. The light yield was stable with a fitted time variation of $0.57 \pm 0.42\%$ /day as shown in Fig.5.39.

The same cuts as described in section 5.5 were applied only for PMT2. The relation between PSD_{ratio} and PMT2 p.e. for ^{137}Cs and ^{252}Cf runs are shown in Fig.5.40 and Fig.5.41. In addition, Fig.5.42 shows PSD_{ratio} distributions for each energy range. The mean value and sigma were also compared with that of the data without the mask which gave a total p.e.(PMT1+PMT2) of 20.9p.e./keV. Fig.5.43 and Fig.5.44 show the mean value for ^{137}Cs and ^{252}Cf runs, respectively.

The difference in the mean value between the data without the mask and with the mask was less than 5%. This result shows that the light yield dependence of the mean of the PSD_{ratio} is small.

Fig.5.45 and Fig.5.46 show the sigma value obtained from ^{137}Cs and ^{252}Cf runs, respectively. The green points show the results of MC simulation.

Even though there is a large difference between ^{137}Cs data and MC for the non-masked data, the difference between ^{137}Cs data and MC for the masked data seems to be less than 10%. The light yield was reduced by a factor of four compared with the masked PMT2 and the sum of PMT1 and PMT2 for non masked data, thus the sigma due to photon statistics is increased by a factor of 2. Because the relative contribution of the unknown component is reduced in the masked data, the agreement between MC and data looks to have improved.

The sigma of the unknown component is estimated from the following rela-

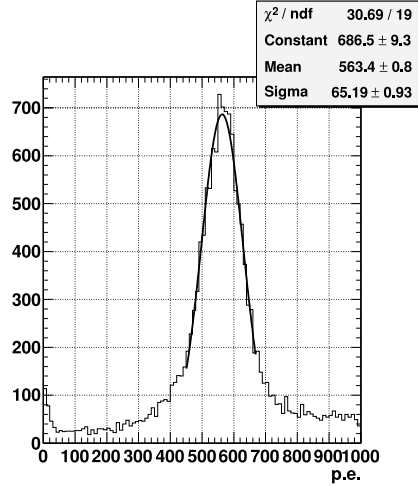


Figure 5.38: A typical p.e. distribution of ^{57}Co data for PMT2. The light yield was reduced to 4.6 p.e./keV $_{ee}$ by a mask.

tion, assuming that the sigma of the photon statistics is correctly simulated in the MC:

$$\sigma_{unknown} = \sqrt{\sigma_{data}^2 - \sigma_{MC}^2} \quad (5.8)$$

Table 5.6 shows the estimated $\sigma_{unknown}$ with its error. The error is large in the masked data, however the two measurements of $\sigma_{unknown}$ are consistent with each other within their errors. In the masked data runs, PMT1 was left in the same configuration as in the non-masked runs. So, in order to check the consistency and to give additional confirmation data, PMT1 data was analyzed even for the masked runs. The light yield of PMT1 in the masked runs was 9.4 p.e./keV. Fig.5.47 shows the relation between the rejection power and light yield.

In addition, the rejection power is estimated above 19 keV. Fig.5.48 shows the rejection power of the masked data (4.6p.e./keV) above 19keV. The mean value of the *PSDRatio* of nuclear recoils for each energy range is assumed constant (0.44) using the value for nuclear recoil at 14.4~19.1keV.

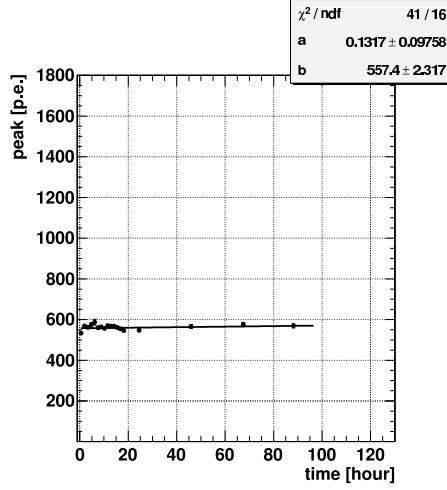


Figure 5.39: Time variation of the ^{57}Co data peak value of PMT2 during the masked run.

Energy(keV)	4.8~7.2	7.2~9.6	9.6~12	12~14.4	14.4~19.1
^{252}Cf masked PMT2	0.031±0.011	0.024±0.009	0.029±0.009	0.026±0.008	0.025±0.006
^{252}Cf non-masked PMT1+PMT2	0.024±0.003	0.021±0.002	0.021±0.002	0.015±0.003	0.016±0.002
^{137}Cs masked PMT2	0.015±0.017	0.031±0.007	0.034±0.005	0.028±0.005	0.030±0.002
^{137}Cs non-masked PMT1+2	0.034±0.003	0.028±0.003	0.033±0.003	0.028±0.002	0.031±0.001

Table 5.6: Estimation of the sigma of the unknown component in the unit of $PSDratio$ defined in Eq.(5.5).

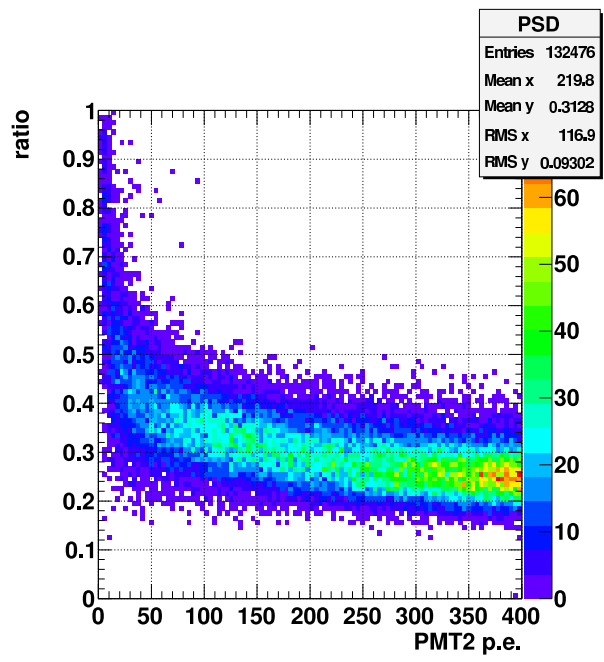


Figure 5.40: Scatter plot of detected p.e. vs. *PSDratio* for PMT2 in the ^{137}Cs data with mask (light yield of PMT2 was reduced to 4.6p.e./keV).

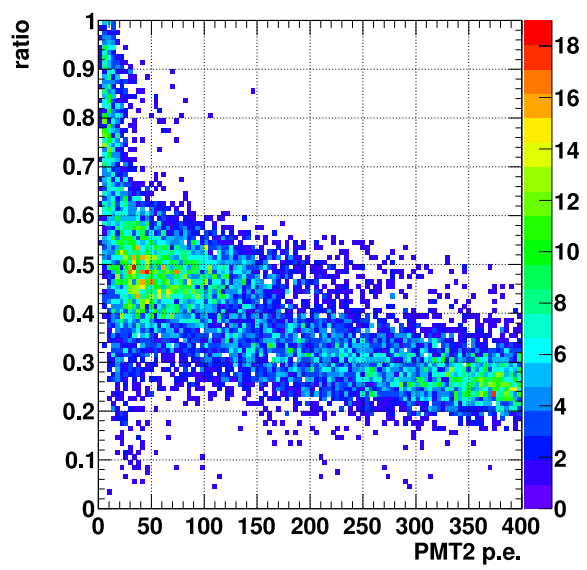


Figure 5.41: Scatter plot of detected p.e. vs. *PSDratio* for PMT2 in the ^{252}Cf data with mask (light yield of PMT2 was reduced to 4.6p.e./keV).

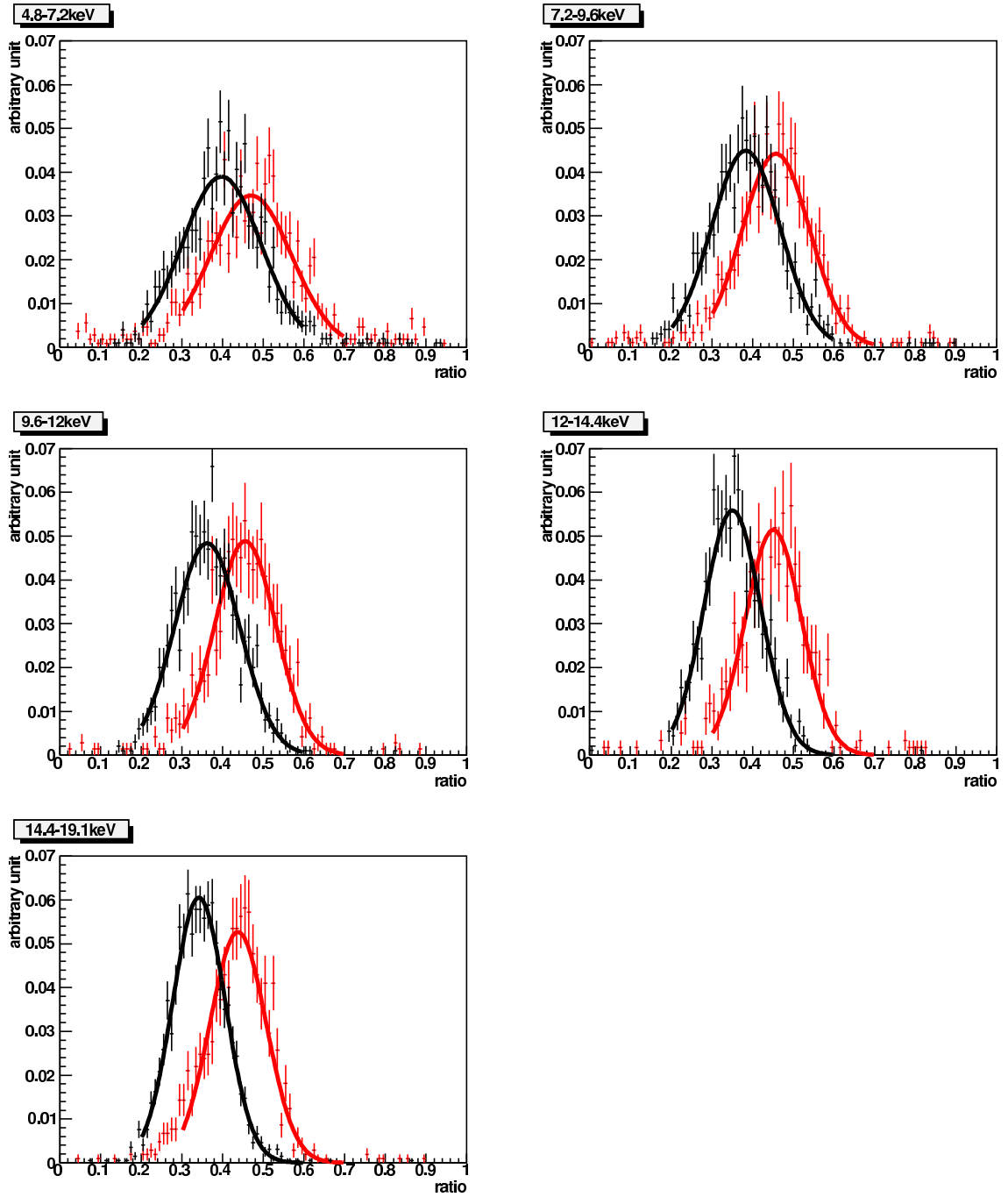


Figure 5.42: *PSDratio* distribution using the masked PMT2 data for each energy range (light yield was reduced to 4.6p.e./keV). The black and red line show the ^{137}Cs and the ^{252}Cf data, respectively.

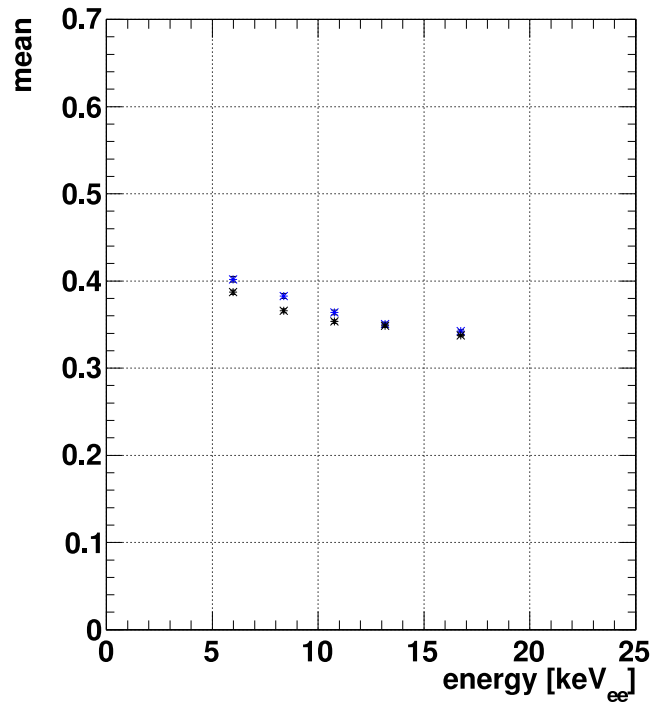


Figure 5.43: Mean value of the *PSDratio* as a function of observed energy in units of keV_{ee} for ¹³⁷Cs runs. The black and blue points show the values for the non-masked PMT1+PMT2 (20.9 p.e./keV) and for the masked PMT2 (4.6 p.e./keV), respectively.

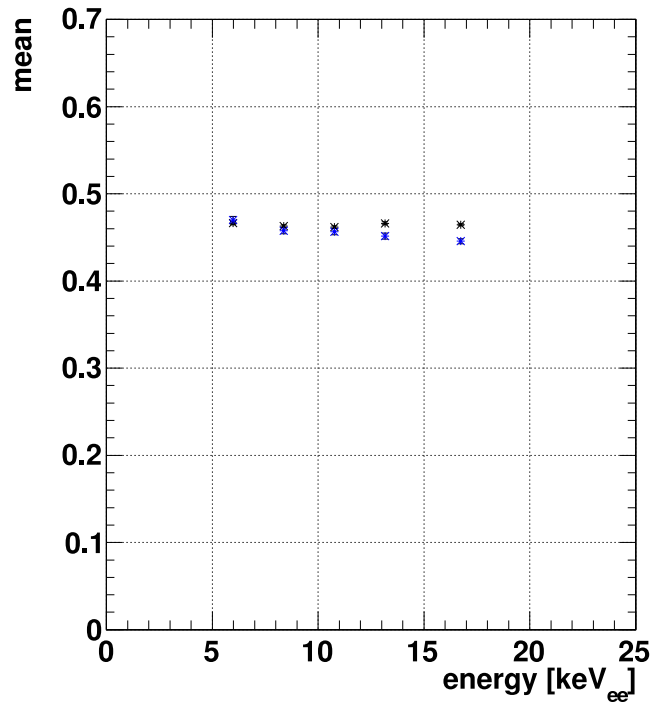


Figure 5.44: Mean value of the *PSDratio* as a function of observed energy in units of keV_{ee} for ^{252}Cf runs. The black and blue points show the values for the non-masked PMT1+PMT2 (20.9 p.e./keV) and for the masked PMT2 (4.6 p.e./keV), respectively.

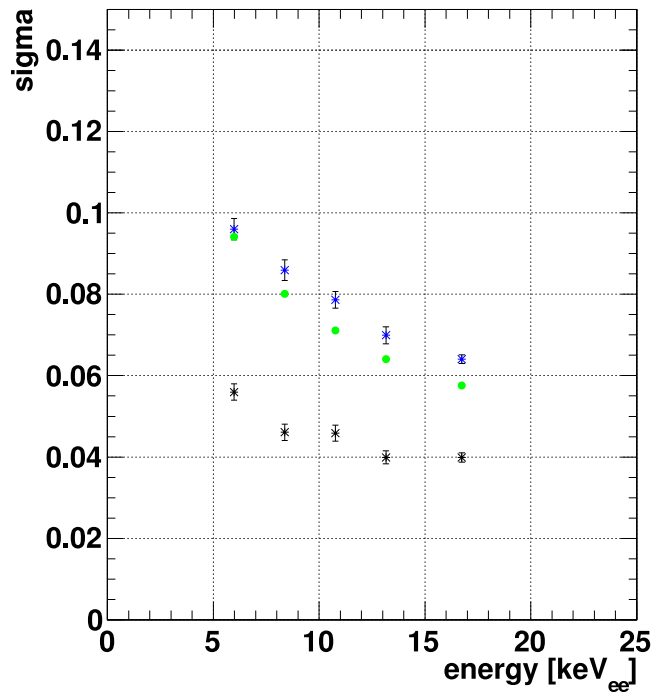


Figure 5.45: Sigma value of the *PSDratio* as a function of observed energy in unit of keV_{ee} for ^{137}Cs data. The black and blue points show the values for the non-masked PMT1+PMT2 data (20.9 p.e./keV) and for the masked PMT2 data (4.6 p.e./keV), respectively. The green points show the MC simulation of the masked PMT2 (light yield was reduced to 4.6p.e./keV).

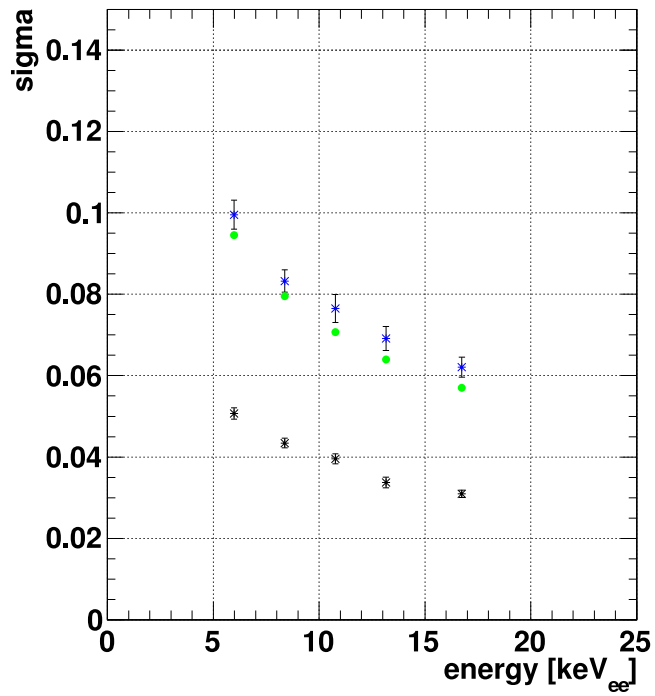


Figure 5.46: Sigma value of the *PSDratio* as a function of observed energy in unit of keV_{ee} for ^{252}Cf data. The black and blue points show the values for the non-masked PMT1+PMT2 (20.9 p.e./keV) and for the masked PMT2 (4.6 p.e./keV), respectively. The green points show the MC simulation of the masked PMT2 (light yield was 4.6p.e./keV).

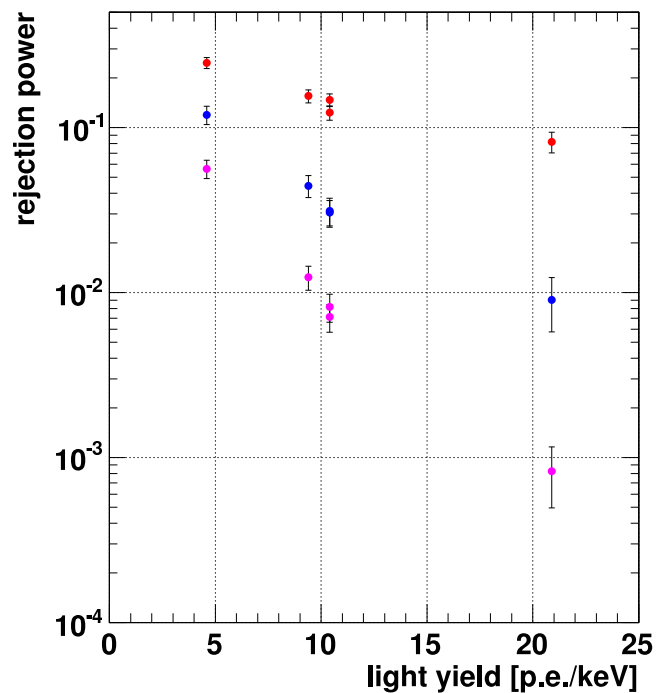


Figure 5.47: Rejection power as a function of light yield for several energy ranges. The rejection power is defined to be the fraction of remaining electron recoil events after the PSD cut to keep 50% of nuclear recoil events. The red, blue and pink points show the values for the 4.8~7.2keV, 9.6~12keV and 14.4~19.1keV energy ranges, respectively.

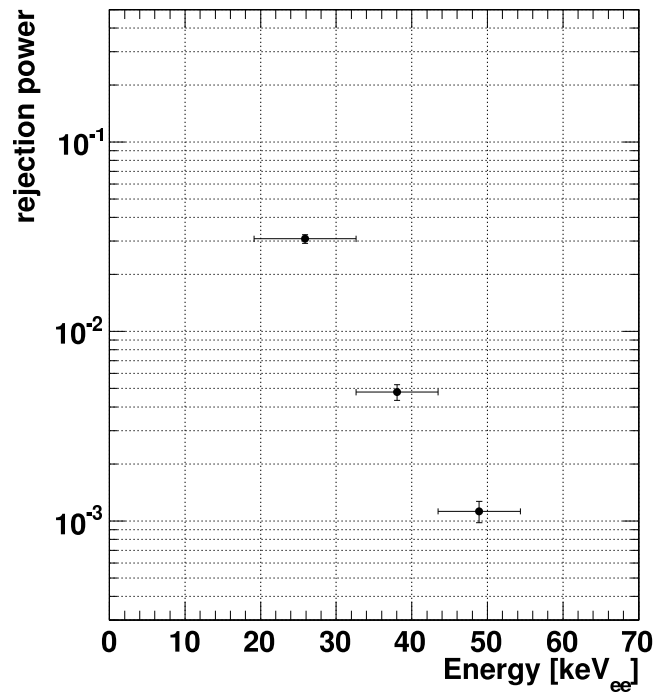


Figure 5.48: Rejection power as a function of energy larger than 19.1keV at low light yield (4.6p.e./keV), assuming the mean value of $PSDratio$ for nuclear recoil remains constant at 0.44 .

5.10 Decay time constant

In this section, the decay time constants of scintillation for nuclear recoil and electron recoil are estimated. Fig.5.49 shows the average waveform of the ^{252}Cf data and that of the ^{137}Cs data in the energy range of 4.8~7.2keV. This figure was made with the following steps.

- select events with an observed total p.e. which is in the given energy range.
- Search for the leading edge with the criterion described in section 5.5.1.
- Adjust the pulse starting time, and add the time corrected waveform for all selected events.

The maximum pulse height of ^{252}Cf is higher than that of ^{137}Cs . The average waveform was fitted by a single exponential function from 10% below maximum to 95% below maximum. Fig.5.50 shows the decay time of PMT1 and PMT2 for each energy range. The difference in decay times between PMT1 and PMT2 was treated as a systematic error. Fig.5.51 shows the decay time of the sum of PMT1 and PMT2 signal with systematic error and statistic error.

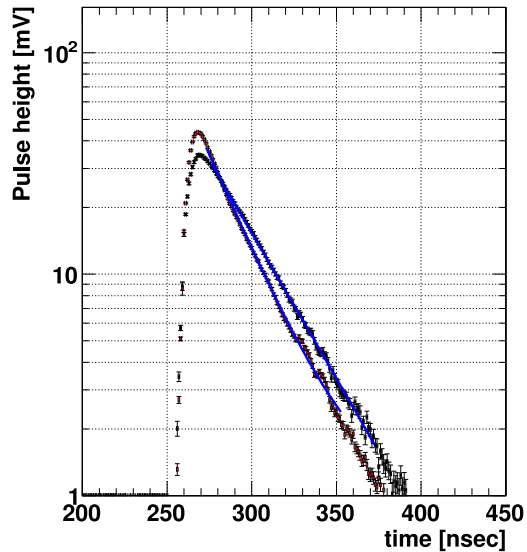


Figure 5.49: Average wave in the energy range of 4.8~7.2keV. The red and black points show the pulse of ^{252}Cf data and that of ^{137}Cs data. The blue lines show the fitted curve by a single exponential function.

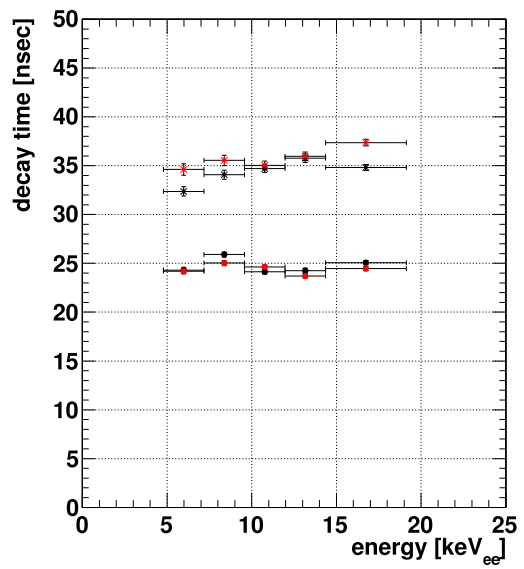


Figure 5.50: The decay time of the scintillation pulse as a function of the energy range. The closed circles and asterisks show the ²⁵²Cf and ¹³⁷Cs data for each energy range. Black and red show PMT1 and PMT2, respectively.

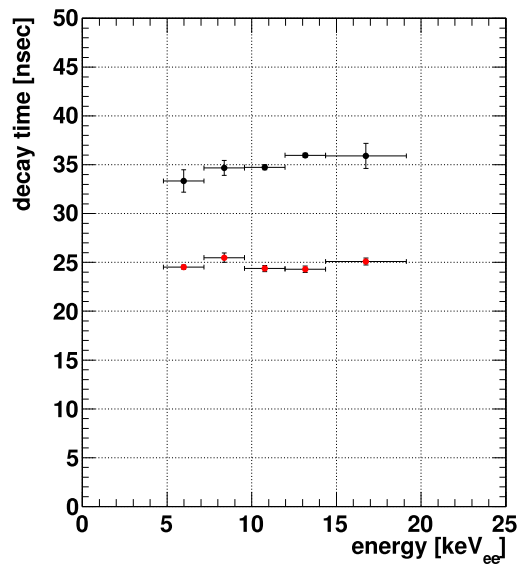


Figure 5.51: The decay time of the scintillation pulse as a function of the energy range. Red and black points show the ^{252}Cf and ^{137}Cs data for each energy range. The error bars include the fitted error and the differences of PMT1 and PMT2 in Fig.5.50 which was treated as a systematic error.

To remove the contamination of electron recoils, a selection cut was applied for electron recoil and nuclear recoil data. The events within $\pm 1\sigma$ of the mean value of PSD_{ratio} for each energy range were selected. Fig.5.52 shows the decay time of the sum of the PMT1 and PMT2 signals after the selection. Above 10keV, the decay time constant of nuclear recoil was decreased.

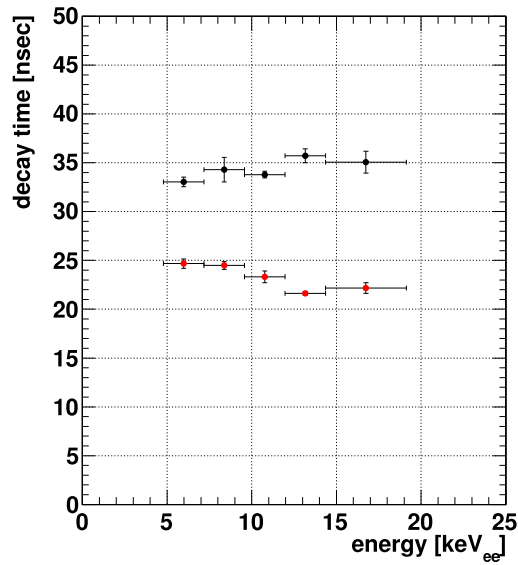


Figure 5.52: The decay time of scintillation pulse. The red and black points show the ^{252}Cf and ^{137}Cs data for each energy range after the selection cut.

5.11 Systematic error

An estimation of the systematic error of the PSD_{ratio} is described in this section. The parameters which are important for discriminating the nuclear/electron recoils are the the difference of the mean values (M_{diff}) of the PSD_{ratio} between nuclear recoil and electron recoil, and the sigma of the PSD_{ratio} of electron recoil ($\sigma_{e-recoil}$), because these two values are used for evaluating the significance of rejecting electron recoil background. Actually, the rejection power was calculated from M_{diff} and $\sigma_{e-recoil}$. The possible sources of the systematic errors of M_{diff} and $\sigma_{e-recoil}$ are listed as follows.

- Uncertainty of the energy scale
The gains of the PMTs are calibrated by the 1 p.e. distribution of an LED signal. The gain stability of the PMTs was estimated to be $\pm 6\%$ both for PMT1 and PMT2.
- Definition of the leading edge
The leading edge was defined as the point where the pulse crosses 112 counts which corresponds to 3 p.e. This crossing point was changed to 110 and 113 counts to estimate the effect of our leading edge definition.
- Position dependence in the detector
Although the chamber is small enough to study the PSD, there might be a slight position dependence of the PSD parameters. In order to estimate this effect, the effect of light balance was estimated. Fig.5.53 shows the light balance as a function of total p.e. The following balance cut was applied and the resulting change in PSD parameters was studied.

$$-0.3 < \frac{(PMT1p.e. - PMT2p.e.)}{Totalp.e.} < 0.3 \quad (5.9)$$

- Light yield uncertainty
The light yield was stable at $\sim 1\%$ /day at 122keV. Therefore for 4 days the influence of light yield and fraction was $\pm 2\%$. The light yield was shifted $\pm 2\%$ to estimate the systematic uncertainty due to changes in the light yield.

Energy(keV)	4.8~7.2	7.2~9.6	9.6~12	12~14.4	14.4~19.1
1p.e. +6%	+0.9%	+3.8%	+1.1%	-1.7%	+1.0%
1p.e -6%	+0.2%	-5.2%	-3.1%	-2.8%	-4.6%
leading edge 110	-5.8%	-4.8%	-3.8%	-4.7%	-2.5%
leading edge 113	-1.0%	-1.4%	-0.6%	-1.4%	-0.4%
light balance	-5.1%	-4.9%	-1.0%	-4.0%	-2.3%
light yield +2%	-0.9%	+2.1%	+0.4%	-1.1%	-0.7%
light yield -2%	+0.0%	-1.1%	-0.3%	-4.1%	-2.4%

Table 5.7: Systematic uncertainties for M_{diff} . The value shows the ratio for the measurement value.

Energy(keV)	4.8~7.2	7.2~9.6	9.6~12	12~14.4	14.4~19.1
1p.e. +6%	-2.2%	-4.7%	-2.1%	-1.0%	-2.6%
1p.e -6%	+4.2%	+0.5%	-1.3%	+1.6%	+0.6%
leading edge 110	-3.7%	+1.3%	-2.9%	+0.5%	-1.3%
leading edge 113	+1.2%	+3.2%	+0.6%	+1.4%	-1.0%
light balance	-3.3%	-3.0%	-5.0%	-0.8%	-1.5%
light yield +2%	-0.9%	-1.3%	-2.2%	+0.0%	-3.1%
light yield -2%	+2.8%	-0.5%	+3.6%	-1.5%	-0.8%

Table 5.8: The systematic uncertainties of the $\sigma_{e-recoil}$ of the *PSDratio* for ^{137}Cs . The value shows the ratio for the measurement value.

Energy(keV)	4.8~7.2	7.2~9.6	9.6~12	12~14.4	14.4~19.1
data	7.7×10^{-2}	1.8×10^{-2}	7.7×10^{-3}	1.6×10^{-3}	6.4×10^{-4}
1p.e. +6%	7.0×10^{-2}	1.1×10^{-2}	6.2×10^{-3}	1.7×10^{-3}	4.1×10^{-4}
1p.e -6%	8.4×10^{-2}	2.4×10^{-2}	8.7×10^{-3}	2.4×10^{-3}	1.1×10^{-3}
leading edge 110	8.1×10^{-2}	2.5×10^{-2}	8.2×10^{-3}	2.6×10^{-3}	7.3×10^{-4}
leading edge 113	8.1×10^{-2}	2.3×10^{-2}	8.4×10^{-3}	2.1×10^{-3}	7.4×10^{-4}
light balance	8.0×10^{-2}	2.0×10^{-2}	5.8×10^{-3}	2.2×10^{-3}	7.0×10^{-4}
light yield +2%	7.6×10^{-2}	1.5×10^{-2}	6.4×10^{-3}	1.8×10^{-3}	4.8×10^{-4}
light yield -2%	8.2×10^{-2}	1.9×10^{-2}	9.9×10^{-3}	1.9×10^{-3}	7.7×10^{-4}

Table 5.9: The rejection power for each systematic uncertainty.

Table 5.7 and Table 5.8 show the systematic uncertainties for M_{diff} and $\sigma_{e-recoil}$, respectively. In addition, Fig.5.54 and Fig.5.55 show the systematic uncertainties for M_{diff} and $\sigma_{e-recoil}$, respectively. Fig.5.56 shows how the rejection power is changed by changing each of the systematic uncertainties. The contribution from PMT gain is the main component to the overall systematic uncertainty. Fig.5.57 shows the rejection power distribution for masked and non-masked data including the systematic error. The numerical summary of the rejection power is shown below with the systematic errors:

- non-masked data (20.9p.e./keV)
 - 4.8~7.2keV : $7.7 \pm 1.1(\text{stat}) \pm 0.6(\text{sys}) \times 10^{-2}$
 - 7.2~9.6keV : $1.8 \pm 0.5(\text{stat}) \pm 0.8(\text{sys}) \times 10^{-2}$
 - 9.6~12keV : $7.7 \pm 2.8(\text{stat}) \pm 2.8(\text{sys}) \times 10^{-3}$
 - 12~14.4keV : $1.6 \pm 0.8(\text{stat}) \pm 0.6(\text{sys}) \times 10^{-3}$
 - 14.4~19.1keV : $6.4 \pm 2.6(\text{stat}) \pm 2.7(\text{sys}) \times 10^{-4}$
- masked data (4.6p.e./keV)
 - 4.8~7.2keV : $2.4 \pm 0.2(\text{stat}) \pm 0.3(\text{sys}) \times 10^{-1}$
 - 7.2~9.6keV : $1.8 \pm 0.2(\text{stat}) \pm 0.3(\text{sys}) \times 10^{-1}$

- 9.6~12keV : $1.2 \pm 0.1(\text{stat}) \pm_{0.2}^{0.1}(\text{sys}) \times 10^{-1}$
- 12~14.4keV : $6.6 \pm 1.0(\text{stat}) \pm_{0.0}^{2.0}(\text{sys}) \times 10^{-2}$
- 14.4~19.1keV : $6.2 \pm 0.7(\text{stat}) \pm_{1.3}^{1.0}(\text{sys}) \times 10^{-2}$

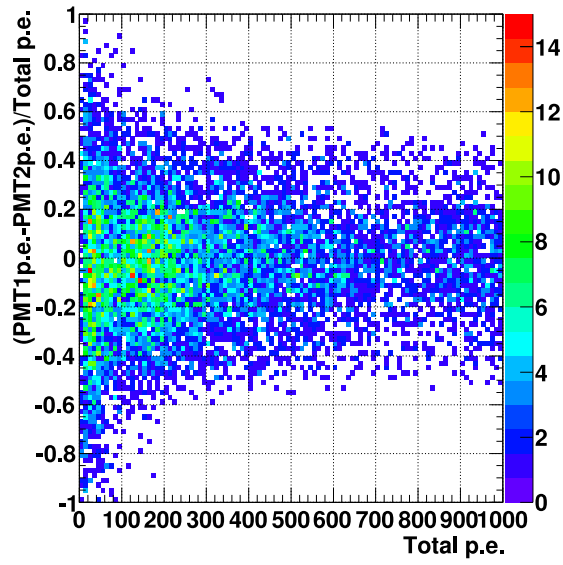


Figure 5.53: The light balance of the ^{252}Cf data as a function of total p.e. Horizontal axis and vertical axis show the total p.e. and $(\text{PMT1 p.e.}-\text{PMT2 p.e.})/\text{total p.e.}$

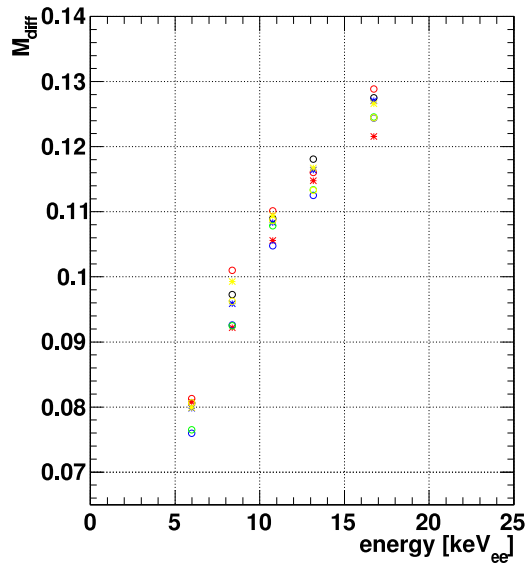


Figure 5.54: Effect of the systematic errors on M_{diff} (the difference of the mean value of the $PSDRatio$ between ^{137}Cs and ^{252}Cf). The black points show the measurement data. The red open circle and asterisk show the effect of a +6% and -6% PMT gain shift. The blue open circle and asterisk show the effect of a change in the leading edge definition to 110 and 113. The yellow open circle and asterisk show the effect of change in light yield by -2% and +2%. The green open circle shows the data with the additional light balance cut applied.

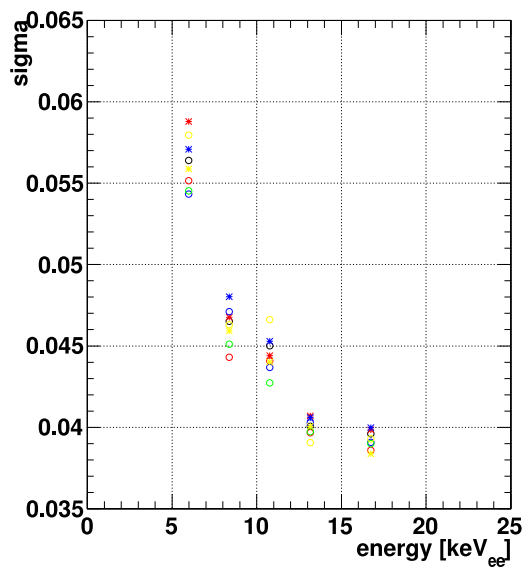


Figure 5.55: Effect of the systematic errors on $\sigma_{e-recoil}$ of the *PSDratio* distribution for ^{137}Cs . The black points show the measurement data. The red open circle and asterisk show the effect of a +6% and -6% PMT gain shift. The blue open circle and asterisk show the effect of a change in the leading edge definition to 110 and 113. The yellow open circle and asterisk show the effect of change in light yield by -2% and +2%. The green open circle shows the data with the additional light balance cut applied.

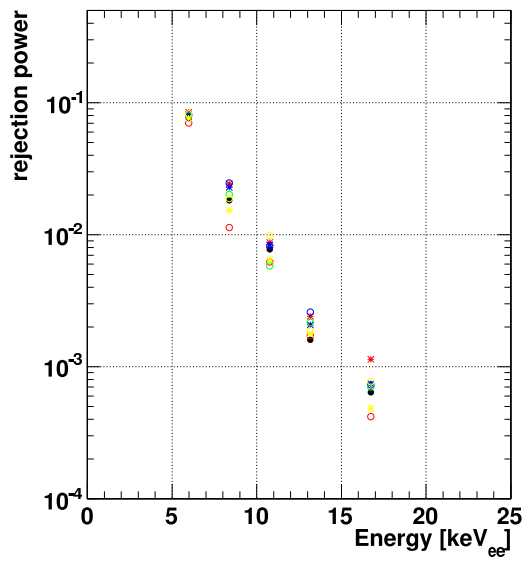


Figure 5.56: The rejection power for each systematic uncertainty. The black points show the measurement data. The red open circle and asterisk show the effect of a +6% and -6% PMT gain shift. The blue open circle and asterisk show the effect of a change in the leading edge definition to 110 and 113. The yellow open circle and asterisk show the effect of change in light yield by -2% and +2%. The green open circle shows the data with the additional light balance cut applied.

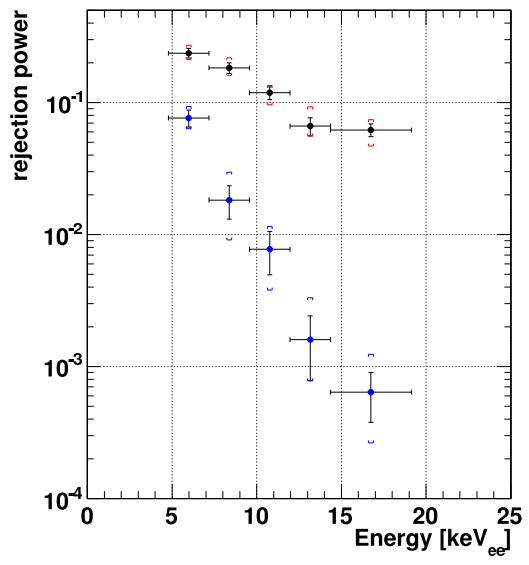


Figure 5.57: The rejection power distribution. Black and blue point show the masked(4.6p.e./keV) and non-masked (20.9p.e./keV) data. Black error bars shows the statistical error. Red and blue braces show the error including systematic uncertainty added in quadrature.

Chapter 6

Discussion

In this chapter, the results of the pulse shape measurements are compared with other reported measurements. In addition, the expected impact of PSD on the XMASS experiment is discussed.

6.1 Comparison with other measurements

PSD of liquid xenon was studied by several experimental groups. The results described in the previous chapter are compared with these other studies.

6.1.1 Comparison with ZEPLIN

As described in section 3.6.1, ZEPLIN used average scintillation time τ_m between 90% and 5% of the pulse height. In order to directly compare with the ZEPLIN results, we have re-analyzed our data using the same analysis method as that of ZEPLIN. Fig.6.1 shows a typical signal in our data. Using the low light yield data, the τ_m distributions for nuclear recoil events and electron recoil events are made as shown in Fig.6.2.

Fig.6.3 shows the comparison of the τ_m with ZEPLIN data. The black, red and blue points show the ZEPLIN result of neutron run at 3~8 keV, neutron data in this thesis at 4.8~7.2 keV and gamma ray data in this thesis at 4.8~7.2 keV.

The ZEPLIN argued that the tail events around 10 nsec are nuclear recoil events. However, our measurement gave much larger τ_m .

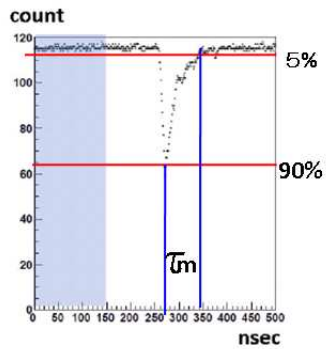


Figure 6.1: The definition of τ_m .

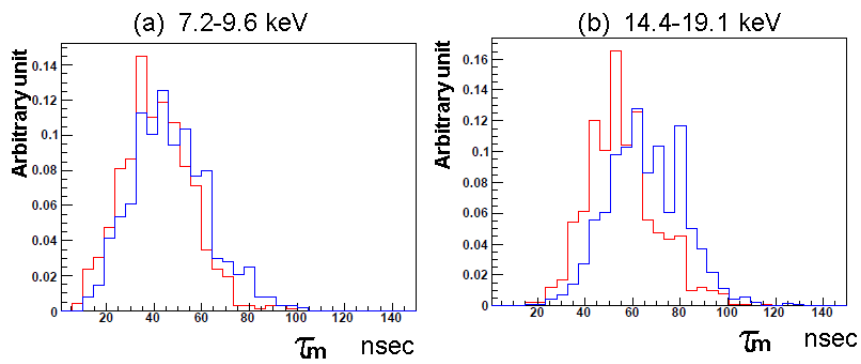


Figure 6.2: The τ_m distribution of our data. Blue and red lines show the gamma ray data and the neutron data, respectively. (a) and (b) show the energy range of 7.2~9.6 keV and that of 14.4~19.1 keV, respectively.

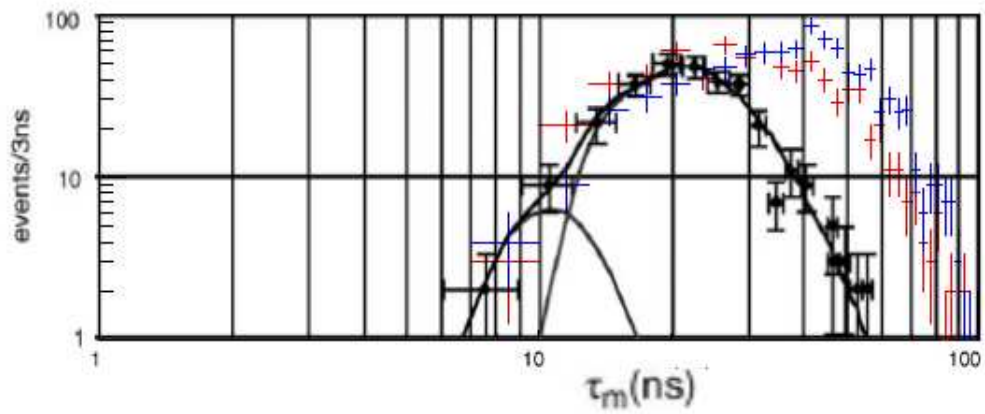


Figure 6.3: τ_m distribution. The black, red and blue points show the ZEPLIN result of neutron run at 3~8 keV, neutron data in this thesis at 4.8~7.2 keV and gamma ray data in this thesis at 4.8~7.2 keV, respectively.

6.1.2 Decay time constant

The decay time constants of liquid xenon for electron recoil and neutron recoil events were measured by D.Akimov [68] as shown in Fig.6.4. This figure also includes our measurement. The light yield of his measurement setup was 0.9 ± 0.02 p.e./keV.

The decay time constant measured by D.Akimov was 21.0 ± 0.5 nsec for nuclear recoil events with an energy from 6keV_{ee} to 30keV_{ee} . The decay time for electron recoil was 29.1 ± 0.6 nsec for electron recoil events at $\sim 13.5\text{keV}$. On the other hand, results from our measurements show that the decay time for nuclear recoils and electron recoils are 23.3 ± 0.6 nsec and 33.8 ± 0.3 nsec at $9.6 \sim 12\text{keV}$, respectively.

The decay time measurements for electron recoil events made by D.Akimov and ours are not consistent with each other. Our measured value is significantly longer than D.Akimov's measurements. Scintillation light from recombination in electron recoils is decreased by impurities in liquid xenon. A decrease in recombination makes the time constant smaller. As for D.Akimov's measurements, the light yield was very small even though their setup configuration was similar to ours. Therefore, impurities in D.Akimov's setup might be the cause of the difference.

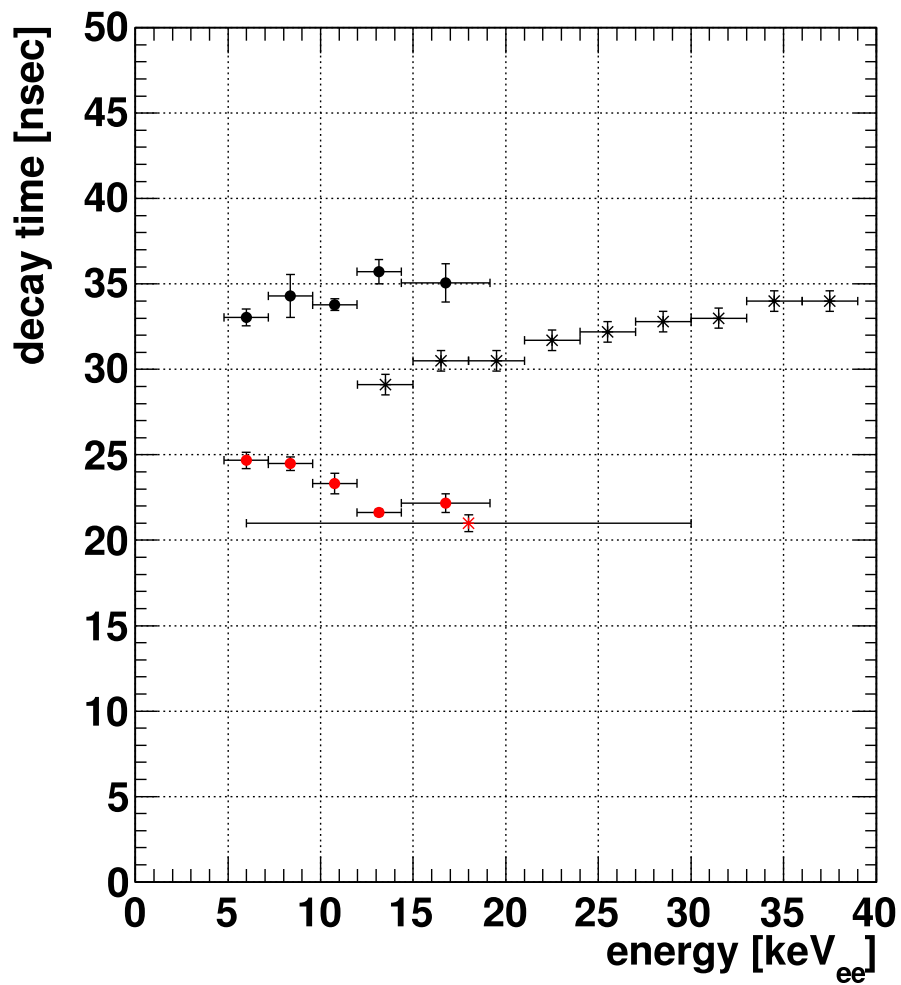


Figure 6.4: The decay time constant as a function of energy. The asterisks and circle points show D.Akimov's result and our result. Black and red show the electron recoil and nuclear recoil events, respectively. Vertical error bars correspond to total errors obtained by adding statistical and systematic errors in quadrature. The nuclear recoil point of D.Akimov corresponds to all events in the electron equivalent energy range from 6keV to 30keV [68].

6.1.3 PSD using double phase detector

A PSD analysis using a double phase detector was reported by LUX group [44]. The detector consisted of a gas and a liquid phase using two PMTs as shown in Fig.3.12. The light yield was obtained to be ~ 5 p.e./keV from a ^{57}Co source (122keV) measurement at zero electric field. The PSD analysis was performed using the ratio of prompt and total signal at a drift electric field of 0.06kV/cm.

Fig.6.5 shows the result of their PSD analysis. The rejection power that they measures is between that obtained at our low light yield (4.6p.e/keV) and high light yield data as shown in the Fig.6.5. The rejection power was better than our low light yield data. LUX group used two Hamamatsu PMTs (R9288 and R6041) whose transit time spread (TTS) was 750 psec (FWHM). On the other hand, TTS of our PMTs (R10789) is 4nsec (FWHM). However, the difference in the rejection power can not be explained by the timing resolution of the PMTs because the time resolution of those PMTs is much smaller than the time constant discussed here.

One possible reason for the difference is the energy scale of electron recoil events. As described in section 3.6, the light yield of electron recoil events critically depends on the applied electric field. On the other hand, the light yield of nuclear recoil events is stable even though the electric field is changed. Fig.6.6 shows the field dependence of scintillation yield in liquid xenon for 122keV gamma-ray and nuclear recoils with 56.5 keV_r [70]. The scintillation yield of electron recoils is shifted drastically at low electric field. At the electric field adopted by LUX measurement (0.06 kV/cm), the light yield of electron recoil is decreased by about 10% at 122keV. As shown in Table.6.1, even though the detected number of p.e. is same for all data set, the energy scale of electron recoil events for LUX data was $\sim 10\%$ higher than the other case. This difference in energy scale might have given slightly better PSD performance in the LUX data.

	number of p.e.	energy at zero field (keV _{ee})
LUX nuclear recoil	100	20
LUX electron recoil	100	22
our nuclear recoil	100	20
our electron recoil	100	20

Table 6.1: The relation between number of observed p.e. and energy at zero field.

Another possible reason for the difference is the fluctuation of recombination process caused by the character of the track. As described in section 5.9, the spread of *PSDratio* of electron recoils is larger than that of estimated from photon statistics, which was expressed by the $\sigma_{unknown}$ component. The most plausible source of the $\sigma_{unknown}$ component is the fluctuation of the electron thermalization before recombination. If this is true, the $\sigma_{unknown}$ component of electron recoils might be reduced by the electric field. A reduced $\sigma_{unknown}$ could have improved the rejection power in the measurement of LUX.

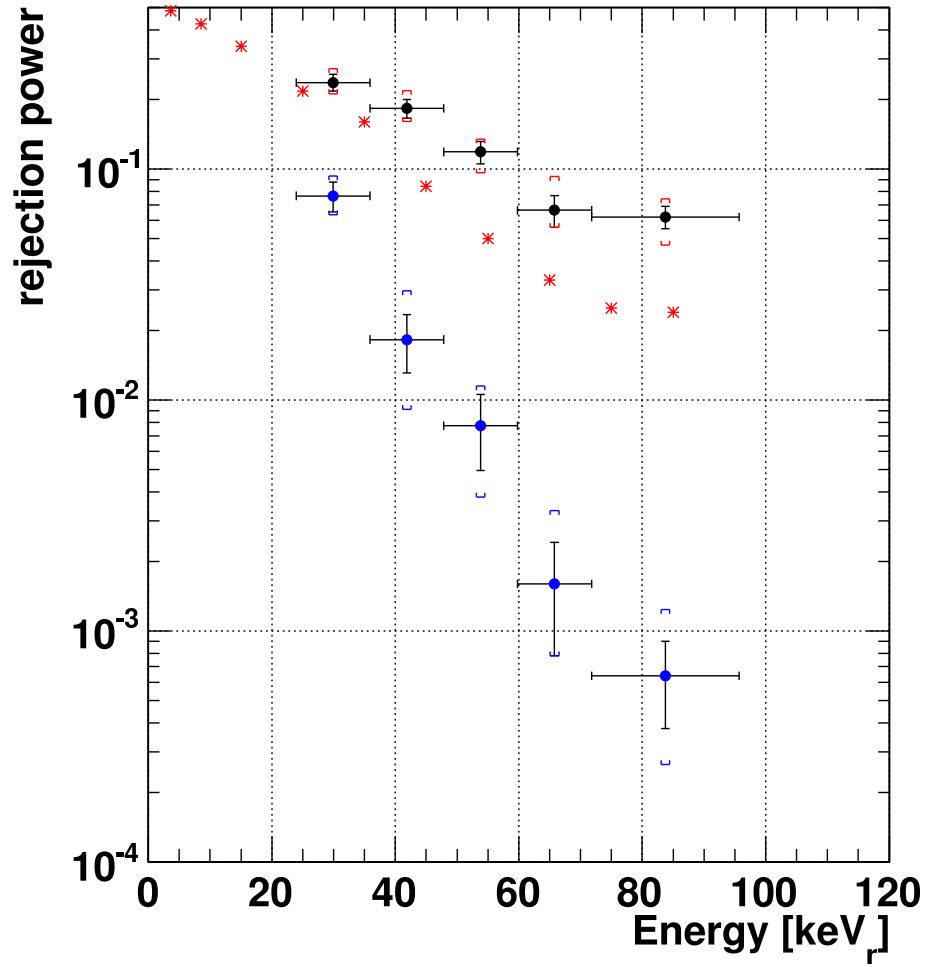


Figure 6.5: The rejection power as a function of recoil energy. The L_{eff} was assumed 0.2. The red asterisk is the data set taken at a drift electric field of 0.06kV/cm [44]. The circle points are our measurements. The black and blue points show the data obtained at low light yield(4.6p.e./keV) and that obtained at high light yield (20.9p.e./keV) respectively.

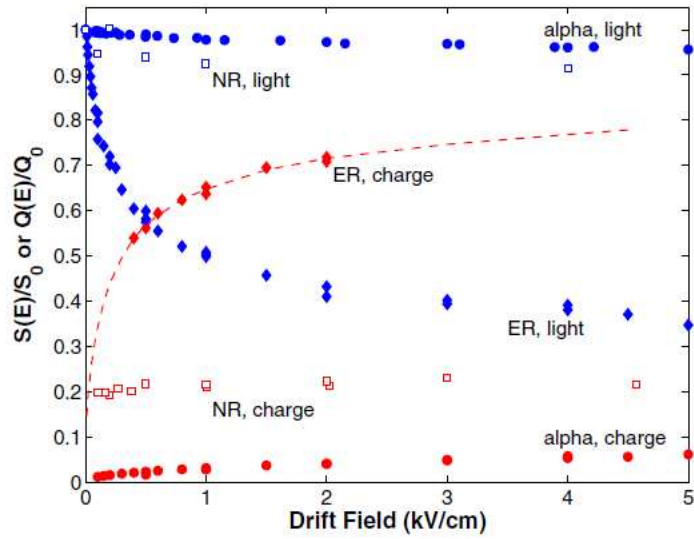


Figure 6.6: Field dependence of scintillation and ionization yield in liquid xenon for 122 keV electron recoils (ER), 56.5 keV_r nuclear recoils and alphas [70]. The relative scintillation yield, $S(E)/S_0$, is the ratio of scintillation yield at a given field, E , to that at zero field. The relative charge yield, $Q(E)/Q_0$, is the ratio of charge yield at a given field, E , to that at infinite field (i.e. with no recombination).

6.1.4 Comparison with S_2/S_1 method

The rejection power of our PSD is compared with the BG rejection method of a double phase detector such as the XENON10 detector shown in Fig.6.7. The method of BG rejection for XENON10 uses the ratio between primary scintillation (S1) and proportional scintillation (S2) caused by the electron which has drifted from liquid to gas phase.

Fig.6.8 shows the distribution of $\Delta\text{Log}_{10}(S_2/S_1)$ at 13.4-17.2keV recoil energy. Fig.6.9 shows the rejection power as a function of S1 energy. Below 5keV_{ee} the rejection power reaches 3 orders of magnitude. However, the rejection power above 10keV_{ee} is about two orders of magnitude. Hence, the rejection power of PSD method studied in this thesis is as good as S_2/S_1 method above 10keV_{ee} .

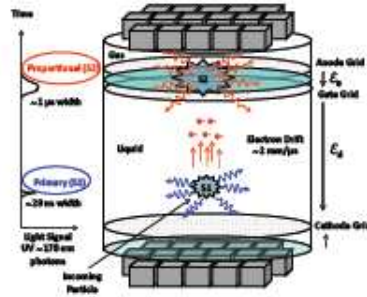


Figure 6.7: The schematic view of the XENON10 detector [54]. A particle interaction in the liquid produces primary scintillation light (S1) and ionization electrons. The electrons drift under an electric field (ϵ_d 1kV/cm) out of the liquid phase. The electrons reaching the gas phase are accelerated by a stronger electric field (ϵ_e 10kV/cm) and proportional scintillation light (S2) is produced.

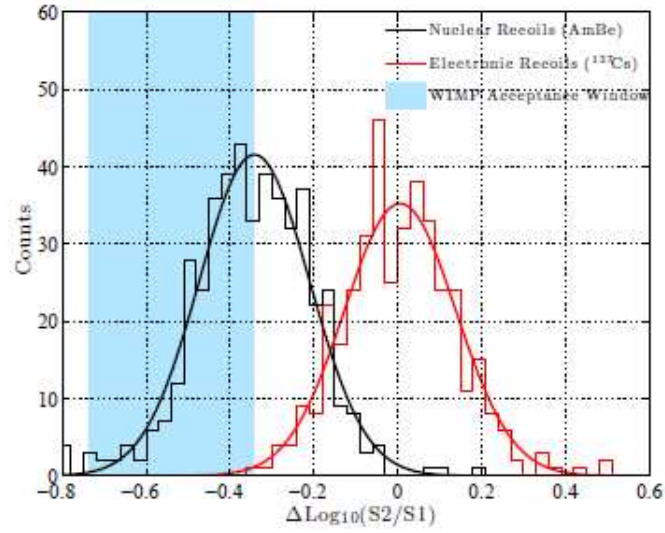


Figure 6.8: The distribution of $\Delta \text{Log}_{10}(S2/S1)$ for electron (red) and nuclear (black) recoil events at 13.4-17.2keV recoil energy. The blue region is their WIMP acceptance window [54].

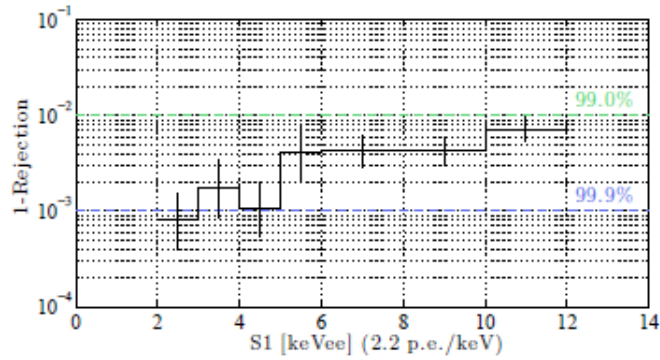


Figure 6.9: The rejection power as a function of $S1$ with 50% efficiency for nuclear recoil events in the XENON10 double phase detector [54].

6.1.5 Summary and value of PSD study in this thesis

In this thesis, PSD of liquid xenon was studied at the energy relevant for dark matter searches with much higher sensitivity than previous experiments. A difference of pulse shape between the nuclear recoil and electron recoil events was observed using a high light yield setup in which 5 keV corresponds to 100 p.e.

As a result of the PSD study in this thesis, we have determined that PSD can be used for the event selection in dark matter searches. The most optimal parameter for the PSD is the ratio of the prompt 20 nsec signal to the wider 200 nsec signal (*PSDratio*). One of the most distinct features of this thesis is that the *PSDratio* was measured not only for the modest light yield which is obtained in the usual detector setup but also for extremely high light yield. This feature revealed the fundamental behavior of the *PSDratio*. The results of this thesis show that the *PSDratio* is independent of light yield and the spread of the *PSDratio* consists of a term for photon statistics and a term that is independent of photon statistics.

The general results obtained in this thesis can be applied not only to current experiments but also to future experiments which may have much higher light yield.

6.2 PSD for the XMASS experiment

In this section, the advantages of PSD for the XMASS experiment are described. As mentioned in section 4.2.7, there is a possibility that events which are misreconstructed due to the wall effect can be reduced using PSD. In the first half of this section, the BG reduction using PSD in the XMASS experiment is estimated using MC simulations with the statistics of 1 year equivalent and 100 kg fiducial volume. In addition, the usefulness of PSD for understanding other BG sources is also discussed. Finally, the advantage of using PSD in the inelastic dark matter search is also described.

6.2.1 Effect of time of flight

In the case of a large detector, the time of flight (TOF) of scintillation light may not be negligible. Here, TOF means the time between the emission time of scintillation light and the detection time by a PMT in the detector. So, TOF depends on the location of the PMT. The effect of TOF is established following steps using MC simulation of the XMASS detector.

- step1: Many photons are generated at 9 points in the XMASS detector whose radii are from 0 cm to 40 cm at every 5 cm. The probability distribution of TOF is calculated for each point.
- step2: The waveform of all events at low light yield is corrected using the nine probability distributions of the TOF randomly as shown in Fig.6.10.
- step3: The same analysis in section 5.6 is performed after the TOF correction.

Fig.6.11 shows the rejection power with and without the TOF correction. It shows that the difference is within statistical error and the TOF effect in the XMASS detector is negligible.

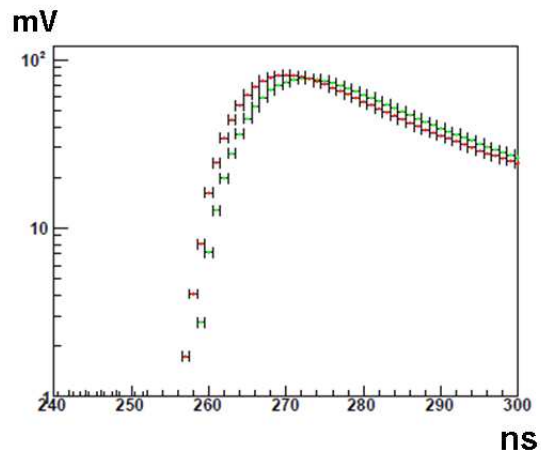


Figure 6.10: Red and green points show the waveform without and with TOF correction, respectively.

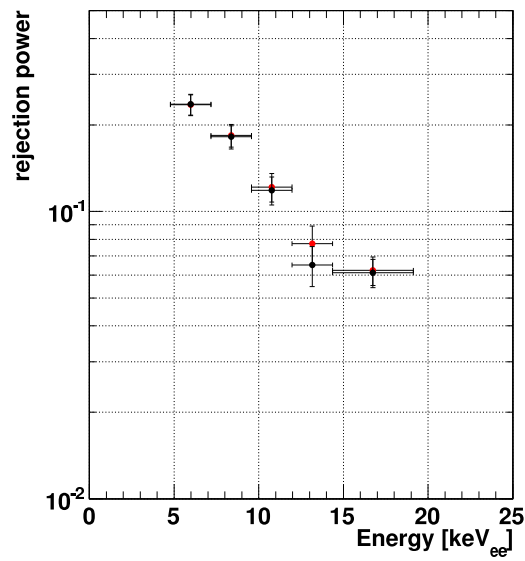


Figure 6.11: The effect of TOF. Black and red points show the rejection power without TOF correction and with TOF correction, respectively.

6.2.2 The advantage of PSD for the XMASS experiment

As discussed in chapter 4, the XMASS detector has 4.6p.e./keV if the attenuation length is assumed to be 100cm. Since vertex reconstruction is the essential for the background reduction in this experiment, a good position resolution is needed. The XMASS group assumes 5keV_{ee} for their analysis threshold. In addition to this, according to Fig.A.5, dark matter signals are expected to appear below 20keV_{ee}. Because of those reasons, discussion in this section is limited to the range within 5keV_{ee} to 20keV_{ee} in the reconstructed energy.

Before beginning the discussion about PSD for the BG, it is important to explain the origin of the background in the energy of interest. The main BG of the XMASS experiment comes from ²³⁸U, ²³²Th, ⁶⁰Co and ⁴⁰K in PMTs. Using the fiducial volume cut, many BG events below 100keV are decreased by the self-shielding. However, some events near the wall are reconstructed as occurring in the center, called wall effect.

Fig.6.12 shows the relation between reconstructed vertex and true vertex for the events with the reconstructed energy below 20keV and with the reconstructed vertex position within 20cm from the center. The true vertices of most events are more than 40cm from the center.

Fig.6.13 shows the relation between reconstructed energy and true deposited energy in liquid xenon. For most events the true energy is a factor of 2 larger than the reconstructed energy. Because the position of the generated event is very close to the wall, which is made from copper whose reflectance is ~10%, the scintillation light reduced to approximately cut in half.

In order to evaluate the impact of the PSD for the BG reduction, the *PSDratio* for true energy is used and "the *sigma*" of each event is also calculated, using the following equation.

$$sigma = \sqrt{\sigma_{unknown}^2 + \frac{PSDratio \times (1 - PSDratio)}{TotalPE}}, \quad (6.1)$$

where the $\sigma_{unknown}^2$ is shown in section 5.9. The *sigma* is estimated using $\sigma_{unknown}^2$ and binominal statistics.

Fig.6.14 shows the remaining BG spectrum after the 20cm fiducial cut. The black points show the BG events for 1 year equivalent statistics in the 100kg fiducial volume assuming the radioactivity of PMT. The red points show the remaining events after the PSD is applied. As shown in Table 6.2, the BG events was reduced to 5.7 events using PSD for events with energy between 5 keV and 15 keV.

	²³⁸ U	²³² Th	⁶⁰ Co	⁴⁰ K	Total
BG	24	40	25	3	92
remaining event after PSD	1.47	2.27	1.73	0.23	5.70

Table 6.2: The BG events and the remaining events with the energy between 5keV and 15keV after the rejection of PSD.

Therefore the BG events are reduced to below 10% using PSD with 50% efficiency for nuclear recoil events.

The sensitivity to dark matter interactions is calculated using Eq.(A.10), (A.23), (A.31), (A.37), (A.38), and assuming the relative scintillation efficiency (L_{eff}) is 0.2. The relationship among nuclear recoil energy E_R , WIMP mass M_χ , and cross section σ_0 is expressed the following equation,

$$N_{90\%} = 100kg \ 365days \frac{361}{M_N M_\chi} \left(\frac{\rho_D}{0.3 \text{ GeV } c^{-2} \text{ cm}^{-3}} \right) \left(\frac{v_0}{230 \text{ km } s^{-1}} \right) \left(\frac{\sigma_0}{1 \text{ pb}} \right) \left(\frac{\mu_{\chi-N}^2}{\mu_{\chi-p}^2} \right) A^2 \\ \times \int_{25keV_r}^{75keV_r} \left[\frac{3j_1(\sqrt{2M_N E_R} r_n)}{\sqrt{2M_N E_R} r_n} \right]^2 \exp(-2M_N E_R s^2) c_1 \exp(-c_2 E_R / (E_0 r)) dE_R,$$

where $N_{90\%}$ is the number of required dark matter events (Table 6.2), $\rho_D = 0.3 \text{ GeV } c^{-2} \text{ cm}^{-3}$ is the local halo density, $v_0 = 230 \text{ km/sec}$, $\mu_{\chi-N}$ is the reduced mass of the neutralino and the target nucleus, A is the mass number, r_n is the effective nuclear radius, s is the nuclear skin thickness, $c_1 = 0.751$ and $c_2 = 0.561$. More detail is shown in Appendix A.

Fig.6.15 shows the sensitivity plot at 90% C.L using the energy range between 5 keV_{ee} and 15 keV_{ee} (between 25 keV_r and 75 keV_r). Many previous experiments of dark matter search didn't subtract the BG and reported the sensitivity at 90% C.L. Therefore the sensitivity of dark matter without BG subtraction is shown in Fig.6.15. Using the PSD the sensitivity is greatly improved. The sensitivity is improved to $5.6 \times 10^{-45} \text{ cm}^2$ from $2.9 \times 10^{-44} \text{ cm}^2$ using PSD at $M_\chi = 100 \text{ GeV}$.

In addition, the PSD may give additional information about the purity of liquid xenon. The purity of liquid xenon is important for XMASS experiment. As described in section 4.2.5, the circulation system of liquid xenon to purify liquid xenon is developed. In the case of liquid argon, the pulse shape is very depend on the impurity in the liquid argon such as nitrogen and oxygen [69]. As reported by [69], the decreasing behavior of the scintillation light caused by electron recoil events was observed from ~ 1 ppm nitrogen concentrations and from ~ 0.1 ppm oxygen concentrations. Using the *PSDRatio* of electron recoil events, the information of purity in liquid xenon may be obtained because the pulse shape of electron recoil events especially may change like liquid argon.

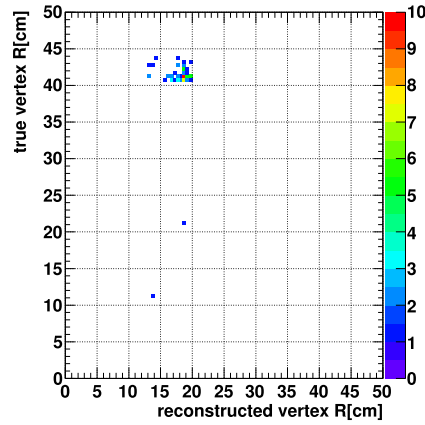


Figure 6.12: The relation between reconstructed vertex and true vertex in liquid xenon after selecting events which are reconstructed within 20cm from the center and below 20keV_{ee} , i.e. MC events that are clearly mis-reconstructed.

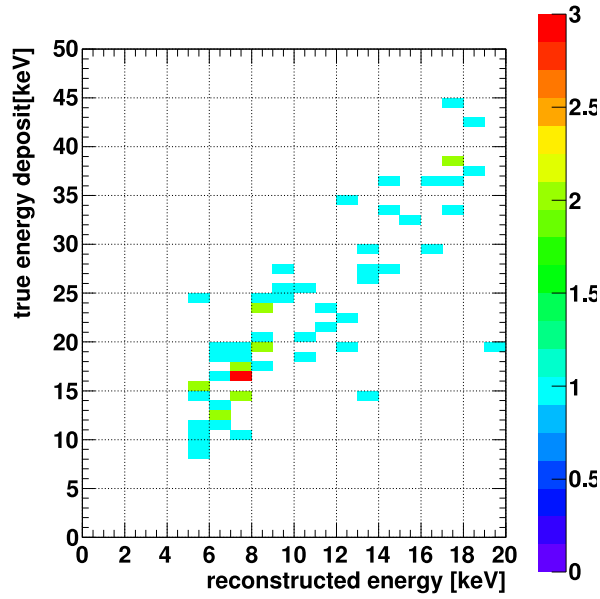


Figure 6.13: The relation between reconstructed energy and true deposited energy in liquid xenon after selecting MC events which are reconstructed within 20cm from the center and reconstructed energy below 20keV_{ee} .

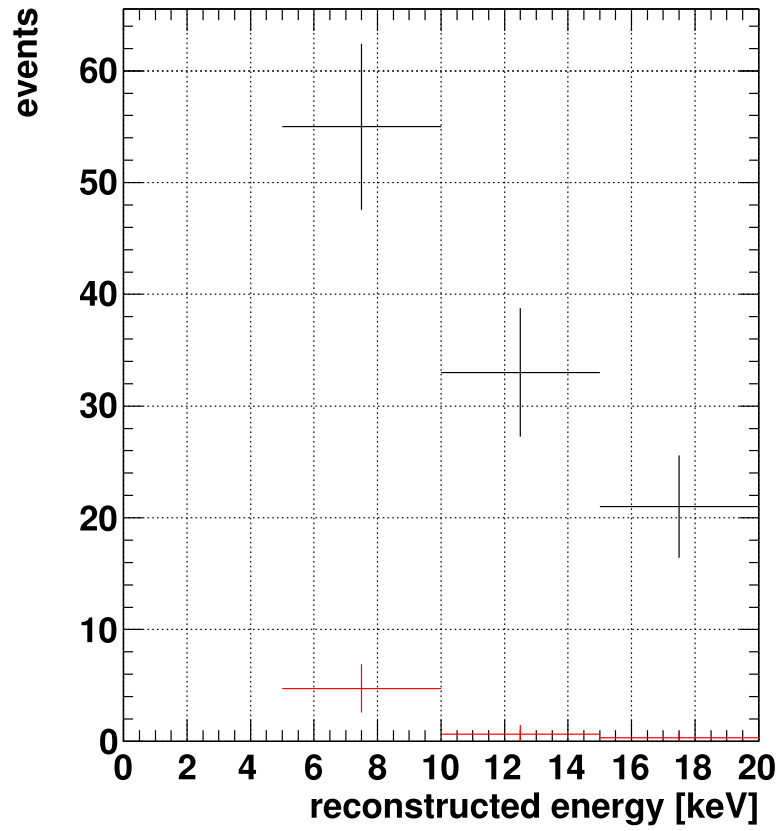


Figure 6.14: The BG spectrum of 1 year equivalent after the 20cm fiducial cut. The black point shows the BG events. The red point shows the remaining events after the rejection of PSD.

- XENON10 2007 New (Net 136 kg-d)
 - CDMS: Soudan 2004–2009 Ge
 - X X X Linear Collider Cosmology Benchmarks (preliminary)
 - Roszkowski/Ruiz de Austri/Trotta 2007, CMSSM Markov Chain Monte Carlos
 - Ellis et. al 2005 CMSSM ($\mu > 0$, pion $\Sigma = 64$ MeV)
- 100811001101

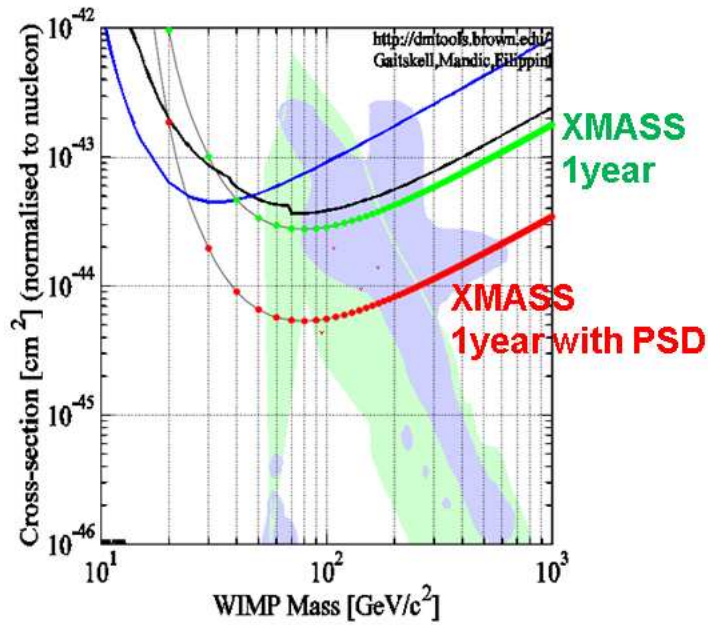


Figure 6.15: The sensitivity plot of dark matter with 90% C.L without BG subtraction. The green line shows the sensitivity of XMASS for 1 year. The red line shows the sensitivity using PSD.

There might be other BG sources which should be identified and removed during the course of the experiment. For this purpose, PSD could contribute to many of these as described below.

- Rn: Rn is a noble gas and emanates from the materials. ^{222}Rn originates from the ^{238}U decay chain and ^{220}Rn from the ^{232}Th decay chain are radioactive isotopes. BG events caused by the Bi-Po decay which exists as the downstream radioactive decay of Rn are reduced using timing analysis.

However, radioactive nuclei with long lifetimes, such as ^{214}Pb and ^{212}Pb are difficult to identify. Both ^{214}Pb and ^{212}Pb cause β decay with high Q value. These β decays cause electron recoils and PSD is useful to reduce this BG in the signal window.

- ^{85}Kr : Kr is reduced using distillation below 1ppt. Events from the decay of the remaining Kr can be reduced using PSD, since the decay of ^{85}Kr is a β decay.
- Daughters of the U/Th chain in the surface of the wall: Some heavy nuclei of U/Th chain cause α decays. The nuclei have recoil energy $\sim 100\text{keV}$ after α decay. If an α particle goes into wall and nucleus with 100keV kinetic energy goes into liquid xenon, the pulses of those events are similar to the nuclear recoil event.

In addition if an α particle goes into the interspace of the detector, the pulses of those events are similar to the nuclear recoil event. Therefore the reduction of those events is difficult to separate using PSD. However, PSD is useful for estimating the number of such daughter nuclei on the wall.

- Fast neutron: Fast neutrons recoil xenon nuclei as dark matter particles do and thus cannot be distinguished. However, neutron induced events often have multiple nuclear recoils for each neutron in liquid xenon because the volume of liquid xenon is large. There is a possibility to reduce this BG by looking for multiple recoils [71].
- Internal radioactive contamination such as Tritium: Tritium causes β decays with a Q value of 18.6keV. PSD is useful to reduce BG caused by Tritium.

6.2.3 Inelastic dark matter

According to the model of inelastic interactions of dark matter in [72], a suppression of low energy nuclear recoil events is predicted. As shown in Fig.6.16, there is a peak caused by the inelastic scattering signal at around 40keV recoil energy.

The suppression peak depends on the value of the mass difference between the second excited and the ground states of dark matter particle. Assuming the L_{eff} is 0.2 for 40keV recoil energy, the visible energy is 10keV_{ee} . In this energy range the rejection power of PSD is 1 order of magnitude even at low light yield (4.6p.e./keV). The XMASS detector with PSD capability has a very good sensitivity for the inelastic dark matter search.

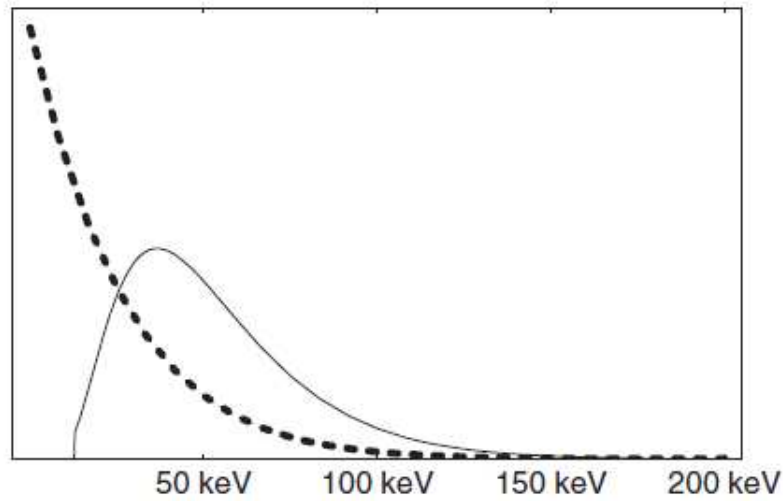


Figure 6.16: The expected spectrum of inelastic (solid line) and elastic (dashed line) events in a germanium assuming a WIMP mass of $M_\chi = 100\text{GeV}$ and a mass difference is 80keV . Horizontal axis shows the recoil energy [72].

Chapter 7

Conclusion

Low background techniques and pulse shape discrimination(PSD) for a liquid xenon dark matter detector were studied in this thesis.

As the first phase of the XMASS experiment, a 1 ton liquid xenon detector was developed to search for dark matter. The energy deposition by dark matter interactions in xenon is expected to be in the few keV to tens of keV range. Liquid xenon is useful to search for dark matter because of its large scintillation yield, about 46000 photons/MeV. The key idea behind the XMASS experiment is background (BG) reduction using the self-shielding of liquid xenon. Since the atomic number of xenon is large ($Z = 54$), almost all gamma rays and β rays are attenuated at the edge of the detector. In order to reduce the BG, the fiducial volume used to search for dark matter is within the center of the detector and its extent is determined by the vertex reconstruction.

Radioactive impurities in PMT are the main BG source in the XMASS experiment. Radioactive impurities of all materials used in PMT were measured using Germanium detector and those with lowest radioactive contamination were selected. The radioactivity of the developed PMT is 0.70 ± 0.28 Bq/PMT, 1.51 ± 0.31 Bq/PMT and 2.92 ± 1.61 Bq/PMT for ^{238}U , ^{232}Th and ^{60}Co , respectively. In addition, the PMTs and all detector elements were tested in the liquid xenon since liquid xenon is a highly solvent material. The cleaning methods were established to avoid elution. These developed PMTs have the lowest radioactivity among all other PMTs.

Typically xenon gas contains 0.1~3 ppm krypton. Krypton has a long-lived radioactive isotope ^{85}Kr . To reach BG level of 10^{-4} counts/day/kg/keV, the goal of the XMASS experiment, krypton contamination in xenon has to be reduced by more than 5 orders of magnitude. The distillation system has been developed to remove krypton from xenon gas. This distillation system has achieved the lowest levels of krypton contamination ever.

In order to achieve further improvement of the sensitivity of the XMASS experiment, PSD of liquid xenon was also studied in this thesis. The reaction of dark matter with xenon is observed as nuclear recoil events. On the other hand, gamma and β ray interactions with xenon, which are the main BG for dark matter searches, are observed as electron recoil events. Discrimination between the nuclear recoils and the electron recoils is very useful for the XMASS experiment. The scintillation decay time of liquid xenon is about 45 nsec for high energy electron recoils. It has been suspected that PSD for liquid xenon

is difficult because this decay time is so short, and a detailed study of PSD for xenon dark matter detectors has not been done so far.

In order to study PSD, a dedicated detector setup was constructed which has a high efficiency of collecting scintillation photons. In the first step of the PSD study, pulse shapes are measured with high light yield (20.9 p.e./keV) in order to evaluate the fundamental difference between nuclear recoils and electron recoils. From this study, a difference in the pulse shapes of nuclear and electron recoils is found even at the low energies relevant for dark matter detection. The *PSDratio* was defined as the charge from the leading edge of a pulse to 20 nsec divided by the charge from that same leading edge to 200 nsec. The *PSDratio* were 0.386 ± 0.003 and 0.465 ± 0.002 for electron recoil and nuclear recoil events at 4.8~7.2 keV, respectively. This *PSDratio* allows at high light yield (20.9 p.e./keV) to reject electron recoils to $7.7 \pm 1.1(\text{stat}) \pm 1.2(\text{sys}) \times 10^{-2}$ for 4.8~7.2 keV events with 50% efficiency for nuclear recoil events. For 14.4~19.1 keV events the rejection power was more than 3 orders of magnitude.

In the second step, the PSD performance was studied at the expected light yield for the XMASS detector (4.6 p.e./keV). Using a mask made from copper the light yield was tuned to this value. At the light yield of the XMASS detector, the rejection power was $2.4 \pm 0.2(\text{stat}) \pm 0.3(\text{sys}) \times 10^{-1}$ for 4.8~7.2 keV with 50% efficiency for nuclear recoil events.

Using the PSD technique developed in this thesis, the advantages of PSD for the XMASS experiment were discussed using MC simulations with the statistics of 1 year equivalent and 100 kg fiducial volume. The main BG of the XMASS experiment comes from gamma rays caused by the decay of radioactive nuclei in the PMTs. Using a fiducial volume cut, the majority of these BG events can be removed. However, some events occurring near the wall are reconstructed incorrectly in the fiducial volume, called the wall effect. The BG events are reduced to 5.7 events from 92 events using PSD for events with energy between 5 keV and 15 keV. These BG events are reduced to below 10% using PSD with 50% efficiency for nuclear recoil events.

The sensitivity at 90% C.L. is greatly improved to 5.6×10^{-45} cm² from 2.9×10^{-44} cm² using PSD at $M_\chi = 100$ GeV. In addition, PSD gives additional support to dark matter signals if they are detected.

Appendix A

Direct detection of WIMP

The neutralinos can be detected via elastic scattering with ordinary matter on the earth. Two types of interaction are predicted, one is spin-independent (SI) and the other is spin-dependent(SD) interaction. In this chapter the theoretical framework of direct detection is described based on [14].

A.1 Total event rate

The dark matter detection rate depends on relative movement between the detector on the earth and the dark matter. The number density of dark matter particles is given by,

$$dn = \frac{n_0}{k} f(v, v_e) d^3v \quad (\text{A.1})$$

$$n_0 \equiv \int_0^{v_{esc}} dn \quad (\text{A.2})$$

$$k = \int_0^{2\pi} d\phi \int_{-1}^1 d(\cos\theta) \int_0^{v_{esc}} f(v, v_e) v^2 dv \quad (\text{A.3})$$

where k is a normalization constant, n_0 is the average of the number of dark matter particles and is equal to the ratio between the mass density of the dark matter, ρ_D , and the mass of the dark matter particle, M_{chi} . v is the dark matter velocity relative to the target, v_e is the earth (target) velocity relative to the rest frame of the dark matter particles and $v_{esc} = |v + v_e|$ is the local galactic escape velocity.

In Eq.A.1, a Maxwell-Boltzmann distribution,

$$f(v, v_e) = e^{-(v+v_e)^2/v_0^2} \quad (\text{A.4})$$

is assumed as the dark matter velocity distribution. Here v_0 is the velocity dispersion of the dark matter. In case of $v_{esc} = \infty$, k is expressed following from the Eq.A.3

$$k = k_0 = (\pi v_0^2)^{3/2} \quad (\text{A.5})$$

For $v_e = 0$ and $v_{esc} = \infty$, the mean velocity of dark matter particles observed on the earth, $\langle v \rangle$, is expressed as

$$\langle v \rangle = \frac{2}{\sqrt{\pi}} v_0 \quad (\text{A.6})$$

The differential event rate per unit mass (kg) on a target is

$$dR = \frac{N_A}{A} \sigma_{\chi-N} v dn \quad (\text{A.7})$$

where N_A is the Avogadro number per unit mass ($6.02 \times 10^{26} \text{ kg}^{-1}$), A is the mass number of target nucleus and $\sigma_{\chi-N}$ is the neutralino-nucleus ($\chi-N$) cross section for zero momentum transfer. The total event rate R is then expressed as

$$R = \frac{N_A}{A} \sigma_{\chi-N} \int v dn = \frac{N_A}{A} \sigma_{\chi-N} n_0 \langle v \rangle \quad (\text{A.8})$$

From the Eq.A.6 and Eq.A.8 the total event rate for the $v_e = 0$ and the $v_{esc} = \infty$ (R_0) is expressed as

$$R_0 = \frac{N_A}{A} \sigma_{\chi-N} \frac{\rho_D}{M_\chi} \frac{2}{\sqrt{\pi}} v_0 \quad (\text{A.9})$$

R_0 can be calculated in the unit of $\text{kg}^{-1} \text{ day}^{-1}$ as

$$R_0 = \frac{361}{M_\chi M_N} \left(\frac{\sigma_{\chi-N}}{1 \text{ pb}} \right) \left(\frac{\rho_D}{0.3 \text{ GeV } c^{-2} \text{ cm}^{-3}} \right) \left(\frac{v_0}{230 \text{ km } s^{-1}} \right) \quad (\text{A.10})$$

where M_N is the mass of the target nucleus. The units of M_χ and M_N are $\text{GeV } c^{-2}$.

In case of the $v_e \neq 0$ and $v_{esc} \neq \infty$ the total event rate is expressed from Eq.A.8 and Eq.A.9,

$$R = R_0 \frac{\sqrt{\pi} \langle v \rangle}{2 v_0} = R_0 \frac{k_0}{k} \frac{1}{2\pi v_0^4} \int v f(v, v_e) d^3v \quad (\text{A.11})$$

Then the total event rate $R(v_e, v_{esc})$ is expressed

$$\frac{R(0, v_{esc})}{R_0} = \frac{k_0}{k_1} \left[1 - \left(1 + \frac{v_{esc}^2}{v_0^2} \right) e^{-v_{esc}^2/v_0^2} \right] \quad (\text{A.12})$$

$$\frac{R(v_e, \infty)}{R_0} = \frac{1}{2} \left[\sqrt{\pi} \left(\frac{v_e}{v_0} + \frac{1}{2} \frac{v_0}{v_e} \right) \text{erf} \left(\frac{v_e}{v_0} \right) + e^{-v_e^2/v_0^2} \right] \quad (\text{A.13})$$

$$\frac{R(v_e, v_{esc})}{R_0} = \frac{k_0}{k_1} \left[\frac{R(v_e, \infty)}{R_0} - \left(\frac{v_{esc}^2}{v_0^2} + \frac{1}{3} \frac{v_e^2}{v_0^2} + 1 \right) e^{-v_{esc}^2/v_0^2} \right] \quad (\text{A.14})$$

where $erf\left(\frac{v_e}{v_0}\right) = 2/\sqrt{\pi} \int_0^{\frac{v_e}{v_0}} \exp(-t^2) dt$, k_1 is the value of k for the $v_{esc} \neq \infty$ written as

$$k_1 = k_0 \left[erf\left(\frac{v_{esc}}{v_0}\right) - \frac{2}{\sqrt{\pi}} \frac{v_{esc}}{v_0} e^{-v_{esc}^2/v_0^2} \right] \quad (\text{A.15})$$

The recoil energy (E_R) of a nucleus struck by a dark matter particle of kinetic energy E ($\frac{1}{2}M_\chi v^2$) and scattered at an angle θ (in center of mass frame) is

$$E_R = E r (1 - \cos \theta)/2 \quad (\text{A.16})$$

$$r = \frac{4M_\chi M_N}{(M_N + M_\chi)^2} \quad (\text{A.17})$$

From the assumption that the scattering is isotropic in the center of mass frame so that recoils are uniformly distributed in E_R over the range $0 \leq E_R \leq E r$, the differential event rate is

$$\frac{dR}{dE_R} = \int_{E_{min}}^{E_{max}} \frac{1}{E r} dR(E) = \frac{1}{E_0 r} \int_{v_{min}}^{v_{max}} \frac{v_0^2}{v^2} dR(v) \quad (\text{A.18})$$

where $E_{min} = E_R/r$ is the minimum energy of the incident particle which can produce a nuclear recoil of the energy E_R , $E_0 = 1/2M_\chi v_0^2$ and v_{min} is the dark matter particle velocity with the energy E_{min} . In case of $M_\chi = 100\text{GeV}$ and $v_0 = 220\text{km/s}$, the E_0 is 26.9keV . Using Eq.A.11, the differential event rate is

$$\frac{dR}{dE_R} = \frac{R_0}{E_0 r} \frac{k_0}{k} \frac{1}{2\pi v_0^2} \int_{v_{min}}^{v_{max}} \frac{1}{v} f(v, v_e) d^3v \quad (\text{A.19})$$

For the simple case of $v_e = 0$ and $v_{esc} = \infty$

$$\frac{dR(0, \infty)}{dE_R} = \frac{R_0}{E_0 r} e^{-\frac{E_R}{E_0 r}} \quad (\text{A.20})$$

The distribution of the recoil energy is determined by the mass of the dark matter particle and target nuclei.

For the $v_e \neq 0$ and the $v_{esc} \neq \infty$

$$\frac{dR(0, v_{esc})}{dE_R} = \frac{k_0}{k_1} \frac{R_0}{E_0 r} \left(e^{-E_R/E_0 r} - e^{-v_{esc}^2/v_0^2} \right) \quad (\text{A.21})$$

$$\frac{dR(v_e, \infty)}{dE_R} = \frac{k_0}{k_1} \frac{R_0}{E_0 r} \left[erf\left(\frac{v_{min} + v_e}{v_0}\right) - erf\left(\frac{v_{min} - v_e}{v_0}\right) \right] \quad (\text{A.22})$$

$$\sim c_1 \frac{R_0}{E_0 r} e^{-c_2 E_R/E_0 r} \quad (\text{A.23})$$

$$\frac{dR(v_e, v_{esc})}{dE_R} = \frac{k_0}{k_1} \left[\frac{dR(v_e, \infty)}{dE_R} - \frac{R_0}{E_0 r} e^{-v_{esc}^2/v_0^2} \right] \quad (\text{A.24})$$

where c_1 and c_2 are fitting constants and vary with the seasons. The average value of c_1 and c_2 are 0.751 and 0.561 through the year [21]. The dR/dE_R is conventionally expressed in the units $\text{keV}^{-1}\text{kg}^{-1}\text{day}^{-1}$ (referred to as differential rate unit, d.r.u.) The velocity dispersion and the escape velocity are commonly set to $v_0 = 220 \pm 40 \text{ km/s}$ and $v_{esc} = 450 \sim 650 \text{ km/s}$.

A.2 Cross section for the neutralino-nucleus scattering

The cross section at zero momentum transfer, $\sigma_{\chi-N}$ is expressed as

$$\sigma_{\chi-N} = 4G_F^2 \mu_{\chi-N}^2 C_N \quad (\text{A.25})$$

where G_F is the Fermi coupling constant ($1.166 \times 10^{-5} \text{GeV}^{-2} (\hbar c)^3$), $\mu_{\chi-N}$ is the reduced mass of the neutralino and the target nucleus,

$$\mu_{\chi-N} = \frac{M_\chi M_N}{M_\chi + M_N} \quad (\text{A.26})$$

C_N is a dimensionless number that carries all the particle-physics model information called enhancement factor. C_N is a sum of SI and SD term,

$$C_N = C_N^{SI} + C_N^{SD} \quad (\text{A.27})$$

The $\sigma_{\chi-N}$ can be expressed using the enhancement factor of proton C_p and enhancement factor of neutron C_n ,

$$\sigma_{\chi-N} = \sigma_{\chi-p} \frac{\mu_{\chi-N}^2 C_N}{\mu_{\chi-p}^2 C_p} = \sigma_{\chi-n} \frac{\mu_{\chi-N}^2 C_N}{\mu_{\chi-n}^2 C_n} \quad (\text{A.28})$$

where $\sigma_{\chi-p}$ and $\sigma_{\chi-n}$ are neutralino-proton and neutralino-neutron cross sections.

A.2.1 Spin-Independent (SI) interaction

The enhancement factor of the SI cross section is expressed as

$$C_N^{SI} = \frac{1}{\pi G_F^2} \left[Z f^{(p)} + (A - Z) f^{(n)} \right]^2, \quad (\text{A.29})$$

where A is the mass number and Z is the atomic number, $f^{(p)}$ and $f^{(n)}$ are neutralino-proton and neutralino-neutron couplings. For $f^{(p)} \simeq f^{(n)}$, $C_N^{SI} \propto A^2$ and

$$\frac{C_N^{SI}}{C_p^{SI}} = \frac{C_N^{SI}}{C_n^{SI}} = A^2 \quad (\text{A.30})$$

From Eq.A.28 and Eq.A.30

$$\sigma_{\chi-N}^{SI} = \sigma_{\chi-p}^{SI} \frac{\mu_{\chi-N}^2}{\mu_{\chi-p}^2} A^2 \quad (\text{A.31})$$

The materials with large A value are effective target nuclei for SI interactions.

A.2.2 Spin-Dependent(SD) interaction

The enhancement factor of the SD cross section is expressed as

$$C_N^{SD} = \frac{8}{\pi} \left(a_p \langle S_{p(N)} \rangle + a_n \langle S_{n(N)} \rangle \right)^2 \frac{J+1}{J} \quad (\text{A.32})$$

where the $\langle S_{p(N)} \rangle$ and $\langle S_{n(N)} \rangle$ are the expectation values of the proton and neutron spin in the nucleus N , a_p and a_n are the neutralino-proton and neutralino-neutron SD couplings, and J is the total spin of the nucleus. The a_p and a_n are expressed as

$$a_p = \sum_{q=u,d,s} \frac{\alpha_{2q}}{\sqrt{2}G_F} \Delta_q^{(p)} \quad (\text{A.33})$$

$$a_n = \sum_{q=u,d,s} \frac{\alpha_{2q}}{\sqrt{2}G_F} \Delta_q^{(n)} \quad (\text{A.34})$$

where $\Delta_q^{(n)}$ and $\Delta_q^{(p)}$ are the quark spin contents of nucleon. The part of $(a_p \langle S_{p(N)} \rangle + a_n \langle S_{n(N)} \rangle)$ is called Lande factor (Λ). The Eq.A.32 is expressed as

$$C_N^{SD} = \frac{8}{\pi} \Lambda^2 J(J+1) \quad (\text{A.35})$$

From Eq.A.28 and Eq.A.35

$$\sigma_{\chi-N}^{SD} = \sigma_{\chi-p}^{SD} \frac{\mu_{\chi-N}^2}{\mu_{\chi-p}^2} \frac{\Lambda^2 J(J+1)}{0.75} \quad (\text{A.36})$$

where the value of $\Lambda^2 J(J+1)$ for proton is 0.75 from Table.A.1.

unpaired proton			
Isotope	J	Abundance (%)	$\Lambda^2 J(J+1)$
^1H	1/2	100	0.750
^7Li	3/2	92.5	0.244
^{19}F	1/2	100	0.647
^{23}Na	3/2	100	0.041
^{127}I	5/2	100	0.007
^{133}Cs	7/2	100	0.052

unpaired neutron			
Isotope	J	Abundance (%)	$\Lambda^2 J(J+1)$
^3He	1/2	1.3×10^{-4}	0.928
^{29}Si	1/2	4.7	0.063
^{73}Ge	9/2	7.8	0.065
^{129}Xe	1/2	26.4	0.124
^{131}Xe	3/2	21.2	0.055
^{183}W	1/2	14.3	0.003

Table A.1: Values of $\Lambda^2 J(J+1)$ calculated on the basis of the odd group model for various nuclei [21].

A.3 Nuclear form factor correction

In the case of non-zero momentum transfer, the matrix elements of the nucleon operators in a nuclear state have to be evaluated. The effective interaction with nuclei the cross section of neutralino-nucleus decrease because of the effect of the nuclear form factor. The cross section is expressed using the cross section of zero momentum transfer σ_0 ,

$$\sigma(qr_n) = \sigma_0 F^2(qr_n) \quad (\text{A.37})$$

where the q is the momentum transfer ($\sqrt{2M_N E_R}$) and r_n is the effective nuclear radius. For the SI case, the form factor is expressed as

$$F^2(qr_n) = \left[\frac{3j_1(qr_n)}{qr_n} \right]^2 \exp(-q^2 s^2) \quad (\text{A.38})$$

where the $j_1(x) = [\sin(x) - x \cos(x)]/x^2$ is a spherical Bessel function, $r_1 = (R^2 - 5s^2)$, $R \simeq 1.2 \text{fm} \times A^{1/3}$ and $s, \simeq 1 \text{fm}$, is a measure of the nuclear skin thickness. For the SD case at non-zero momentum transfer there is also a form factor suppression which must be calculated from the nuclear wave function. From Eq.A.33 and Eq.A.34 the isoscalar (a_0) and isovector (a_1) are expressed as

$$a_0 = a_p + a_n \quad (\text{A.39})$$

$$a_1 = a_p - a_n \quad (\text{A.40})$$

The form factor is expressed as using the spin structure function $S(q)$

$$F^2(q) = \frac{S(q)}{S(0)} \quad (\text{A.41})$$

$$S(q) = a_0^2 S_{00}(q) + a_1^2 S_{11}(q) + a_0 a_1 S_{01}(q) \quad (\text{A.42})$$

where $S_{ij}(q)$ is the independent form factor, pure isoscalar term S_{00} , pure isovector term S_{11} and an interference term S_{01} .

The form factor is expressed as approximately zeros of the Bessel function when the coupling of odd-group nucleon only are taken into account. For the useful experimental range $0 \leq qr_n \leq 6$ the form factor is expressed as [21]

$$F^2(qr_n) = j_0^2(qr_n) \quad (qr_n < 2.55, qr_n > 4.5) \quad (\text{A.43})$$

$$F^2(qr_n) = \text{constant} \simeq 0.047 \quad (2.55 \leq qr_n \leq 4.5) \quad (\text{A.44})$$

where $j_0(x) = \sin(x)/x$ and $r_n \simeq 1.0A^{1/3}$.

Fig.A.1 and Fig.A.2 show the nuclear form factor as a function of recoil energy for the spin independent case and the spin dependent case.

A.4 Relative scintillation efficiency of nuclear recoils

The dark matter signal is detected as a signal of a nuclear recoil. On the other hand, scintillation detectors are usually calibrated using gamma ray sources.

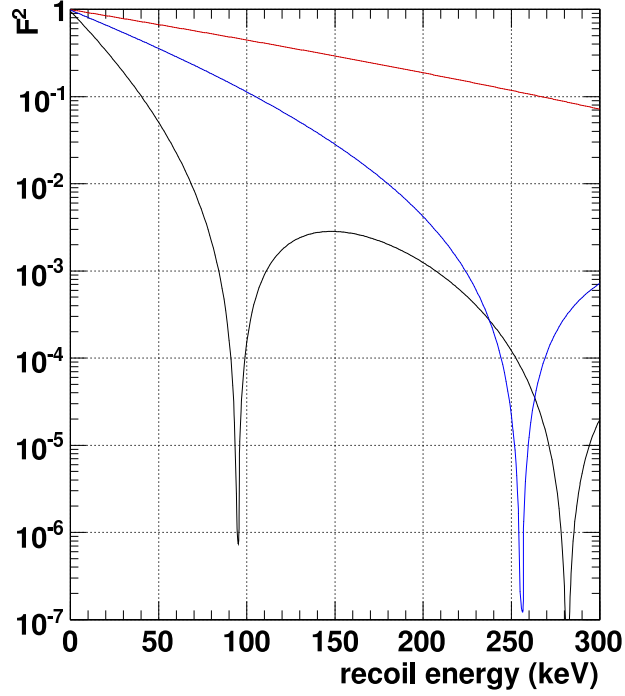


Figure A.1: Nuclear form factor as a function of recoil energy for the spin independent case in various targets. The form factor of Xenon, argon and germanium are shown by the black, red and blue lines.

The visible energy, E_v , is defined as the energy calibrated by gamma ray sources. Therefore the different energy depositions of the nuclear recoil against the electron recoil have to be taken into account. The ratio of the visible energy to the recoil energy is expressed as

$$E_r = \frac{E_v}{L_{eff}} \quad (\text{A.45})$$

where L_{eff} is the relative scintillation efficiency.

The L_{eff} have been measured using a neutron source. The L_{eff} as a function of visible energy, E_v , for various detectors are listed in Table.A.2. The detail of L_{eff} for xenon is described at section 3.4.

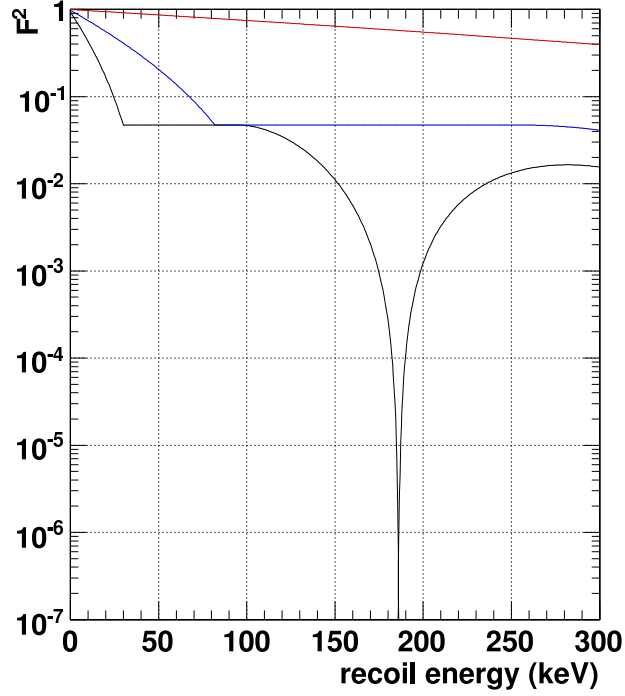


Figure A.2: Nuclear form factor as a function of recoil energy for spin dependent case in various targets. The form factors of ^{129}Xe , ^{19}F and ^{73}Ge are shown by the black, red and blue lines.

A.5 The expected signal of dark matter

The expected signal of the dark matter is described in this section. The dependence on target nucleus and annual modulation are discussed.

A.5.1 Dependence on target nucleus

The event rate of dark matter depends on the target nucleus. Fig.A.3 and Fig.A.4 show the event rate of dark matter with the various nuclei for the SI-interacting and the SD-interacting neutralino of $M_x = 100\text{GeV}$ and $\sigma_{\chi-p}^{SI} = 1 \times 10^{-43}\text{cm}^2$. The recoil energy spectrum depends on target nuclei, which is useful for determining the mass of WIMPs.

Target	Nucleus	f_Q
Xe	Xe	0.2 [73]
		0.22 ± 0.01 [68]
NaI(Tl)	Na	0.3 [74]
	I	0.08 [74]
Ge	Ge	0.25 [75]

Table A.2: The quenching factor, f_Q , for various targets. They have energy dependence but in this table single numbers are shown for simplicity. More details are discussed in the references.

A.5.2 Annual modulation

An annual modulation of the event rate is expected by the Earth's motion around the Sun. Its signatures such as variations in event rate and recoil energy spectrum are quite important since their observation gives compelling evidence of dark matter.

The expected nuclear recoil energy spectrum depends on the dark matter velocity distribution and the Earth velocity with respect to the Sun could cause an annual modulation. The detector velocity v_e (i.e. velocity of the earth) in the Galactic rest frame can be expressed as,

$$v_e = v_{sun} + v_{earth} \cos \gamma \cos \omega(t - t_0) \quad (\text{A.46})$$

where the $v_{sun} = 230 \text{ km/s}$ is the Sun's velocity with respect to the halo, the $v_{earth} = 30 \text{ km/s}$ is the earth's orbital velocity around the Sun on a plane with inclination $\gamma = 60^\circ$ respect to the galactic halo, $\omega = 2\pi/T$ with $T = 1 \text{ year}$ and $t_0 \simeq 2 \text{nd June}$.

Fig.A.5 shows the expected spectrum in 2nd June and 4th Dec with the $M_x = 100 \text{ GeV}$, $\sigma_{\chi-p}^{SI} = 1 \times 10^{-43} \text{ cm}^2$, $v_e = 245 \text{ km/s}$ on 2nd Jun and $v_e = 215 \text{ km/s}$ on 4th Dec. From the calculation of the event rate, the difference is only $\sim 3\%$ and the large mass detector is required to measure the annual modulation.

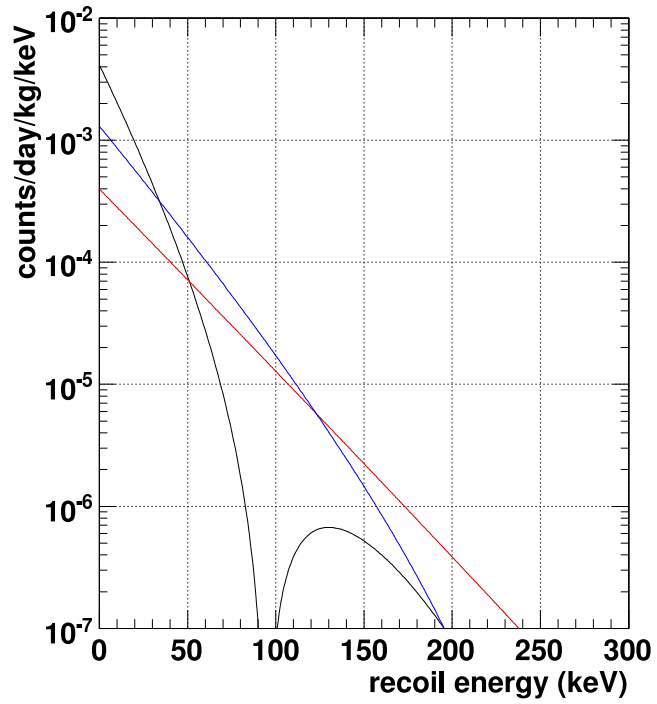


Figure A.3: The expected event rate as a function of nuclear recoil energy for the spin independent case. The neutralino mass M_χ and $\sigma_{\chi-p}^{SI}$ are assumed to be 100 GeV and 10^{-43}cm^2 . The expected event rates of Xenon, Argon and Germanium are shown by the black, red and blue lines.

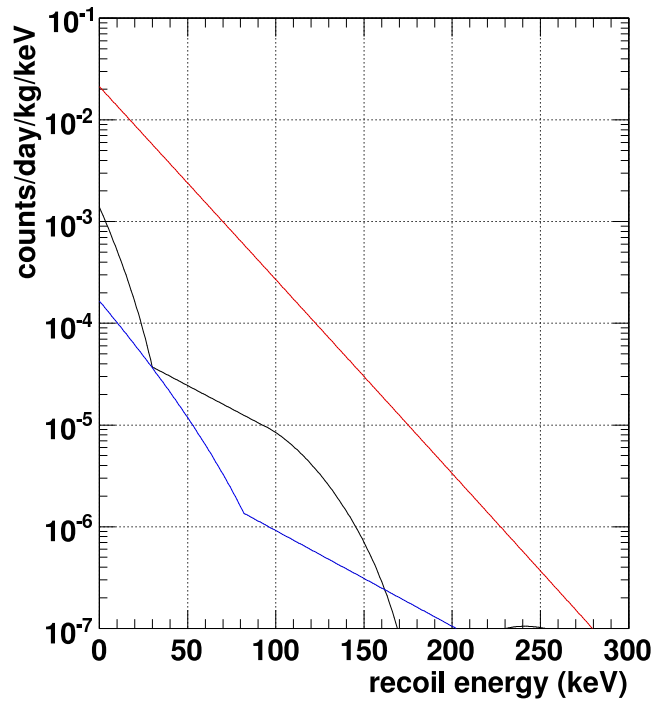


Figure A.4: The expected event rate as a function of nuclear recoil energy for the spin dependent case. The neutralino mass M_χ and $\sigma_{\chi-p}^{SD}$ are assumed to be 100 GeV and 10^{-38}cm^2 . The expected event rate of Xenon, Fluorine and Germanium are shown by the black, red and blue lines.

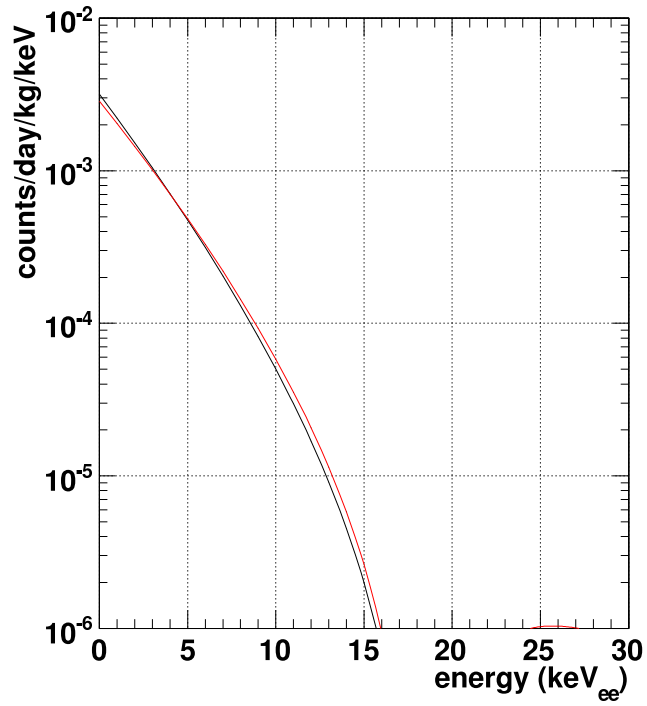


Figure A.5: The expected event rate as a function of energy for the spin independent case. The neutralino mass M_χ and $\sigma_{\chi-p}^{SI}$ are assumed to be 100 GeV and 10^{-43}cm^2 . L_{eff} is assumed 0.2. The black and red lines show the expected event rates on Dec 4th and June 2nd, respectively

Bibliography

- [1] K. G. Begeman, A. H. Broeils and R. H. Sanders, MNRAS **249**(1991)523.
- [2] J.Dunkley, *etal.*, Astrophys.J.Supp **180**(2009) 306.
- [3] D.Tytler, *etal.*, Physica Scripta **T85**(2000) 12.
- [4] M.Tegmark, *etal.*, Phys Rev D **69**(2004) 103501.
- [5] R.A.Knop, *etal.*, Astrophys.J. **598**(2003) 102.
- [6] A.W.Allen, *etal.*, MNRAS **334**(2002) L11.
- [7] R.P.Olling, MNRAS **311**(2000) 361.
- [8] J.Caldwell and J.P.Ostrinker, Astrophys.J. **251**(1981) 61.
- [9] M.Tegmark, *etal.*, Phys Rev D **74**(2006) 123507.
- [10] Astalos, *etal.*, Phys Rev D **69**(2004) 011101.
- [11] P.Sikivie, Phys Rev Lett **51**(1983) 1415.
- [12] S. Andriamonje1, *etal.*, JCAP 04(2007) 010.
- [13] Y.Inoue, *etal.*, Phys.Lett.B **68**(2008) 93.
- [14] G.Jungman, *etal.*, Phys.Rep. **267**(1996) 195.
- [15] U.Amaldi, *etal.*, Phys.Lett.B **260**(1991) 447.
- [16] G. Abbiendi, *etal.*, Eur. Phys. J.**C35** (2004) 1
- [17] M.Nojiri, *etal.*, JHEP **0603**(2006) 063.
- [18] P.Picozza, *etal.*, PAMELA Astropart. Phys. **27**(2007) 296.
- [19] T.Delahaye, *etal.*, Phys.Rev.D **77**(2008) 063527.
- [20] The Super-Kamiokande Collaboration, Phys.Rev.D **70**(2004) 083523.
- [21] J.D.Lewin and P.F.Smith, Astropart. Phys. **6**(1996) 87.
- [22] B.Bernabei, *etal.*, Eur.Phys.J.C. **56**(2008) 56.
- [23] B.Bernabei, *etal.*, arXiv:1002.1028.
- [24] M.G.Boulay, *etal.*, arXiv:0904.2930.

- [25] J.Angle, *etal.*, Phys.Rev.Lett. **100**(2008) 021303.
- [26] Z.Ahmed, *etal.*, Science. **327**(2010) 1619.
- [27] A.C. Sinnock and B.L. Smith, Phys. Rev., **181**(1969)1297.
- [28] Particle Data Group: S. Eidelman, *etal.*, Phy. Lett. B **592**(2004)1.
- [29] J. Jortner, *etal.*, J. Chem. Phys., **42**(1965)4250.
- [30] S. Nakamura, Yokohama National University, Private communication.
- [31] A.Hitachi and T. Takahashi, Phys.Rev.B **27**(1983)5279.
- [32] G.M.Seidel, *etal.*, Nucl. Instr. and Meth. A **489**(2002)189.
- [33] MEG proposal to PSI, Proposal to INFN,
(URL:<http://meg.web.psi.ch/docs/index.html>).
- [34] Photon Cross Sections Database,
(URL:<http://physics.nist.gov/PhysRefData/Xcom/Text/XCOM.html>).
- [35] A. Baldini, *etal.*, IEEE Trans. Dielectr. Electr. Insul. **13**(2006)547.
- [36] S.Kubota, *etal.*, Phys.Rev.B **20**(1979)3486.
- [37] I.Onsager, Phys.Rev. **54**(1938)554.
- [38] T.Doke, *etal.*, J.Appl.Phys **41**(2002)1538.
- [39] J.Lindhard, *etal.*, Mat.Fys.Medd.Dan.Vib.Selsk.33, no.10(1963)
- [40] A.Hitachi, Astropart. Phys. **24**(2005) 247.
- [41] E.Aprile, *etal.*, arXiv:1005.0380.
- [42] R.Bernabei, *etal.*, arXiv:0806.0011v2.
- [43] E.Aprile and T.Doke, Rev.Mod.Phys.**82**(2010)2053.
- [44] J.Kwong, *etal.*, arXiv:0908.0790.
- [45] G.J.Alner, *etal.* Astropart. Phys. **23**(2005)444.
- [46] R.Bernabei, *etal.*, Phys.Lett.B **436**(1998)379.
- [47] A.Benoit, *etal.*, Phys.Lett.B **637**(2006)156.
- [48] Y.Suzuki, *etal.*, arXiv:0008296.
- [49] The Super-Kamiokande Collaboration, Phys. Lett. **452**(1999)418.
- [50] W. Ootani, master thesis, University of Tokyo, 1994.
- [51] A. Minamino, master thesis, University of Tokyo, 2004.
- [52] K. Miuchi, master thesis, University of Tokyo, 1999.
- [53] M. Ishitsuka, master thesis, University of Tokyo, 2001

- [54] E. Aprile, *etal.*, arXiv:1001.2834v1.
- [55] P. Cauwels, *etal.*, Radiation Physics and Chemistry. **61**(2001)649.
- [56] K. Abe, *etal.*, Astropart. Phys. **31**(2009)290.
- [57] W. L. McCabe and J. C. Smith, Unit Operations of Chemical Engineering, 3rd Edition, McGraw-Hill (1976).
- [58] A. Minamino, *etal.*, arXiv:0912.2405.
- [59] Geant4 Collaboration, Nucl. Instr. and Meth. A **503**(2003)250.
- [60] V. Tomasello, *etal.*, Nucl. Instr. and Meth. A **595**(2008)431.
- [61] K. Ueshima, *etal.*, Nucl. Instr. and Meth. A **594**(2008)148.
- [62] T. Doke and K. Masuda, Nucl. Instr. and Meth. A **420**(1999)62.
- [63] O. Sifner and J. Klomfar, J.Phys.Chem.Ref.Data **12**(1994)1.
- [64] John David Jackson, Classical Electrodynamics.
- [65] http://www.oken.co.jp/web_oken/Mgf2_jp.htm
- [66] Properties of Neutron Sources, IAEA-TECDOC-410 (1987).
- [67] T. Doke, *etal.*, Technique and Application of Xenon Detectors (2001)17.
- [68] D. Akimov, *etal.*, Nucl.Instr.and Meth A **524**(2000) 245.
- [69] R. Acciarri, *etal.*, Nucl. Instr. and Meth. A **607**(2009)169.
- [70] E. Aprile, *etal.*, Phys.Rev.Lett. **97**(2006) 081302.
- [71] A. Minamino, PhD thesis, University of Tokyo, 2008
- [72] D. Tucker-Smith and N. Weiner, Phys.Rev.D **72**(2005) 063509.
- [73] F. Arneode, *etal.*, Nucl.Instr.and Meth A **449**(2000) 147.
- [74] N.J. Spooner, *etal.*, Phys.Lett.B **321**(1994) 156.
- [75] Y. Messous, *etal.*, Astropart.Phys. **3**(1995) 361.